Polarization Measurements of Radio Emission of Cosmic Ray Air Showers with LOPES

Zur Erlangung des akademischen Grades eines
DOKTORS DER NATURWISSENSCHAFTEN
bei der Fakultät für Physik des
Karlsruher Institut für Technologie (KIT)

genehmigte

DISSERTATION

von

M. Sc. Paula-Gina Isar

aus Roşiori de Vede, Romania

Karlsruhe
Spring 2010

Abstract

It has been recently definitively established that the development of Extensive Air Showers (EAS) which are induced in the Earth's atmosphere by impinging cosmic particles from the outermost space is accompanied by the emission of radio waves. This phenomenon is experimentally investigated by the LOPES experiment, co-located at Karlsruhe Institute of Technology (KIT) with the EAS detector array KASCADE-Grande using traditional detection techniques.

The LOPES experiment is an absolutely amplitude calibrated array of radio antennae for observing radio waves from EAS in the frequency range of 40-80 MHz. The KASCADE-Grande array provides the trigger information and experimentally determined parameters of the associated EAS observed in the energy range of $10^{16} - 10^{18}$ eV. The studies are focussed to understand and clarify the phenomena of EAS radio emission, in particular in view of an eventual large scale application of a corresponding detection technique, like in LOFAR (Low Frequency Array for which LOPES is a prototype station) and for the Pierre Auger Observatory.

Until summer 2006, all 30 antennas were equipped in the east-west polarization direction only, measuring a single polarization of the radio emission. The data of this LOPES set-up provided the possibility for a detailed investigation of correlations of the radio signal with basic EAS parameters like arrival direction, particle energy and mass of the primary. The results enable studies of the radio signal on a single EAS event basis, in particular of its lateral extension. Nevertheless, the north-south polarization component is required for an improved understanding of the radio emission signal and for a verification of the geo-synchrotron effect as the dominant mechanism of radio emission in air showers.

The focus of the present work are measurements and analyses of the polarization of the radio signals from EAS. Investigations of the radio pulse height in correlation with EAS parameters, including an adequate parametrization of the pulse height per single polarization in east-west and north-south direction, respectively, have been performed. The studies of the lateral distribution per single event and per single polarization of the electric field are helpful for an improved understanding of the shower development. The polarization vector was finally reconstructed by observations with dual polarization antennae which are configured for both polarizations of signals recorded at the same place and simultaneously for the east-west and north-south direction. Comparisons with theoretical studies complete the investigations. The geo-synchrotron emission process is confirmed as the radio emission mechanism in cosmic ray air showers. In addition, it could be found that a not negligible contribution to the total signal stems from another emission process. It is most probably induced by the negative charge excess during the shower development. This contribution mainly modifies the North-South polarization component of the dominant geo-synchrotron induced signal.

Zusammenfassung

Polarisations-Messungen der Radiostrahlung von Luftschauern der Kosmischen Strahlung

Vor kurzem konnte definitiv geklärt werden, dass die Entstehung ausgedehnter Luftschauer kosmischer Strahlung einhergeht mit einer Emission von Radiosignalen. Dieses Phänomen wird derzeit unter anderem mit dem LOPES-Experiment am Karlsruher Institut für Technologie (KIT) untersucht, welches innerhalb einer Detektoranlage für ausgedehnten Luftschauer, KASCADE-Grande, aufgebaut ist.

KASCADE-Grande benutzt zur Beobachtung von Luftschauern herkömmliche Messmethoden mit Teilchendetektoren. Das LOPES Experiment ist ein Netz von kalibrierten Radioantennen, das die Radiosignale der ausgedehnten Luftschauer bei 40-80 MHz vermisst. Das KASCADE-Grande Experiment liefert dazu den Trigger sowie wichtige experimentell bestimmte Parameter des assoziierten Luftschauers in einem Energiebereich von $10^{16} - 10^{18}$ eV. Die Untersuchungen sind darauf ausgerichtet, die Radioemission ausgedehnter Luftschauer besser zu verstehen und die Möglichkeiten einer großangelegten Anwendung dieser Nachweistechnik in anderen Experimenten wie LOFAR (Low Frequency Array für das LOPES eine Prototyp Station darstellt) und für das Pierre-Auger-Observatorium zu untersuchen.

Bis zum Sommer 2006 waren 30 Antennen nur für eine Detektion der Polarisation in Ost-West-Richtung ausgerüstet. Die Resultate ermöglichten die Analyse der Radiosignale auf Basis einzelner Ereignisse, insbesondere auch der lateralen Verteilung des Radiosignals. Trotzdem bleiben einige Fragen offen, solange nur die Ost-West-Polarisation beobachtet wird, da diese emittierte Radiosignal nicht vollständig erfasst. Für ein umfassendes Verständnis ist zusätzlich eine Messung der Nord-Süd-Polarisations-Komponente erforderlich.

Der Fokus dieser Arbeit liegt auf der Messung und Analyse der Polarisation der Radiosignale aus ausgedehnten Luftschauern. Untersuchungen der Höhe des Radiopulses in Korrelation mit den Schauerparametern, einschließlich einer adäquaten Parameterisierung der Pulshöhe für die einzelnen Polarisationsrichtungen, wurde durchgeführt. Studien der lateralen Verteilung für einzelne Ereignisse und der Polarisationsrichtung des elektrischen Feldes verbessern das Verständnis der Luftschauerentwicklung. Schliesslich wurde der Polarisationsvektor mit speziellen Antennen analysiert, die eine Sensitivität sowohl in Ost-West als auch Nord-Süd-Richtung aufweisen, gemessen. Vergleiche mit theoretischen Überlegungen komplettieren die Untersuchungen. Dabei konnte der Geo-Synchrotron Effekt als dominanter Emissionsmechanismus für das Radiosignal aus augedehnten Luftschauern bestätigt werden. Zusätzlich konnte gezeigt werden, dass es zusätzlich zum geo-magnetischen Effekt einen weiteren, nicht vernachlässigbaren Beitrag zum Radiosignal gibt, der vermutlich auf den im Luftschauer erzeugten negativen Ladungsüberschuss zurück zu führen ist. Dieser Beitrag zur Radioemission modifiziert vornehmlich die Nord-Süd Polarisationskomponente des durch den Geo-Synchrotron Mechanismus erzeugten Signales.

Content

1. Introduction

Our Earth is continuously bombarded by cosmic particles from the space, most abundantly by high energy protons and heavier nuclei of various atoms, with an intensity of about 1000 particles/$m^2 \cdot s$ integrated over all directions, and with energies up to about 10^{20} eV. After all, the highest energy reasonably well claimed is at $3 \cdot 10^{20}$ eV (Fly's Eye, 1993). The cosmic ray energy density, integrated over all energies, is approximately 1 eV/cm^3, in the same order as that of the starlight (0.6 eV/cm^3) and of the galactic magnetic field (0.2 eV/cm^3). If we include in the term "prime cosmic rays" the neutrino radiation and the still undiscovered gravitational waves, cosmic rays are the only messengers from outside the solar system in addition to electromagnetic waves observed in all wavebands. Primary cosmic rays are dominantly charged particles and are deflected by the irregular magnetic fields in space, eventually with exception at highest energies, so that in general the origin is obscured. From astrophysical point of view the basic questions are: "Where are they coming from? How are they accelerated to highest energies? How do they propagate through the space?". When entering into the Earth's atmosphere, cosmic ray particles produce secondary radiation by collisions with the air nuclei, producing the full zoo of subnucleonic particles, of electrons and photons. The cosmic radiation phenomenon has been discovered by Victor Hess, [1, 2], in his celebrated balloon ascents in 1911/12. Since that time the studies of cosmic rays have gained fascinating aspects. In addition to the intrinsic interest in this phenomenon of nature, as a subject of science it combines astrophysical messages with information of particle physics. Despite a lapse of time of nearly 100 years since discovery, their origin and accelerator mechanisms are still largely a matter of conjecture. The energy spectrum of primary cosmic rays comprises more than 12 orders of magnitude in the energy scale. The spectrum follows an overall power law ($\propto E^{-2.7}$) with various district changes of the spectral index, most conspicuously around $3 \cdot 10^{15}$ eV, called the knee (see Fig. 1.1). The part above the knee exceeds till recently, when the LHC [3] was not yet in operation, the highest energies available at artificial accelerators. The flux of the primary cosmic ray falls from 1 particle/$cm^2 \cdot s$ to 1 particle /$km^2 \cdot yr$ at high energies. The steeply falling spectrum of primary cosmic rays implies that the particle flux at higher energies is too low for direct measurements by detectors carried by balloon or satellite flights.
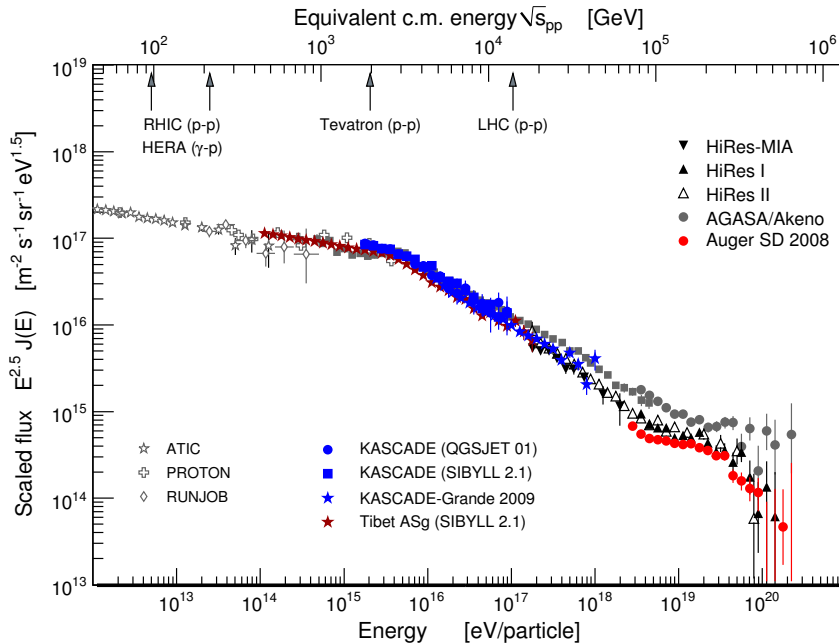
Figure 1.1: Cosmic ray energy spectrum from direct and indirect measurements of cosmic rays [4].

The standard method above $E \simeq 10^{14} \ eV$ is the observation of Extended Air Showers (EAS) induced by high energy particles when penetrating the atmosphere. EAS are particle cascades which develop by repeated collisions of the primary and fast secondary cosmic rays with air molecules, propagating to ground as an extended avalanche of electron - positron pairs and gamma rays, of muons and hadronic particles, laterally largely extended and able to be registered by particle detectors at ground. The EAS phenomenon has been discovered by Auger et al. in 1938 [5] and independently by Kohlhörster and colleagues [6]. Through the movement of these particles further detectable effects of the EAS are induced: Cherenkov radiation and fluorescence in air. All these EAS components are used for detailed detection procedures.

In 1964 Jelley et al. [7] observed also radio pulses from EAS, and this radiation has been subsequently studied in several research centres [8], even with triggering by a conventional array [9]. Jelly et al. used an array of dipole antennas, sensitive in the range of 40 MHz, operated in coincidence with Geiger counters. From the beginning two main mechanisms have been considered to contribute to EAS radio emission: Askaryan-type Cherenkov radiation due to a charged particle moving through the dielectric media air faster than the velocity of light [10] and emission arising from the deflection of charged particles in the geomagnetic field (synchotron radiation) [11]. In the 70's, however, the radio measurements lost their vital interest. This was probably due to the limited electronic facilities in those days, the lack of reproducibility of the results and insufficient knowledge in interpreting the data. As a consequence, the method was not pursued for longer time, and the historic results came into question. However, for studies of the emission mechanism, in particular investigations whether radio emission is generated in air by the interaction of the EAS avalanche with the Earth's magnetic field (coherent geosynchotron emission [12] were revived at the beginning of this 21st century, in particular with experimental studies of the LOPES

experiment which has definitively established and rediscovered the radio emission from EAS in 2005 [13]. LOPES is an array of dipole antennas with digital electronics, operated together with the conventional detector array KASCADE-Grande [14]. Compared to the historical experiments, it provides an order of magnitude increase in bandwidth and time resolution, effective digital filtering methods, and for the first time true interferometric imaging capabilities. Sophisticated simulations of radio emissions have been developed during recent years, e.g. the Monte Carlo code REAS [15], and help in the understanding of the full radio signal of cosmic ray air showers.

Radio techniques can help in the understanding of high energy cosmic rays, which can cover the range of $10^{18} - 10^{19}$ eV thought to represent the transit from galactic to extragalactic sources of cosmic rays. A large hybrid detector area with full exposure and good angular resolution is required, and thus radio techniques can play a important role in the field of the extensive air shower observations.

In particular, polarization of the radio emission initiated by the secondary charged particles of the air shower in the Earth's magnetic field is of importance. The polarization characteristics can tell about the air shower dependencies with respect to the radio signal, e.g. azimuthal dependencies. The radio signal is polarized into the direction of the shower axis and of the Earth's magnetic field. Knowledge of the shower direction given by its azimuth, zenith and the geomagnetic angle (the angle between the shower axis and the Earth's magnetic field) are of main importance in testifying the radio emission mechanism. Thus, the polarization measurements allow the recording of the most complete part of the radio signal which can therefore be fully compared with the corresponding simulations.

The present work is in context with the LOPES experiment and reports about first studies of the polarization features of the EAS radio pulses. After a sketch of the background, the LOPES experiment will be described and the signal reconstruction and data analysis will be outlined. Results on the observed polarization features are communicated and discussed.

2. Extended Air Showers

When a primary cosmic ray particle of sufficiently high energy penetrates into the Earth's atmosphere it loses the energy by a series of subsequent collisions with multiple production of secondary particles. On average a proton (with mean free path length of ca. 80 g/cm^2) will interact more than 12 times before it reaches sea level. The secondary particles are mainly neutral and charged π and K, but also heavier mesons, hyperons and antinucleons. The π^0s decay immediately into γ rays which soon produce $e^+ - e^-$ pairs which subsequently produce bremsstrahlung to create further pairs. In this way the γ rays induce avalanches of electromagnetic particles whose numbers quickly increase until their energy has dropped so far that ionization losses and Compton scattering become important (see Fig. 2.1). The charged $\pi^\pm$ and other hadrons either decay into high energy $\mu^\pm$ (and neutrinos) or interact further, producing more secondary hadrons. The $\pi^\pm$ interact only weakly within the atmosphere and have a relatively long lifetime due to the relativistic time dilation. They reach ground level with high probability.

The longitudinal development of an extended air shower (EAS) is characterized by a rapid increase of the number of particles up to a flat maximum and then of an exponential decline. There is approximately a logarithmic dependence of the height of maximum X_{max} on energy. The maximum is near sea level for high energy EAS, but about 6000 m in altitude for 10^{15} eV primaries. At sea level mostly showers are observed, which are dying out; at detector installations mounted at high altitude the observed EAS are "younger". Through the interaction of primary cosmic rays with nitrogen and oxygen nuclei of the atmosphere (thickness ca. 1000 g/cm^2) an EAS of charged and neutral particles is produced with three dominant components: (1st) electromagnetic particles with an equilibrium of electrons, positrons and γ quanta; (2nd) the penetrating μ component; (3rd) the hadronic core.

In the EAS the energy of the rare primary particle on top of the atmosphere is distributed to millions of secondary particles which move like an extended "pancake", hundreds of meters wide and a few meters thick. The different components have a different lateral distributions. The EAS particles are traditionally detected and their intensity is measured by extended arrays of detectors, installed on ground. Such a detector array is KASCADE-Grande [17, 18] installed in Forschungszentrum Karlsruhe,
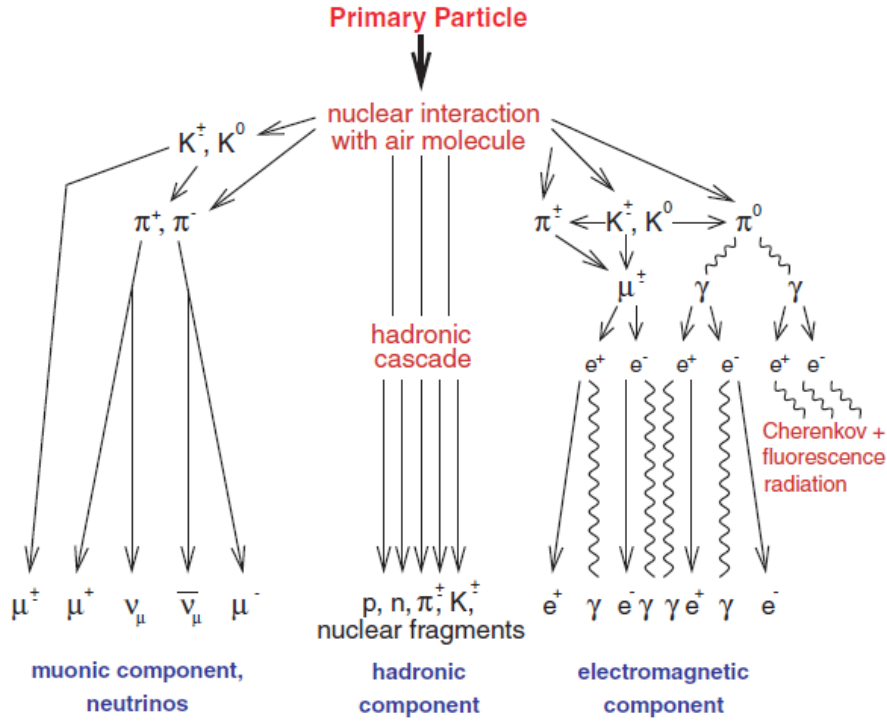
Figure 2.1: Air shower development in the Earth's atmosphere [16].

now KIT (Karlsruhe Institute of Technology), Campus North. The measurements with arrays of charged particle detectors provide the basic EAS parameters:

(i) the location where the shower axis intersects the ground;

(ii) the lateral distributions of the various components and integrated the total number of the particles of various components, called the shower sizes;

(iii) the azimuth and zenith angles of the shower incidence deduced from the tilt of the shower "disk" as it passes through the detectors.

There is a number of different EAS observables defined with specific observations like the time distributions of the arriving particles [19]. It is a general goal to relate the EAS observables to the energy and mass of the indirectly observed primary particle from the cosmos. For that extensive Monte Carlo simulations of the EAS development have to be invoked [16].

The EAS development is accompanied with different effects in the atmosphere. The fast moving charged particles induce Cherenkov light [20, 21] in the atmosphere which provides relevant information, when being observed under favorable conditions. Another detection technique is based on the observation of nitrogen fluorescence [22], mainly efficient at higher energies. This technique is applied at the Pierre Auger Observatory [23, 24]. The advantage of Cherenkov and fluorescence light observations is that they inform about the longitudinal development of the EAS, differently from traditional ground level observations which only provide the (more or less detailed) actual status of the lateral development of the EAS. A further detection technique is on the horizon with observations of the radio emission from EAS. This the general subject of the present work.

3. Radio emission of EAS

The interest in radio emission from EAS originates from Gurgen Askaryan in 1962 [10] who called attention of the fact that any electromagnetic cascade in a gaseous, liquid or solid dielectric material rapidly develops a net charge asymmetry due to electron scattering and positron annihilation processes. When the shower front carrying the charge excess is moving through the dielectricum with a velocity faster than the speed of light in the medium, it emits Cherenkov radiation. This Askaryan effect is dominant in dense media.

Radio emission from Extended Air Showers has been discovered in the sixties of the last century [7], but because of the technical difficulties to detect unambiguously the radio pulses and uncertainties of the data handling, the pioneering experiments practically stopped in the seventies. The basic understanding followed the view that the continuously produced $e^+ - e^-$ pairs get separated by the geomagnetic field (see Fig. 3.1), giving rise to a transverse current in the shower. In a frame moving along with the shower, the electrons and positrons drift in opposite directions. The transverse current induces dipole radiation, which results by Lorentz-boosting in a strong forward-peaked radiation, timely compressed into an electromagnetic pulse, as shown in Fig 3.2.
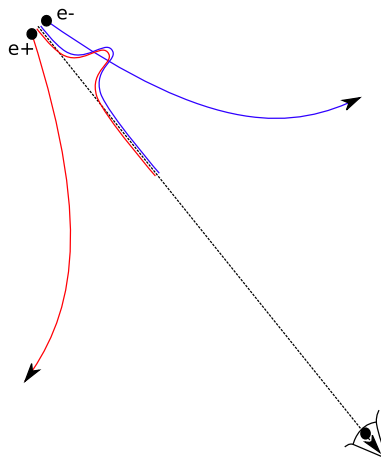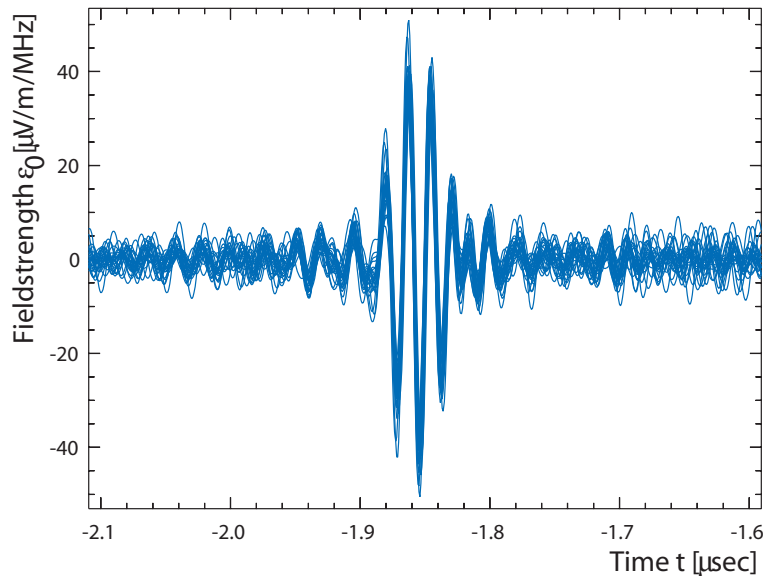

Figure 3.1: Electrons and positrons separated in the geomagnetic field.

Figure 3.2: Example of a radio pulse coherently registered by the LOPES antennas [25]. Calibrated, up-sampled traces of an example event, after correction for geometrical delays are shown. The radio pulse induced by a cosmic ray air shower can clearly be distinguished from the background noise.

Coherence is achieved since the shower in its densest regions is not wider than a wavelength around 100 MHz and at a few km height the phase shift due to the lateral extent of the shower for an observer on the ground is still less than a wavelength up to some 100 m from the shower core. Most of the electrons in the shower are actually concentrated within a region smaller than this, and we may ignore an emission from larger radii. At radio frequencies the wavelength (about few meters) is larger than the size of the emitting region and the emission should be coherent. The flux of the radiation must quadratically grow with the number of particles rather than linearly.

Though already pointed out in the seventies [8] as a possible mechanism, the coherent geosynchotron effect [26] has found more detailed attention as the origin of radio emission of EAS [12, 13] only in recent years, and it has been proposed as the main mechanism for radio wave generation in EAS. The emission is explained to be arising by the deflection of the electrons and positrons in the Earth's magnetic field, inducing synchrotron radiation. This effect has been recently studied in detail by Monte Carlo simulations [15].

In the following the LOPES experiment is described, which is motivated to establish unambiguously the existence of radio emission from EAS and to study the gross features of the phenomenon. This recent revival of the interest is coupled with the advent of advanced electronic devices for detection.

4. The LOPES experiment

4.1 Layout

The LOPES experiment is a digital antenna array, sensitive in the frequency regime between 40-80 MHz, designed as a prototype for the astronomical digital telescope LOFAR (LOw Frequency ARray) complemented all across Northern Europe. It is located at the site of the KASCADE-Grande experiment at Forschungszentrum Karlsruhe (now: Karlsruhe Institute of Technology (KIT), Campus North), which provides the well-calibrated trigger information with cosmic ray air showers properties, needed for the reconstruction of the radio pulses. KASCADE-Grande is a traditional particle detector array (KArlsruhe Shower Core and Array DEtector-Grande) measuring the air showers in the primary energy range from 10^{14} to 10^{18} eV. The LOPES antennas are triggered by the particle detectors, first of the original KASCADE experiment [27], later on also of the KASCADEGrande set-up [18]. The latter allows the extend of studies to higher energies of the EAS primaries.

In Fig. 4.2, the KASCADE-Grande array is shown. The KASCADE experiment [28] detects the electrons, photons and muons outside the core region of extensive air showers in 252 detector stations on a rectangular grid of 13 m spacing, hence forming an array of $200 \times 200 \ m^2$. The array is organized in 16 clusters of 4×4 stations each, and the LOPES event selection is invoked when an 10/16 cluster trigger from the array is available. An access to measurements of higher energy air shower particles is possible with the Grande array due to the large number of scintillation stations covering an area of approximate $700 \times 700 \ m^2$ ($0.5 \ km^2$) next to the KASCADE array in order to operate together. As an extension of the KASCADE experiment running successfully since 1996, the Grande array has been realized by 37 stations located in hexagonal grids with an average distance of 140 m [14, 29]. Each Grande station is equipped with 10 m^2 of scintillation counters and the electronic components. A central data acquisition station (DAQ) collects the data from all stations and generates a valid experiment trigger. The signals are sent to it via 700 m long coaxial cables. In the DAQ, the analog signals of all 37 stations are digitized corresponding to the energy deposited in each station. The Grande array is divided for trigger purposes into hexagons of 7 stations (6 on the perimeter and 1 in the center), forming in total

18 clusters. The Grande event selection is invoked whenever a 7/7 (7 stations out of 7 of one hexagon have been fired) trigger coincidence from Grande is present. For exploring further applications of the radio technique at the Pierre Auger Observatory, inside the field the $LOPES^{STAR}$ (a Self Trigger Array of Radio detectors for LOPES [30]) test arrangement has been installed (see Fig. 4.2). A beacon antenna (see Fig. 4.3) can also be seen placed nearly at the center of the KASCADE-Grande array, which is used in the phase-delay calibration of the LOPES antenna.

The LOPES experiment was built to study whether radio emission from cosmic ray induced air showers is unambiguously detectable and to which extent it provides useful aspects for modern cosmic ray experiments. Compared with the historical experiments [8], it has an order of magnitude increase in bandwidth and time resolution, with effective digital filtering methods, and for the first time true interferometric imaging capabilities. The electric field of the radio emission is coherent and the good correlation of an air shower emitted pulse with the shower's geomagnetic angle suggests that the emission originates from the interaction of the EAS with the Earth's magnetic field.

The goal of LOPES is first the proof-of-principle with an understanding of characteristic features of the radio signal and of the emission mechanism. For this measurements of the polarization of the radio waves play an important role (see Chap. 6). The particular aims of the LOPES experiment are the following:

(i.) understanding the correlations of the recorded radio signal with the parameters of the observed EAS;

(ii.) exploring the sensitivity to the direction of shower incidence (i.e. angular dependence);

(iii.) exploring the dependence of the recorded radio signal on the energy and mass of the primary;

(iv.) verifying the suggested geo-synchrotron emission mechanism;

(v.) exploring the aspects for large scale application of the radio detection technique;

The antennas for LOPES are of short dipole type with an inverted V shape (Fig. 4.1). It consists of commercial PVC pipes holding the active parts. The radiator is consisting of two 102 cm long copper cables reaching from the top down at two sides of the pyramid. The layout of the LOPES antennas inside the KASCADE-Grande array is displayed in Fig. 4.2.

The LOPES experiment started its measurements in 2004 initially with 10 antennas, LOPES-10 arranged in the east-west polarization direction only [31, 32]. The antennas were devised for recording the radio emission of air showers generated in the Earth's atmosphere. After one year of taking data, the team of LOPES experiment has proved the existence of short radio pulse-like emission originating in EAS, see [13]. Later on, the array was extended by 20 more antennas forming LOPES-30, see [33, 34]. By the end of 2006, the set-up has changed to dual-polarization measurements, LOPES-pol, see [35]. The studies of this work are focussed on the polarization of the radio emission, comprising the measurements and their analysis.

Figure 4.1: A LOPES antenna at the site within the field of the particle detector array KASCADE-Grande.

4.2 Calibration

The array of 30 digital radio antennas has an absolute amplitude calibration [36] in order to estimate the electric field strength of the short radio pulse generated by air showers. To perform the calibration, a commercial calibrated radio source is used as emitter at the top of each LOPES antenna which is measuring an artificially triggered event. All environmental effects like ground characteristics, atmospheric temperature and the set-up systematics are included. The emitter is a movable bi-conical reference antenna which is linearly polarized and has a nearly constant directivity near its principal axis. We perform several calibration campaigns per year. Because of the changes in the atmospheric conditions antennas might be sensitive to difference in temperature and humidity. The calibration data are analysed and the absolute amplitude factor is being calculated per individual antenna channel (see Fig.4.4(a)), considered afterwards in the calibration table of the LOPES/LOFAR software tools which is used in data analysis for the pulse height reconstruction. Having the absolute amplitude value, we obtain the field strength in the range of 0-100 μV/m/MHz, which is comparable with the simulated radio pulse by a Monte Carlo code based on sophisticated electrodynamics calculation.

Besides the amplitude calibration, each single antenna has a time accuracy of 1 ns [25]. We use a transmitting reference antenna, a Beacon, which continuously emits sine waves at known frequencies (63.5 MHz and 68.1 MHz), and a pulse generator which emits a pulse at a fix known time. For LOPES, as a digital interferometer, the relative delay timing between the different antennas is of importance (e.g. Fig. 4.4(b)), because the absolute time of an air shower event has to be precisely known for the matching between LOPES events and the corresponding KASCADE-Grande events. Variations of the relative delays between the antennas can be detected and corrected for, at each recorded event by measuring the phases at the beacon frequencies (e.g. Fig. 4.4(c)). Thus having both, the amplitude and timing calibration, the instrumental delay corrections are applied to measured data. This allows a proper
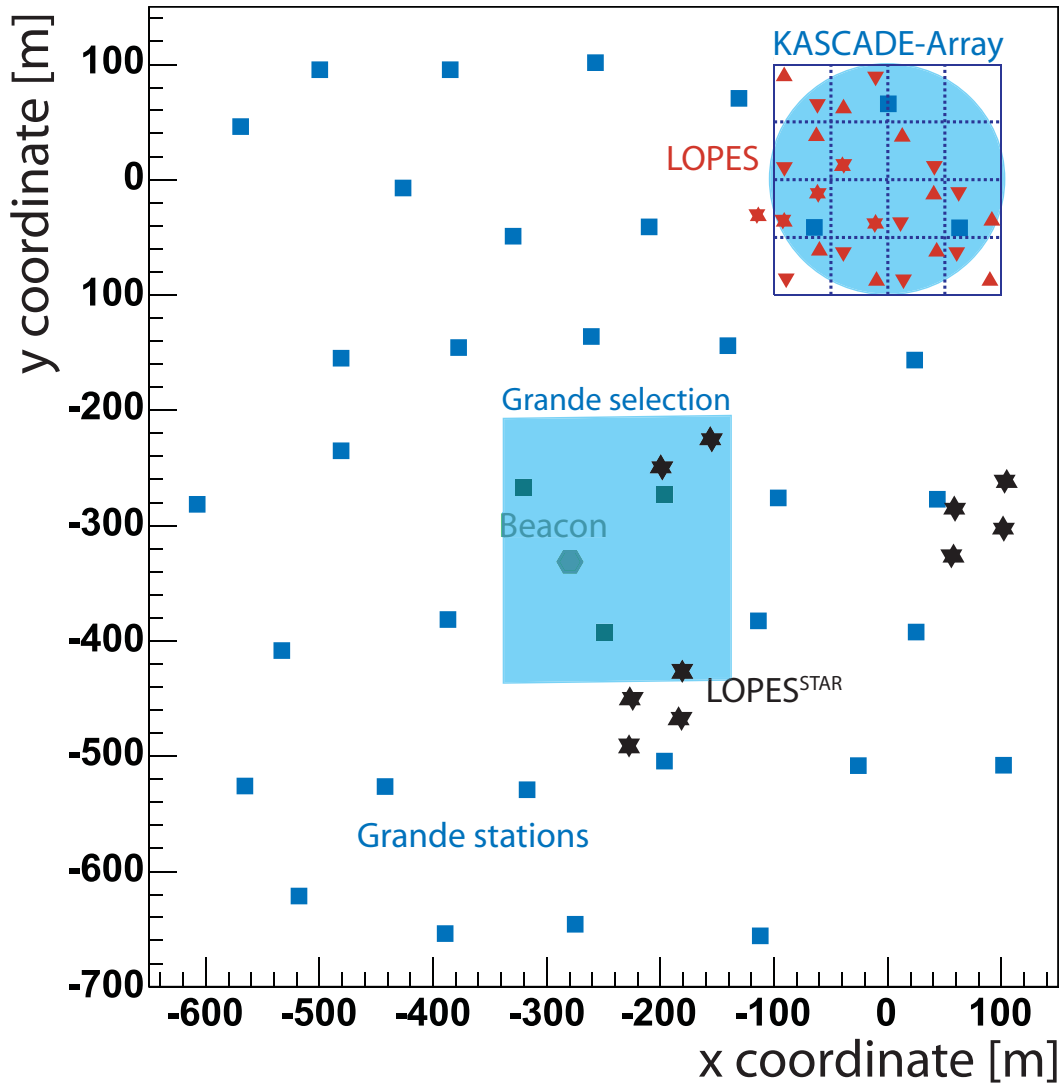
Figure 4.2: Layout of the KASCADE-Grande particle detector array at Forschungszentrum Karlsruhe. Included are: the LOPES antennas in the dual-polarization set-up, the self-triggering designed $LOPES^{STAR}$ antennas and the beacon antenna. The circle, left side up corner, represents the KASCADE selected area. The rectangle middle side represents the Grande selected area.
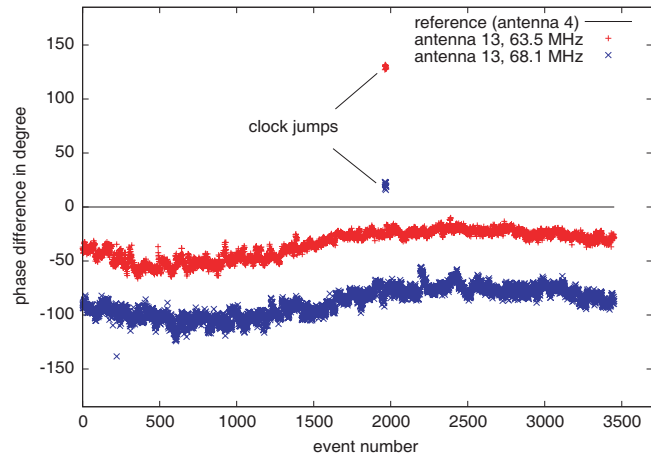

Figure 4.3: The beacon dipole antenna used used to monitor the timing from LOPES
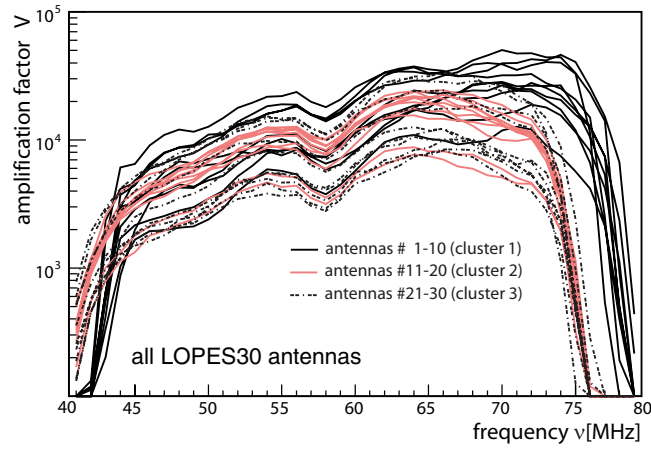
(a) The amplification factor
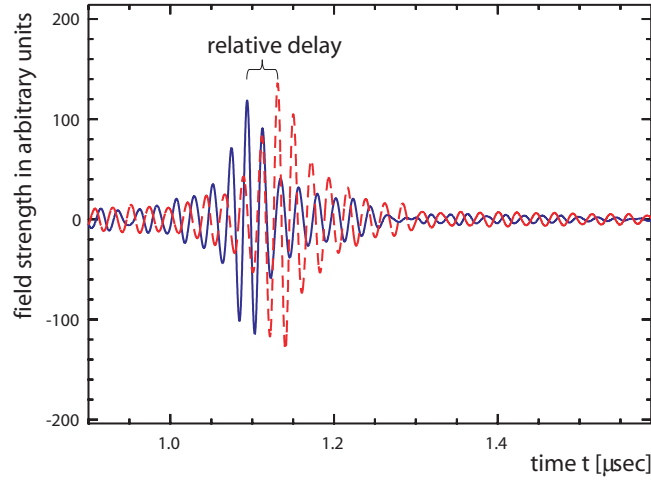

(b) The relative delay

(c) The phase difference

Figure 4.4: (a) Antenna amplification factors; different colour and line type separate the three antenna clusters with the individual electronics. The relative delay is mainly caused by different filters. (b) Relative delay between two antennas measured as the difference of the times when a calibration pulse is received, which has a height of about 1 V and is fed directly into the antenna cables. The relative delay is mainly caused by different cable lengths. (c) Phase differences between two antennas at both beacon frequencies. The absolute value of the phase differences is not of relevance; the changes are of about 1.5 ns ($\sim 35°$) between summer and winter.
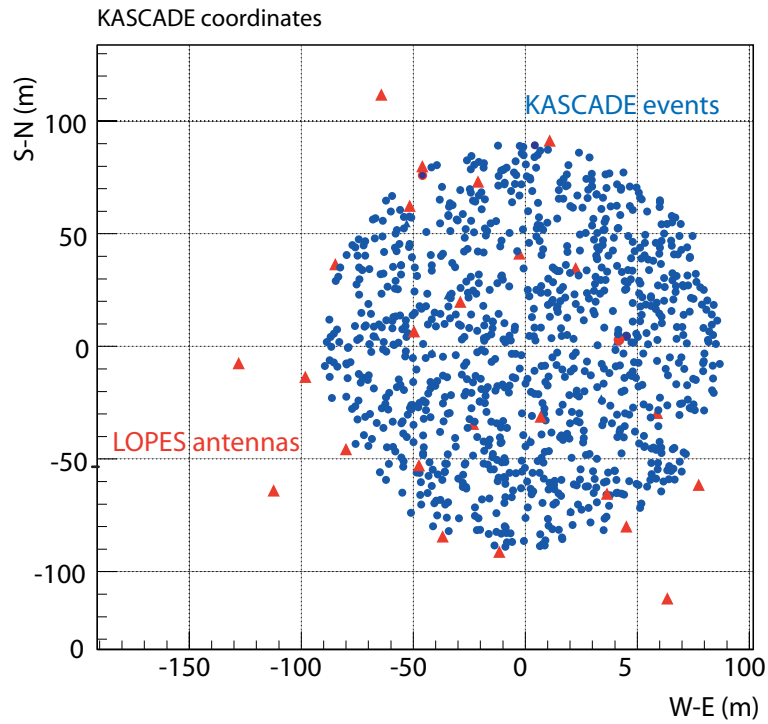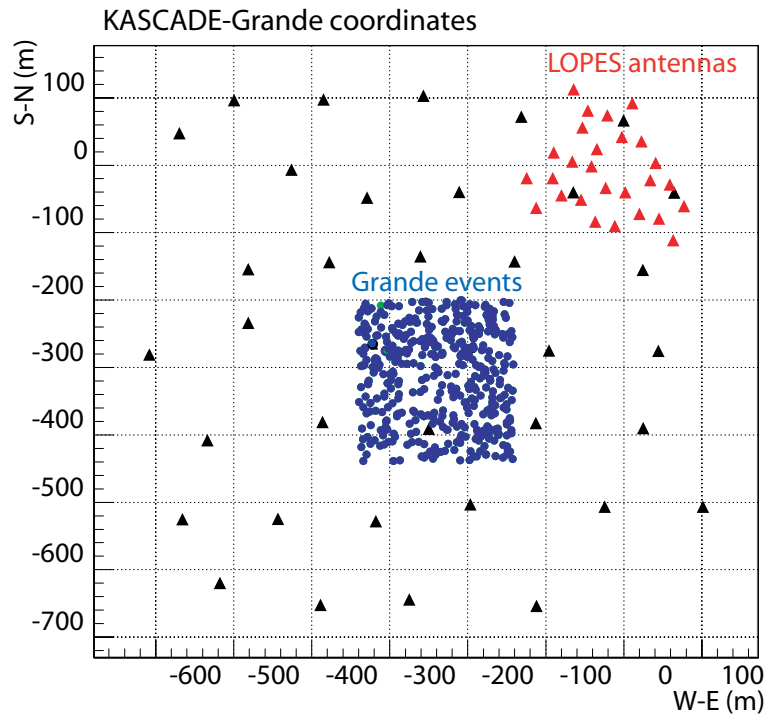
(a) Selection of shower cores for KASCADE
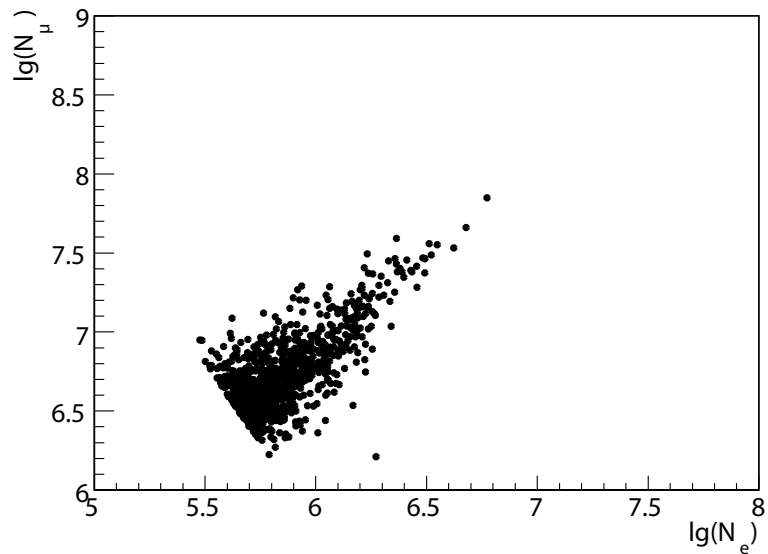
(b) Shower size distribution

Figure 4.5: (a) Layout of the selected KASCADE events within 90 m radius, and the LOPES antennas. Circles represent the shower cores falling inside KASCADE. Triangles represent the LOPES antennas. (b) Two dimensional shower size distribution (of 976 entries) with electron number N_e and muon number N_μ as reconstructed by KASCADE.

(a) Selection of shower cores for Grande
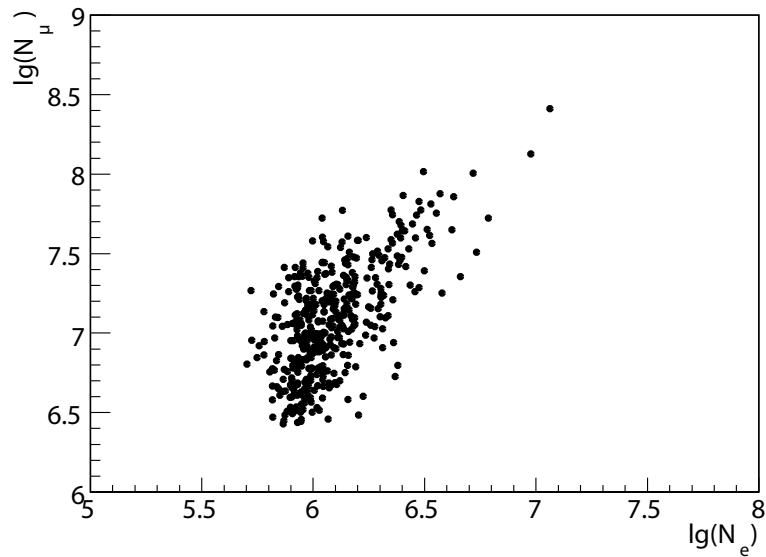
(b) Shower size distribution

Figure 4.6: (a) Layout of the selected Grande events (circles) at about 100 m distance from the LOPES antennas (triangles). (b) Two dimensional shower size distribution (of 417 entries) with electron number N_e and muon number N_μ as reconstructed by Grande.

Table 4.1: KASCADE and Grande trigger/event selection

Data selection for zenith angle less than 40 deg.		
Info	KASCADE	Grande
Events	976	444
Energy/eV	$10^{16.5}$ - $10^{17.8}$	10^{17} - $10^{18.5}$
Area/m	circle of 90 m radius	rectangle (-140, -340, -200, -440)

reconstruction of the field strength coherently seen in all non-flagged antennas at a precise time of about -1.8 μs, as shown in Fig. 3.2 of Chap. 3.

4.3 Data selection

The data selected for further processing of observed radio emission prefer EAS of primary energies around 10^{17} eV. That means EAS triggered by the KASCADE-Grande array, are considered with electron sizes $N_e > 10^5$ and muon numbers $N_\mu > 10^6$. Furthermore the cores of EAS of interest must fall into a fiducial area (see Figs. 4.5(a) and 4.6(b)) i.e with a circular area of 90 m radius inside the KASCADE field or for the Grande array within a distance > 100 m from the LOPES antenna array with zenith angles of incidence $\leq 40°$. For some special consideration also EAS with angles of incidence $> 40°$ are considered [37].

Two different selections are indicated by Figs. 4.5 and Figs. 4.6 and Table 4.1. Fig. 4.5(a) shows the distribution of the EAS cores within the chosen fiducial area of the KASCADE array, whenever 10 of 16 detector clusters have fired. Fig. 4.6(a) displays the distributions within a rectangle area outside the LOPES antenna array (about 100 m away). Whenever the trigger coincidence from the stations 9, 10, 13 which are located inside the chosen fiducial Grande array occurs, the trigger from Grande takes place. Figs. 4.5(b) and 4.6(b) present the corresponding correlated $N_e - N_\mu$ distributions (in the case of Grande, N_e is extracted from the relation $(N_{ch} - N_\mu)$).

4.4 Reconstruction

The standard reconstruction procedure for the analysis of air shower events with radio emission is implemented in the current version (C++ based) of the LOPES analysis software. It is implemented as part of the LOFAR software tools. It includes the correlation of the LOPES and KASCADE-Grande events with a selection of showers of high energy. The signals experience a Fast Fourier Transformation (FFT), a filtering for the effective wave band (43-74 MHz), correction of instrumental properties, suppression of narrow band radio frequency interference (RFI), up-sampling, and a inverse FFT. Finally by interferometric crosscorrelation a beam in the direction of the EAS incidence is formed.

Radio waves are propagating electromagnetic waves in vacuum or in matter. They consist of electric and magnetic field components which oscillate in phase perpendicular to each other and perpendicular to the direction of propagation. Practically,

a LOPES antenna sensitive to a certain direction of polarization of the electric field receives an electromagnetic wave (a radio signal) and transforms it into an electric signal (an impulse). It is amplified with a low noise amplifier and is processed with a first filter. The signal is sent via coaxial cable (100 m or 180 m long) to an RCU (Receiver and Conversion Unit) where it is amplified and filtered in the frequency band of 40-80 MHz. Analog data are digitised (1 Gbit/s) and optically transmitted to a memory buffer (TIM Module), where they are selected out by the trigger signal feeding for further storage a central data acquisition (DAQ) PC. A unique global time is used to match synchronized events. These events passed the trigger condition: 10 out of 16 clusters to be fired for KASCADE, and cluster numbers 9, 10, 13 to be fired in coincidence for Grande. Only events of the highest energies (above $10^{16.5}$ eV) are of interest for LOPES. Although the triggered events (~ 2 per min.) are of relatively high primary energy, a detectable radio signal is not expected in the all candidate events. For the events of interest one makes a selection based on air shower parameters, like if the shower cores are fallen inside a reliable fiducial area (see Fig. 4.2), large shower sizes. The LOPES events are combined with air shower candidate events based on a unique time-stamp. These results are listed. The list is used as input for the pulse height reconstruction. The reconstruction procedure results finally in the quantified pulse height.

For the reconstruction of the radio signal, we first apply a Fourier transformation to the signal traces in the time domain (to a spectrum in the frequency domain), where main part of the signal processing takes place. Particularly, instrumental delays of the different antennas have to be known with good accuracy. Small errors in the relative delays described by the antenna responses degrade the coherence of the signal (see Fig. 4.4(b)). Furthermore, each single antenna has an absolute amplitude calibration and a phase-delay calibration (see Sec. 4.2). Thus, the relative delays between antennas can be corrected and the coherence of the pulse can be achieved. The absolute amplitude calibration leads to frequency-dependent amplification factors (see Fig. 4.4(a)) which represent the amplification of the electronics and the time delay as major corrections for each antenna signal response. By these calibration procedures variations between different antennas are corrected. These corrections are applied to the measured signal, resulting in the true electric field strength which can be compared to the values predicted by simulations (which will be discussed in the following Chapters). Nevertheless, for LOPES as a digital interferometer, the relative timing between the different antennas is of importance, and the absolute time of an air shower event has to be known for the matching of LOPES with KASCADE-Grande events. Remaining differences are estimated to be about 20% in amplitude, which provides a first estimate of a systematic uncertainty in the measurements.

Since various noise components are present at the LOPES experiment, we have to correct for the narrow band RFI which occupies only few channels in the frequency band of 40-80 MHz, while a short pulse (tens orders of nanoseconds) of an EAS emitted signal is spread over all frequency channels. So by flagging the channels with RFI one can greatly reduce the background noise without affecting the air shower pulse much. After RFI suppression the noise level inside our frequency band is nearly flat [38]. However, to maintain the DAQ system of LOPES we monitor the mean noise level from all antennas (see Fig. 4.7). Thus, antennas are flagged in case of one of the following conditions:

(a) Good antenna response   (b) Bad antenna response
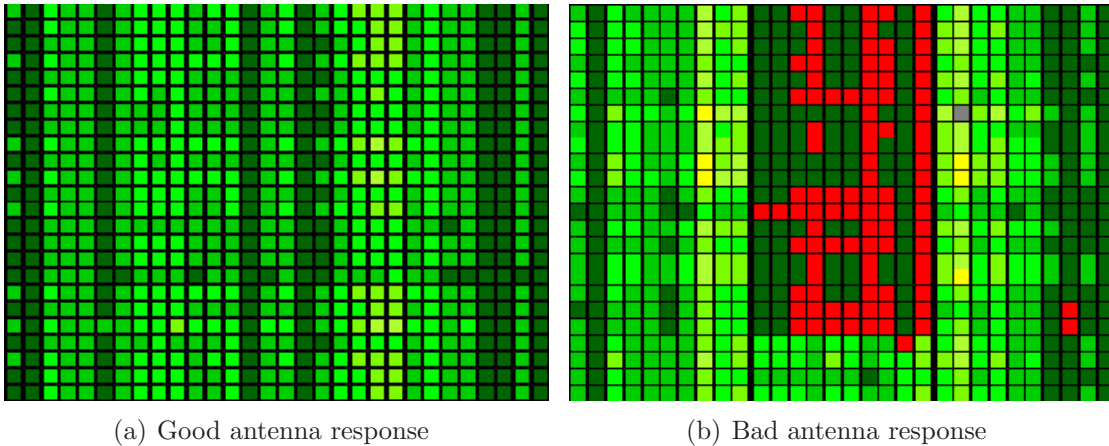
Figure 4.7: The graphical overview shows colour coded the mean noise level in all LOPES antennas (x-axis: antenna number from 1 to 30) for one day (y-axis: 1 hour per bin). The left panel shows a day of well operating antennas. The right panel shows a day with problems at the power supply of DAQ 9902 and a low signal recorded at Ant.28 for two hours.

(i.) They have an unusual amount of noise, i.e. their noise level is significantly larger than those of the other antennas; e.g., they are standing next to the KASCADE muon tracking detector and the shower core falls on top it. In this case lots of particles penetrate the shielding of the detector and the detector generates a large amount of RFI.

(ii.) They have an extremely small signal, e.g. because they were not connected or badly connected;

(iii.) They have bad timing, because of calibration failure. Thus, we make the pulse height reconstruction more reliable from the detector view point, once none of the considered antennas are dominantly affected by the noise or any other technical difficulty.

The radio signal is filtered by a band-pass filter and digitized with 12-bit ADCs (sampling rate 80 MHz), allowing afterwards 2nd Nyquist sampling of the signal. The response of the analogue electronics to a short pulse is an oscillation over a short time period. The major contribution to this oscillation comes from the band-pass filter: filtering of the lower frequencies causes an oscillation around zero amplitude, while the finite bandwidth broadens the pulse. If such a signal is sampled at 80 MHz (12.5 ns) some of this fine-structure is not visible any more. As the interferometric beam forming is sensitive to this fine structure it is useful to reconstruct the full structure by up-sampling (e.g., at 640 MHz as used for this analysis) and block averaging, which helps in improving accuracy of the pulse height. This is done by zero-padding method in the frequency-domain, i.e. by constructing an artificial dataset with a higher sampling frequency (and thus larger bandwidth) and then filling the frequency bins for which data are available with the measured data and all other bins with zeros. After applying the Fourier-transformation back into the time domain one has the correct interpolation of the data. The beam forming is done into the direction of the air shower given by KASCADE or Grande trigger source, depending on the shower selection. The beam forming is optimized by three shower
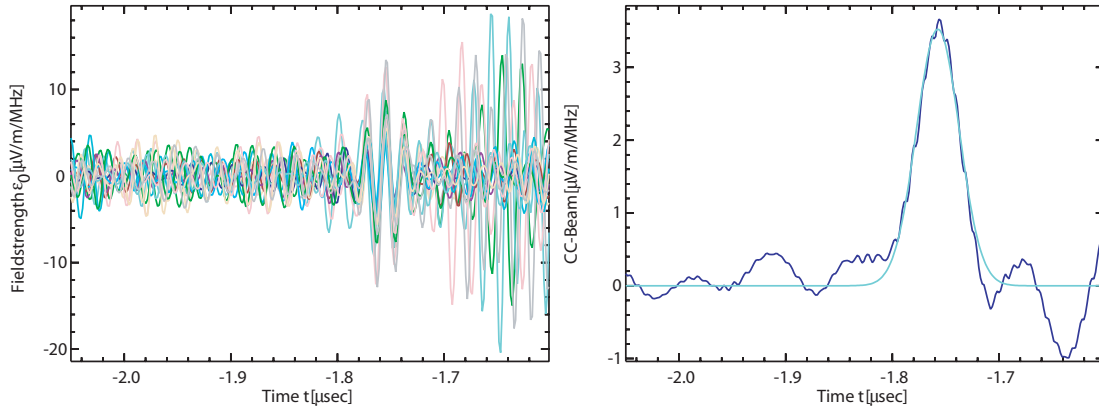
Figure 4.8: Example of a measured event, for which the reconstructed field strength (left panel) and the CC_{beam} (right panel) are shown. The CC_{beam} is fitted with a Gaussian function (light-blue line), which gives the height of the peak. The coherence of the radio signal can be observed in the range of -1.8 and -1.7 ns. The background noise visible later in the spectrum (after -1.7 ns) is caused by the excitation of the particle detectors at the place where the shower falls.

parameters: azimuth, elevation ($90° −$ zenith), and radius of curvature. The radio wave front of an air shower is not expected to arrive as a plane wave on the ground, since it has some curvature. During the reconstruction procedures the radius of curvature is taken into account by iterating a free parameter and the pulse height is evaluated on a small grid around the direction given by the KASCADE-Grande experiment until the pulse height is maximized. The position at which the pulse height has a maximum is then used as the starting point for a simplex maximization routine. This routine adjusts the three direction parameters, so that the pulse height is achieved. Practically, data from pair of antennas are multiplied, the resulting values are averaged, and then the square root is taken while preserving the sign. We call this the cross-correlation beam or CC_{beam} [38]:

$$cc(t) = \pm \sqrt{\left| \frac{1}{N_{\mathrm{P}}} \sum_{i=1}^{N-1} \sum_{j>i}^{N} s_i(t)s_j(t) \right|} \tag{4.1}$$

where N is the number of antennas, N_{P} the number of pairs of antennas, $s_i(t)$ the field strength of antenna i, and t the time-bin index. The negative sign is taken if the sum had a negative sign before taking the absolute values, and the positive sign otherwise. The advantage of the CC_{beam} is that a peak from a coherent pulse always has a positive sign (e.g. Fig. 4.8). Basically, the CC_{beam} is the radio observable of importance used in the further analysis.

4.5 The results of LOPES-30

The results of the LOPES experiment in the former configuration, preceding the studies of the polarization features, do already reveal the influence of geomagnetic angle pointing to the geomagnetic origin of radio emission from EAS. The geomagnetic angle is the angle between the axis of EAS incidence, deduced from the data of the observation of the cohabited particle detector array, and the direction v of the geomagnetic field vector, given by the local magnetic declination and inclination. At

the site of LOPES the Earth magnetic field is directed to the South ($\phi = 180°$ and $\theta = 25°$). Thus showers incident from South do experience only a relatively small Lorentz force.

There appears a correlation of the radio pulse height (CC_{beam}) with the primary particle energy inferred from EAS array data, additionally dependent from the geomagnetic angle and the distance from the shower axis. The average radio pulse height displays nearly a linear dependence of the primary particle energy [39], indicating the coherence of radio emission (see Fig. 4.9(a)). Even more, the radio pulse can be estimated by using the EAS observables only, as follows:

$$\varepsilon_{EW} = 11 \cdot (1.16 - \cos(\alpha)) \cdot \cos(\theta) \cdot \exp(\frac{-R}{236m}) \cdot (\frac{E_p}{10^{17}eV})^{0.95} \; [\mu V/m/MHz] \quad (4.2)$$

where the shower direction is defined by the geomagnetic angle α and the zenith angle θ; D is the distance from observer to the shower axis, and E_p the energy of the primary. Fig. 4.9(b) displays the correlation of the pulse height with geomagnetic angle α resulting from the analysis of the east-west polarized component only (as observed by LOPES-30). Maybe this is the reason for the not yet well explained phenomenological dependence of the radio pulse with $(1 - cos(\alpha))$.

Fig. 4.9(c) shows the results of the analysis of the field strength of an individual shower reconstructed from a single antenna. The lateral distribution follows an exponential decrease: $\epsilon = \epsilon_0 \cdot exp(-R/R_0)$ [40]. The scale parameter R_0 is determined phenomenologically and has a value of 100-200 m. Still no evidence is found for a correlation of R_0 with an EAS parameter. It has been shown [32] that the radio signal is detectable up to 500 m for EAS up to the primary energy of about 10^{18} eV. It was proven, the radio technique is capable to measure very inclined showers of zenith angles larger than $50°$, even at large distances from the shower cores [41, 37]. It should be mentioned that various studies [42, 43] have been directed to the influences of the strong electric fields of a thunderstorm, which imply considerable disturbances for the radio detection of EAS. Furthermore, the directional accuracy of radio antennas is in the order of $\backsim 1°$ [44]. The reconstruction of the arrival direction with LOPES is in agreement with the KASCADE reconstruction.
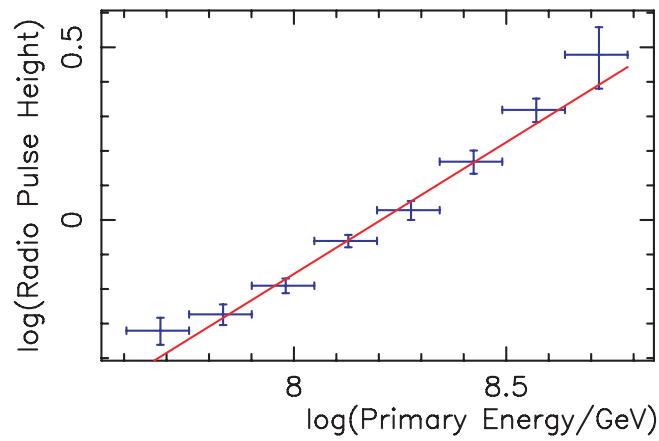
(a) Average pulse height vs. estimated EAS energy
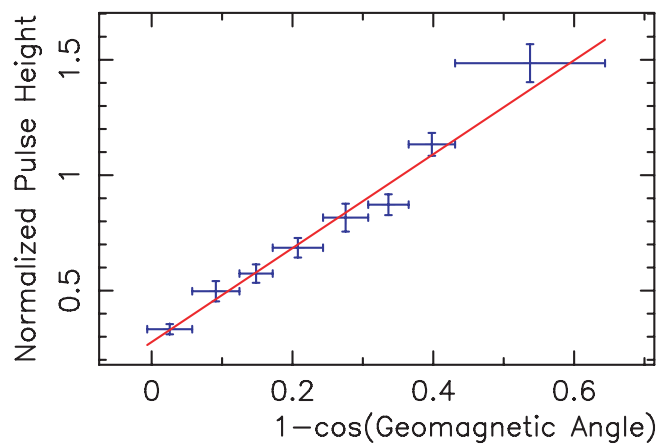
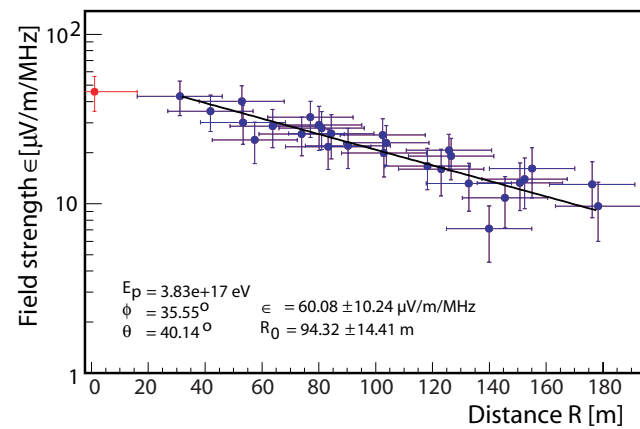(b) Average pulse height vs. geomagnetic angle

(c) Lateral distribution of the field strength for the distance R from the shower axis for an individual event

*Figure 4.9:* Some of the results of LOPES-30 [39, 40, 45]

5. Polarization studies

5.1 Theoretical motivation

Many researches have been concentrated on the understanding of coherent Cherenkov radio emission from the charge excess developing in high energy EAS [10]. The distinct influence of the geomagnetic angle on observed radio emission features, however, points to an alternative dominant mechanism, associated with the acceleration of charged EAS particles gyrating in the Earth's magnetic field: The geo-synchotron mechanism [12]. Positively and negatively charged particles are bent in opposite directions in a magnetic field and emit coherently synchrotron radiation. This is, in principle, a well understood effect and has to be applied to the specific geometry of developing air showers in the Earth's atmosphere. Thus it has been pointed out [46, 47, 48] that in a simplified consideration the synchrotron electric field produced near the axis of particle motion is to first order proportional to the cross product $\epsilon \propto \vec{v} \times \vec{B}$, where $\vec{v}$ is the direction of the EAS motion and $\vec{B}$ the geomagnetic field. There are various emission models, following the geomagnetic scheme, worked out in detail by Monte Carlo simulations [49, 46, 26, 15]. Corresponding Monte Carlo codes have been developed: The sophisticated Code REAS is based on ref. [26] and is usually combined with the air shower Monte Carlo simulation program CORSIKA [50, 51].

During the shower development an evolution of charge excess occurs (i.e. over abundance of e^- as e^+ annihilates with high probability), which leads to an additional radio emission (expected to be of $\approx$ maximum 10-20% of the geomagnetic emission). According to the simulations, the radio emission generated by the geo-synchotron mechanism is expected to be highly linearly polarized, perpendicular to the shower axis and the geomagnetic field. The simulations usually present the signal for two polarization directions of the electric field which clearly depend on the location of the observer relative to the shower axis; the closer the observer to the shower core, the stronger the radio signal, showing linear polarization. For a given zenith angle the polarization is directly related to the azimuth of shower incidence (i.e. the geomagnetic angle, the angle between the shower axis and the Earth magnetic field). Fig. 5.1 shows a simulated raw pulse of an air shower of azimuth 135°, zenith 44.5°
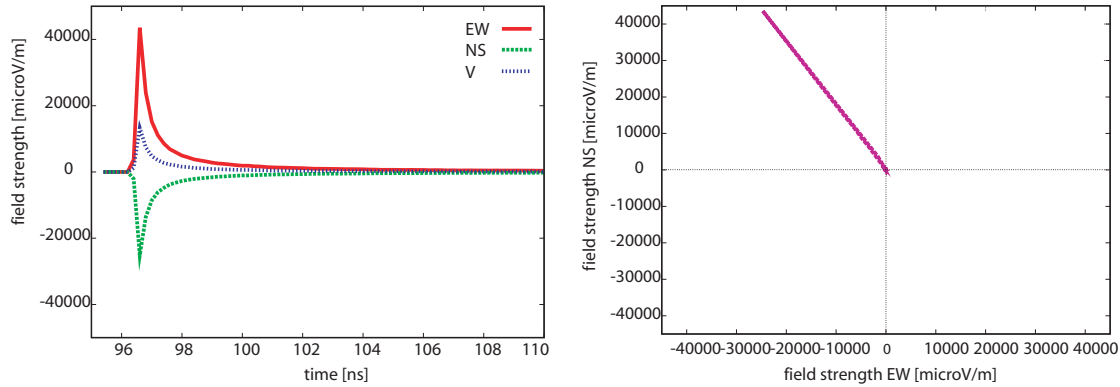
(a) Time-wise synchronized appearance of east-west (EW) and north-south (NS) polarization components (V, the vertical component).

(b) Linear polarization constructed from the EW and NS components of the field showing the coherence of the radio signal

Figure 5.1: A simulated radio signal

initiated by a proton primary particle of energy $10^{17.5}$ eV. The observer is at the shower core, and thus the north-south and east-west polarization components are of similar strength and arrive mostly synchronously (a) showing a perfectly linearly polarized pulse shape (b). In the center regions where the emission is strongest, the polarization vector points in the direction perpendicular to the air shower and magnetic field axis.

The angle between the shower axis and the Earth magnetic field (see Fig 5.2), i.e. the so-called geomagnetic angle (top panel) increases with increasing zenith angle. For large zenith angles (in Karlsruhe) large geomagnetic angles are obtained mainly for showers arriving from the Northern hemisphere (bottom panel).

Assuming the simplified $\vec{v} \times \vec{B}$ model [52], Fig. 5.3 shows the calculated azimuthal variation of the relative contributions of the NS and EW components, including their ratio ($|\vec{v} \times \vec{B}|^{NS}/|\vec{v} \times \vec{B}|^{EW}$), for showers of 5 difference zenith incidence angles ($\theta = 10°, 20°, 30°, 40°, 65°$). Fig. 5.4 displays the dependence of P_v^{NS} and P_v^{EW} projections as well as their ratio P_v^{ratio} related to geomagnetic angle α. The maximum amplitude in each NS and EW polarization component is nearly 1, with generally a larger contribution in the EW direction. However, the remaining part is expected from the vertical component which is not treated here because of the LOPES set-up sensitive only to the EW and NS polarization directions of the electric field. Therefore, the ratio between the NS and EW polarization components is also displayed in order to have a quantity which shows only the polarization characteristics and is independently of amplitude or other shower parameters. The projections of the vector shows a very different behaviour with α and ϕ. The larger the zenith angle the clearer the feature characteristics become. In particular, when $\theta = 65°$ (i.e. the vector projection is parallel with the Earth's magnetic field) the increase in the range of the geomagnetic angle is clearly seen. In the case of P_v^{ratio}, characteristic features are observed too. With respect to the ϕ correlations, mainly showers arriving from the North ($270 < \phi < 90°$) are expected and fewer showers from the South ($\phi = 170°$), for $\theta < 40°$, while a decrease in the geomagnetic dependency for $\alpha > 30°$ is seen. We need to mention, that the simplified geomagnetic model dependency with the air shower geometry is treated independently of the primary energy or any other shower parameters.

Concluding the considerations of the polarization characteristics, based on the $\vec{v} \times \vec{B}$ model, we summarize that showers with the strongest signals will be registered perpendicular to the Earth magnetic field: from Northern directions for the EW polarization component and from East and West directions for the NS polarized signal. For a 65° inclined shower the contribution of the amplitude in the EW polarization direction becomes nearly 100%, while in the NS component the emission contribution is about 80% for showers coming from East or West (missing contribution to 100% is related to the vertical polarization component). It confirmed by data, this characteristic $\vec{v} \times \vec{B}$ -amplitude behaviour would give a strong indication of the geomagnetic origin of the radio emission from EAS.

5.2 Monte Carlo simulations

Full Monte Carlo simulations have been performed on a sample of 41 events (compiled in Table.5.1) for a detailed understanding of the radio signal in its polarizations. Thus, in order to have the radio signal simulated in EW and NS polarization directions, certain azimuth, zenith, energy ($10^{17.5}$ eV) and mass (in this case, proton) of the primary are given. The simulation procedure consists of several steps: 1st, the shower development in the Earth's atmosphere is performed with the CORSIKA code [50], which provides detailed information about electrons (e^-) and positrons (e^+) developed in the atmosphere; 2nd, the radio emission of the air shower is treated with the REAS3 code [15], which implements the geo-synchrotron model [26] by treating the emission as synchrotron-like radiation from the relativistic secondaries (e^-, e^+) deflected in the Earth's magnetic field. Additionally, REAS3 contains also contribution from the charge excess; 3rd, the simulated amplitude is filtered with the REASplot code in the frequency band of 43-76 MHz (the effective band of the LOPES experiment) per each EW and NS polarization component.

The aim here is to study whether the simplified geomagnetic model $|\vec{v} \times \vec{B}|$ can explain the behaviour of the full simulation of the radio emission, which also includes the charge excess. For detailed investigations, the simulated amplitude of a single LOPES Antenna (e.g. Ant-1) is compared with the $\vec{v} \times \vec{B}$ -amplitude. Ant-1 is located at about 80 m distance to the North-West direction from the shower core (see Table 5.1) located at the center of the KASCADE experiment, where the LOPES antennas are. From the (frequency-filtered) simulated amplitude on each polarization component of the electric field in dependence with the azimuth angle (see Fig. 5.5) it is see that for the EW polarization direction the highest amplitude is for showers coming from the North and South, and for the NS polarization direction the highest amplitude is mainly for showers coming from East and West directions (with a small contribution also from North and South, see top panel). From the correlation of the amplitude with the geomagnetic angle α, the increase of the signal amplitude in the EW polarization component with increasing α is observed. A different effect is seen in the NS component (i.e. a decrease for $\alpha > 45°$). The widths of the distributions are large, because of covering a large range of zenith angles (θ = 0° - 60°), e.g. Fig. 5.5 (top panels). From the ratio of the amplitude (ratio = $\epsilon^{NS}/\epsilon^{EW}$, see Fig. 5.5, bottom panels) almost the same characteristic features are observed as for the simplified geomagnetic ($\vec{v} \times \vec{B}$) model; for ratio > 0, dominant detection is expected from the NS polarization component and for ratio < 0, dominant detection is expected for the EW polarization component. Larger error bars
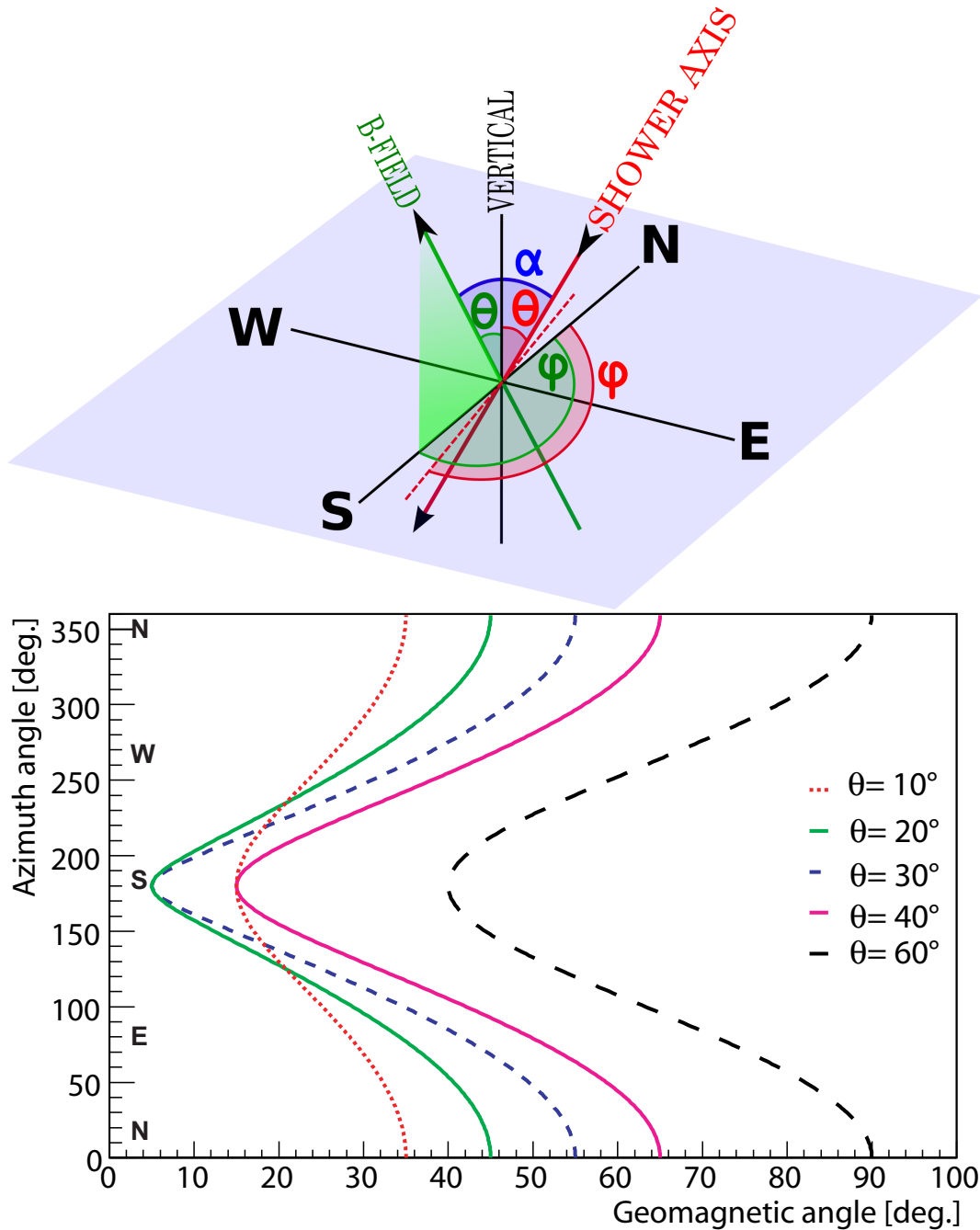
Figure 5.2: Top: Sketch of the axis of an air shower and of the Earth magnetic field of Northern Europe ($\phi = 180°$ and $\theta = 25°$). Included are the representative angles: azimuth (ϕ), zenith (θ) and geomagnetic angle (α). Bottom: An analytical calculation of geomagnetic angle for the full range of azimuth (0° - 360°) is applied. The dependence for different zenith (θ) angles is shown. One can see the geomagnetic angle increases with increasing zenith angle for same azimuth (more clearly seen in the Northern hemisphere).
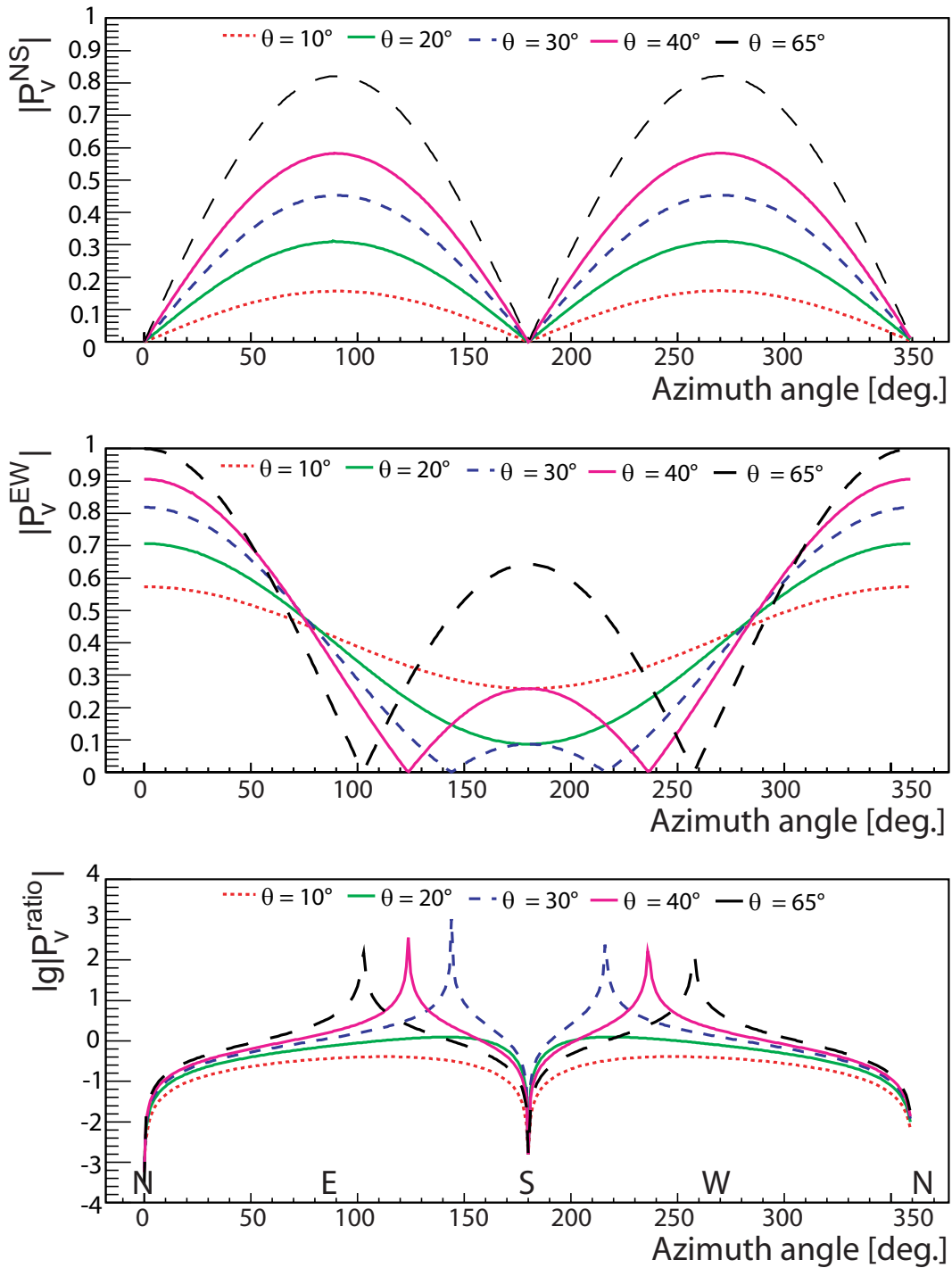
Figure 5.3: $\vec{v} \times \vec{B}$ model: relative contributions for the polarization components north-south (top panel), east-west (middle panel), and their ratio (bottom panel) vs. the azimuth angle calculated for different zenith angles.
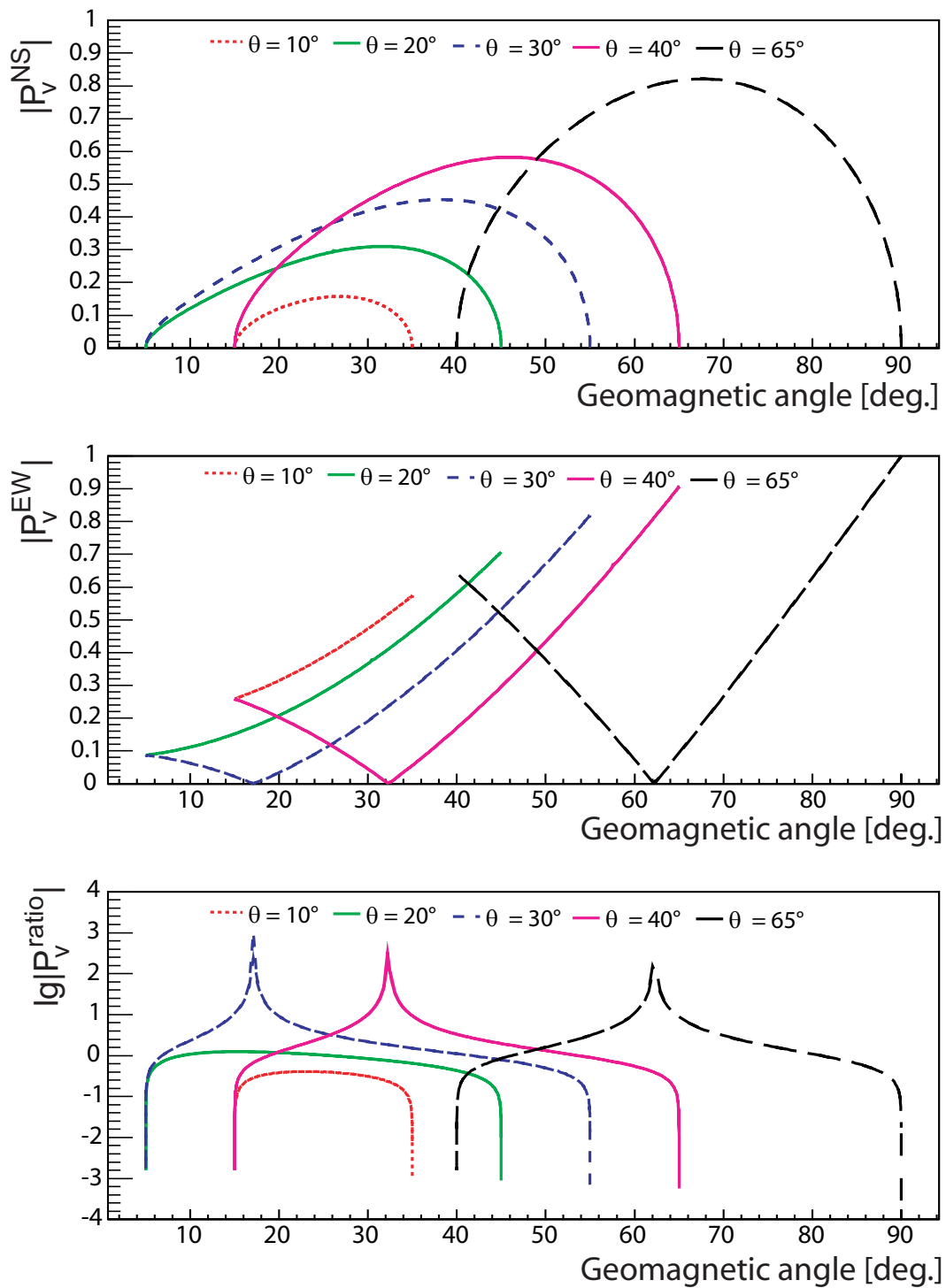
Figure 5.4: $\vec{v} \times \vec{B}$ model: the relative contributions vs. the geomagnetic angle.
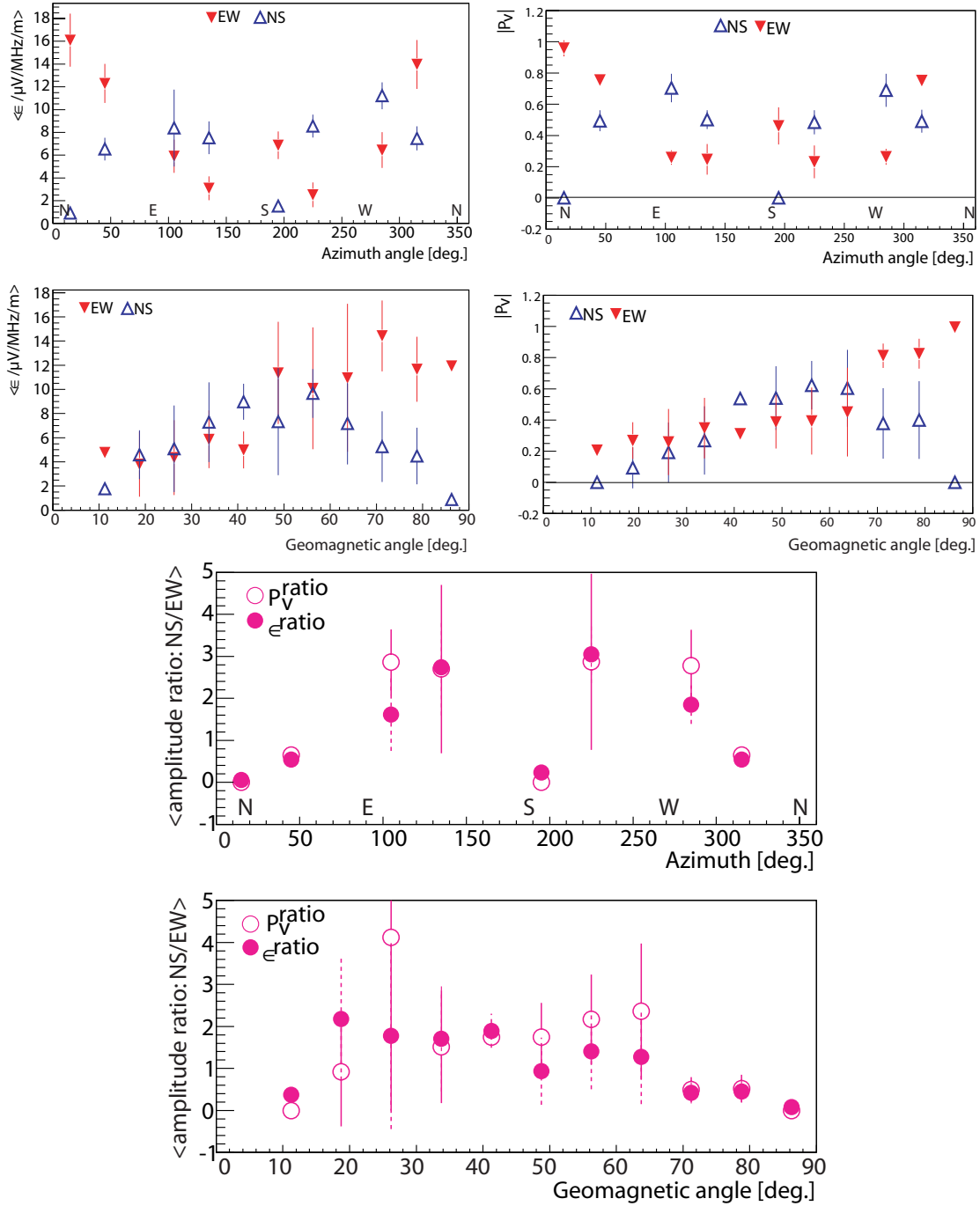
Figure 5.5: Correlation of the simulated (with REAS3 code, 80 m distance from shower core, left side - top panels) and analytical calculated (in terms of $P_v = \vec{v} \times \vec{B}$, right side - top panels) amplitude with azimuth and geomagnetic angles per polarization. The comparison between their amplitude ratio is shown at bottom panels. The error bars show the rms (root mean square) of the distribution inside the bin.
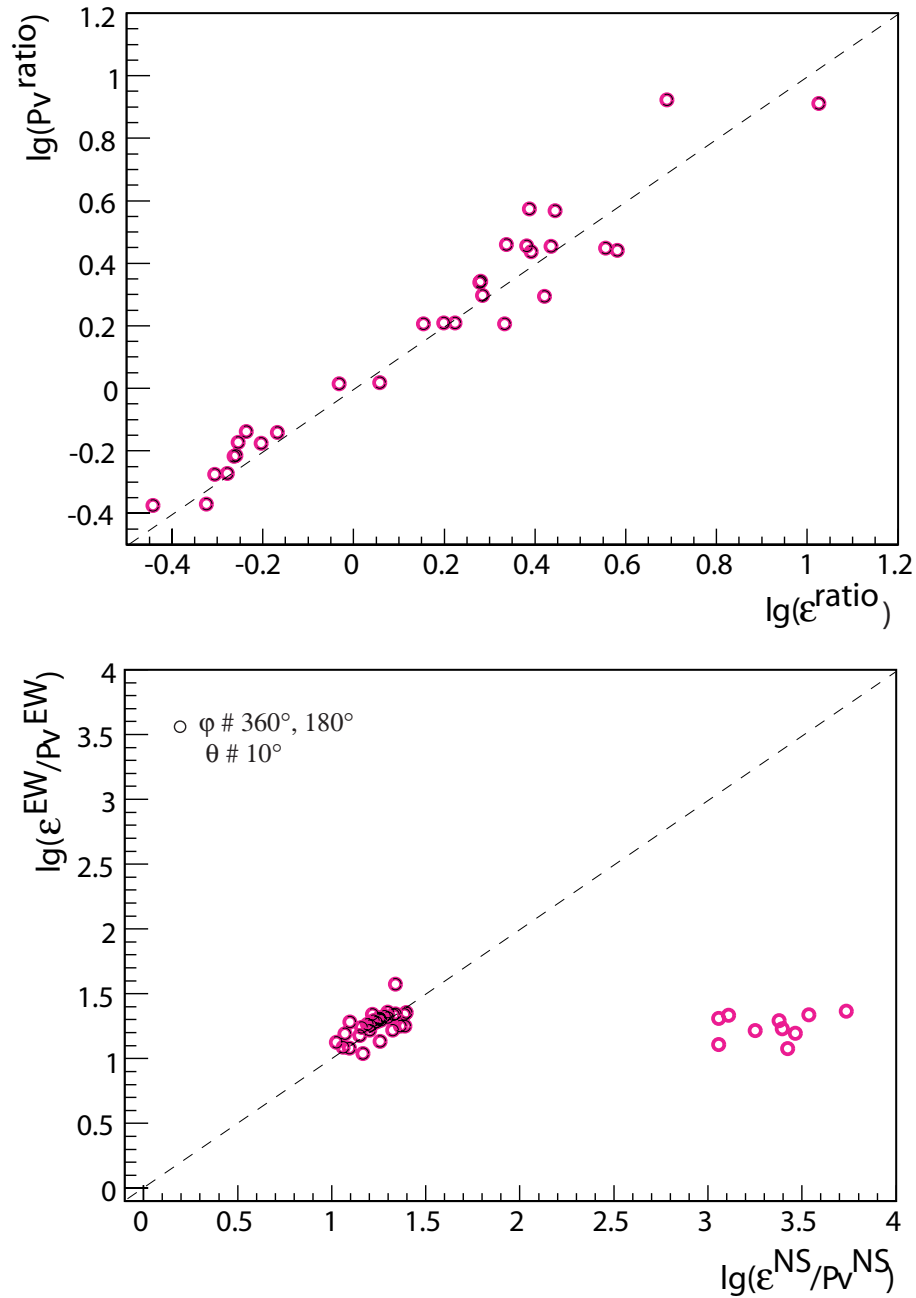
Figure 5.6: Top panel: Scatter plot between the ratio of $\vec{v} \times \vec{B}$ -amplitude and ϵ -simulated amplitudes (ratio=NS/EW polarization directions). A good agreement is found. Bottom panel: Ratio between the simulated amplitude (with REAS3 in the EW polarization) and $\vec{v} \times \vec{B}$ -amplitude (projected to the EW polarization direction): Y-axis. Same but for the NS polarization direction: X-axis. All sample of events is plotted (pink colour), which shows that showers coming from North and South directions are off to the side. Black colour depicts events of non-arrival directions from North and South.
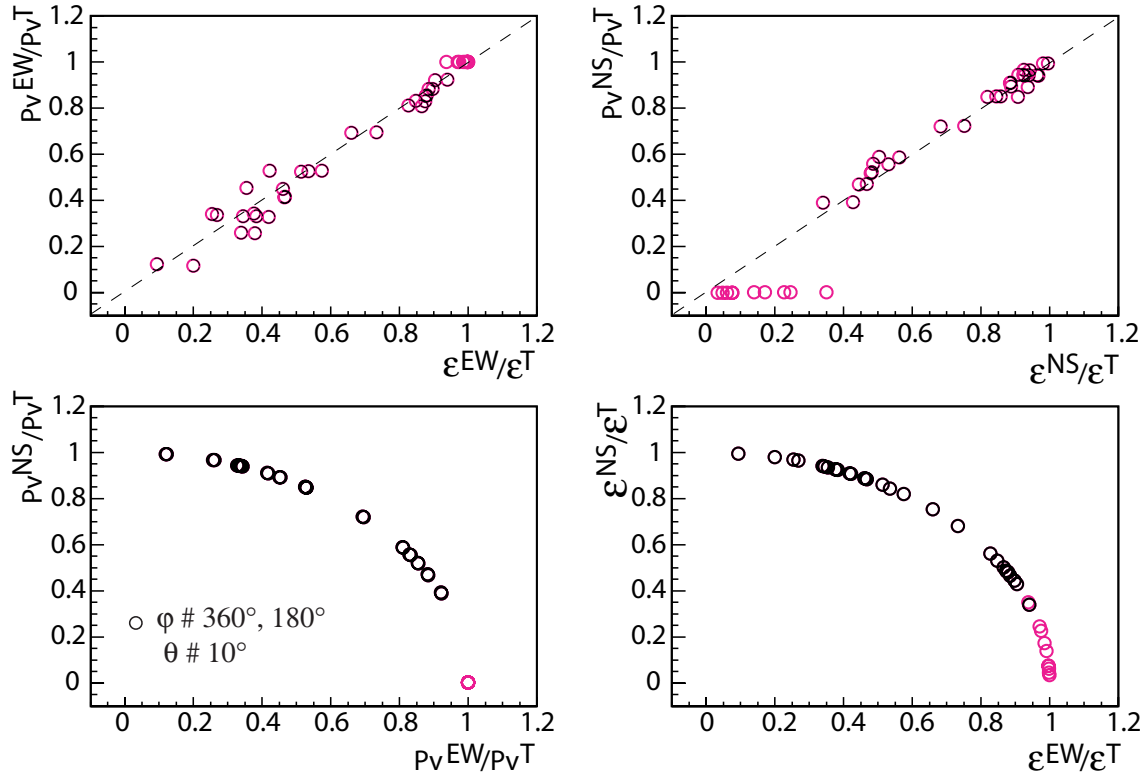
Figure 5.7: From left to right: scatter plot between $\vec{v} \times \vec{B}$ -amplitude in the EW polarization direction divided by the total amplitude and the ϵ -simulated amplitude in the EW polarization direction divided by the total amplitude. Same for NS polarization direction, for which case is observed that for incoming showers from Northern and Southern hemispheres, as well as for vertical showers ($\theta = 0°$), the polarization vector given by the $\vec{v} \times \vec{B}$ -amplitude projected to the North direction is zero, while the simulated corresponding amplitude is not. Lila circles show all events; black circles depict events of non-arrival directions from North and South.

Table 5.1: Input for REAS3 simulation of air shower radio emission. All showers are imitated by primary protons of an energy of $10^{17.5}$ eV.

No.	Elevation [deg.]	Azimuth [deg.]
1	90	0
2	64.1581	180
3	64.1581	135
4	64.1581	90
5	64.1581	45
6	64.1581	0
7	64.1581	315
8	64.1581	270
9	64.1581	225
10	53.1301	180
11	53.1301	135
12	53.1301	90
13	53.1301	45
14	53.1301	0
15	53.1301	315
16	53.1301	270
17	53.1301	225
18	44.427	180
19	44.427	135
20	44.427	90
21	44.427	45
22	44.427	0
23	44.427	315
24	44.427	270
25	44.427	225
26	36.8699	180
27	36.8699	135
28	36.8699	90
29	36.8699	45
30	36.8699	0
31	36.8699	315
32	36.8699	270
33	36.8699	225
34	30	180
35	30	135
36	30	90
37	30	45
38	30	0
39	30	315
40	30	270
41	30	225

The "Input REAS3" title spans above the No., Elevation [deg.], and Azimuth [deg.] columns.

are seen for showers coming from around South direction, i.e. hemisphere parallel with the geomagnetic field direction. Moreover, in the $\vec{v} \times \vec{B}$ -ratio is observed that for showers coming from North and South directions, including also vertical showers ($\theta = 0$), the amplitude is zero for the NS polarization direction only. However, this is not the case in the simulation, where a small contribution for the nS component is seen, even if the $\vec{v} \times \vec{B}$ model predicts it to be zero.

The ratio between the simulated amplitude and the $\vec{v} \times \vec{B}$ -amplitude, e.g. ϵ/P_v, per polarization is displayed in Fig 5.6. It can be seen there is not a well agreement for the complete data-set on both approaches (i.e. simulation and simplified geomagnetic model (bottom panel)). However, good correlation between their individual ratio (ϵ, P_v) is found (see top panel). This is the sign that, generally, the amplitude in term of ratio is in agreement between the simplified model and the full simulation. In few case, the relative contribution of the NS polarization component is not in agreement. In Fig. 5.7 are shown the distributions of the relative amplitude as given by simulation and by simplified geomagnetic model, where $\epsilon^T = \sqrt{\epsilon_{EW}^2 + \epsilon_{NS}^2}$, $P_v^T = \sqrt{P_{EW}^2 + P_{NS}^2}$. This is the only way to compare the amplitude as $\vec{v} \times \vec{B}$, where the pure geometry is used. Good agreement between $\vec{v} \times \vec{B}$ and full simulation is seen in the EW polarization direction, but different situation is found for the NS polarization (for events with certain shower geometry). It is observed that for the incoming showers from the Northern and Southern hemispheres the contribution of the $\vec{v} \times \vec{B}$ -amplitude is close to zero, while for the simulation is not. Also for vertical showers (i.e. $\theta = 0°$) the contribution of $\vec{v} \times \vec{B}$ -amplitude is zero in North-South. From the scatter plot between the normalized amplitudes per polarization component to the total amplitude, one can see that the contribution for the NS polarization is lower compared to the EW polarization. Moreover, in the simulations, showers coming from the North and South directions are detected in both EW and NS polarization directions. This contradicts, however, the $\vec{v} \times \vec{B}$ -model.

Concluding the theoretical investigations, almost the same feature characteristics are seen in the distributions of the simulated amplitude of a single LOPES antenna as for the simplified geomagnetic model. There is however an exceptional case for vertical showers as well as for showers coming from the North and South hemispheres. The correlation of the simulated amplitude (of each EW and NS polarization component of the electric field) with the azimuth and geomagnetic angles of the air shower predicts same feature characteristics as for the $\vec{v} \times \vec{B}$ -model (of which polarization vector is projected to each EW and NS polarization component, independently). Both approaches (simulation and model) describe remarkably well the angular distributions in both EW and NS polarization directions. Their results are almost in agreement when comparing their individual ratio of the amplitudes (NS/EW), e.g. Fig. 5.6, top panel. Same geomagnetic effect is treated in cases, except of the charge excess consideration in the Monte Carlo simulation only. It predicts detection in the NS polarization direction even from showers coming from Northern and Southern hemispheres, while the NS projection of the $\vec{v} \times \vec{B}$ -polarization vector becomes zero, but the relative contribution is in the order of 10% (see Fig. 5.7). However, both models support the role of geomagnetic effect in the radio emission mechanism of air showers and help in the interpretation of the measured radio signal. Detailed comparisons between measurements and these two analytical approaches are discussed in the following Chapter.

6. Measurements & Analysis

The studies of this work are focused to an improved knowledge of the radio signal. Of particular interest are the polarization characteristics. This is possible because of the well-known determination of EAS observables provided by the KASCADE-Grande experiment and the polarization measurements performed by the LOPES experiment. By measuring the east-west and the north-south components of the electric field, the geomagnetic effect of the emission is tested. Dependencies of the reconstructed CC_{beam} in each polarization direction on shower parameters like arrival direction, distance to shower axis or primary energy will be discussed in the following Sections, as well as the lateral extent of the field strength over the distance. Finally, for the first time for LOPES, the polarization vector of a dual-polarized antenna is examined.

6.1 Experimental Investigations

The radio signal is generally present in both components with a definite mutual relation predicted by the theoretical studies. In order to establish the emission mechanism and to increase the sensitivity of the measurements, in 2006 LOPES-30, sensitive to the east-west polarization component only, has been reconfigured to enable dual-polarization measurements by the following arrangement: 10 antennae were directed to be sensitive to the east-west (EW) polarization component, 10 antennae to north-south (NS) direction, while 5 antennae were devised with channels sensitive to both, EW and NS directions at the same place, recording at the same time both polarizations of the electric field (see Fig. 6.1). The usual observable we deduce from the measurements is the CC_{beam} (see Sec. 4.4).

Fig. 6.2 shows the total field strength seen by a dual-polarized LOPES antenna as a function of the angle between the polarization axes of the bi-conical reference source (used in the absolute amplitude calibration) and the LOPES antenna [36]. Each polarization direction is measured individually during the same campaign by varying the polarization angle of the reference antenna in steps of 10 degrees, and thus rotating the reference source in a vertical position at 11 m height on top of each LOPES antenna. No crosstalk between the channels was found. The results obtained proof that LOPES antennae are suitable for such polarization measurements.
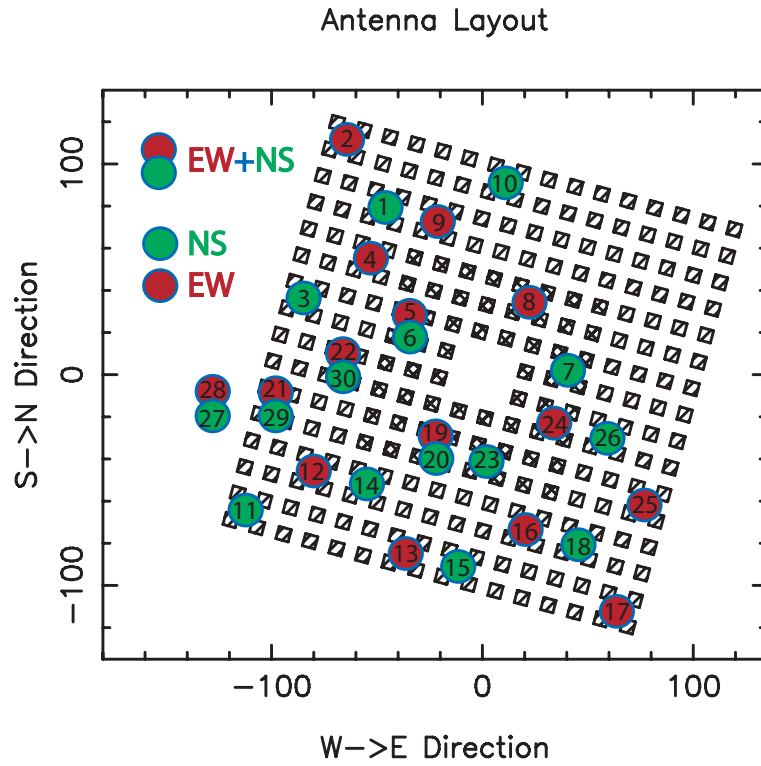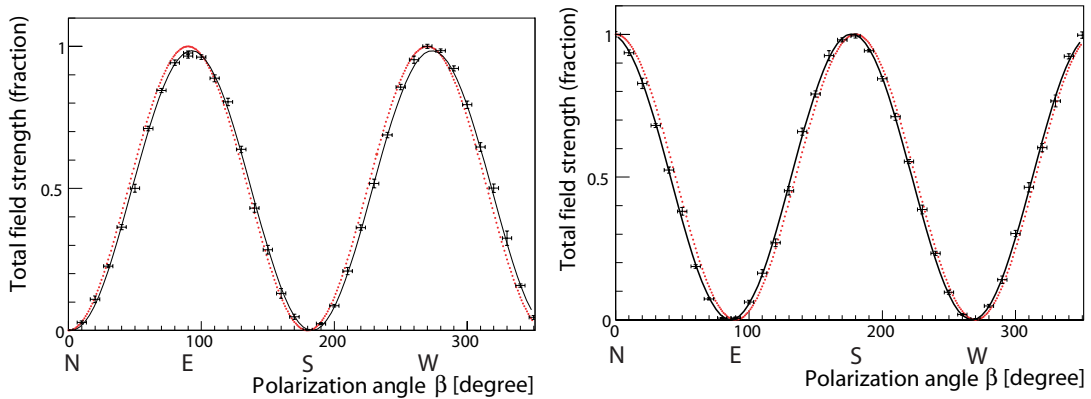
Figure 6.1: Layout of LOPES-pol inside the KASCADE-Grande area (see Fig. 4.2).

(a) East-West polarization direction. Dotted line: theoretical $\sin\beta$-distribution (normalized to the value at $\beta=270°$)

(b) North-South polarization direction. The dotted curve is normalized to the value at $\beta=180°$.

Figure 6.2: Fraction of the total field strength seen by each linearly polarized LOPES antenna as a function of the polarization angle β. Points: experimental data, solid line: data fit by a $\sin\beta$-function which fits very well data.

The experimental observation of this variation allows a verification of the situation discussed in Chapter 5. Detailed investigations of both, measured and simulated polarization components of the electric field are discussed in this Chapter.

6.2 First events measured with LOPES-pol

As an example, Fig. 6.3(a) shows one of the first events detected by LOPES in the dual-polarization configuration in December 2006. The KASCADE shower reconstruction results in a primary energy of 10^{18} eV, a geomagnetic angle (the angle between the shower axis and the Earth magnetic field) of 83°, an azimuth angle of 51° (i.e. coming from North-East), and a zenith angle of 66° for this particular event. The shower clearly shows signals recorded in both polarization directions of the electric field. The north-south (NS) and the east-west (EW) polarization components are of similar strength and arrive almost synchronously, as expected for a linearly polarized pulse. The figure shows the value of the reconstructed CC_{beam} which describes the average of the electric field strength for the mean distance from the shower axis.

As another example, Fig. 6.3(b) shows an event detected in December 2006 with a primary energy of $3 \cdot 10^{17}$ eV, a geomagnetic angle of 77°, an azimuth angle of 333° (i.e. coming from North, North-West), and a zenith angle of 54°. The shower shows different signals recorded in the EW and NS polarization directions. The observed differences are, however, explained by the individual projection of the $\vec{v} \times \vec{B}$ model to the EW and NS polarization directions (see Figs. 5.3, 5.4). For showers arriving from the North, we expect a higher signal amplitude detected in the EW polarization direction, and a lower signal in the NS polarization component.

These two selected events clearly show the capability of the LOPES experiment in recording the radio emission in both, the EW and NS polarization components. However, these events are very inclined, i.e. zenith angle $> 54°$, geomagnetic angle $> 77°$. They are good candidates for seeing the physical effects, but not very suited for the standard analysis, due to large zenith angles. The EAS reconstruction by the KASCADE-Grande experiment is of high accuracy for small zenith angles, e.g. $\theta < 40°$, only. Standard reconstruction of the radio signal requires events with accurate EAS reconstruction and thus, the geometry of the input showers is restricted to a range of zenith angles between 0-40 degrees.

6.3 Investigations of the CC_{beam} signal

The purpose of the CC_{beam} analysis is to examine dependencies of the measured radio signal on each polarization direction, independently, with respect to the air shower observables provided by the KASCADE-Grande experiment. As discussed in Sec. 4.4, from the reconstruction of the radio signal we obtain the quantified radio pulse height, the so called CC_{beam}, which is calculated per individual polarization, EW and NS directions, separately. Here is important that for each single event, the air shower geometry is the same for the reconstruction of the field strength in each polarization component.

As not every selected air shower event is accompanied by a radio pulse recorded by the LOPES experiment, one has to select the reliable events by validating the following aspects: existence of a pulse, coherence of the pulse and position in time of the
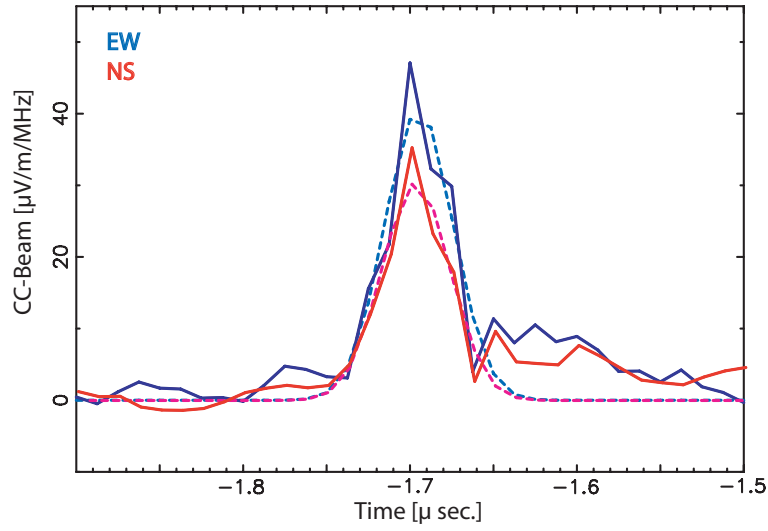
(a) The 1st event
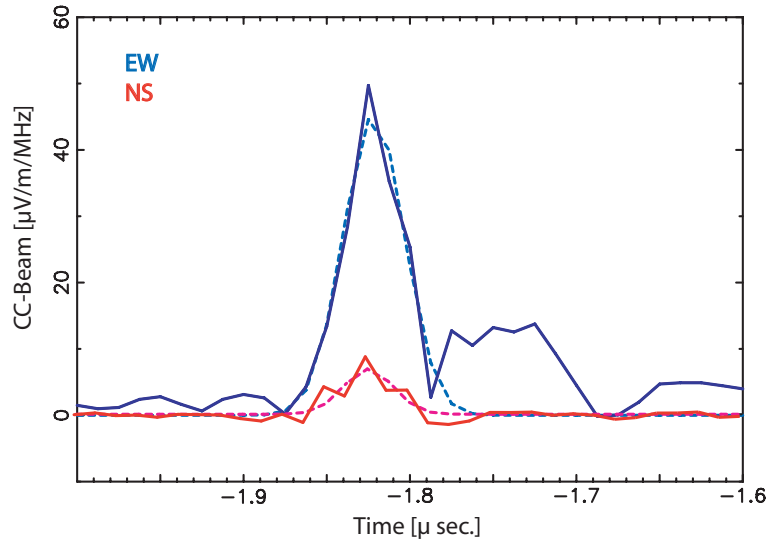
(b) The 2nd event

Figure 6.3: (a) First events seen with the dual-polarization set-up. One of them was registered by the end of Dec '06, of a primary energy of 10^{18} eV coming from North-East. One can clearly see very high radio signals recorded in both polarization directions, which prove the detection in both polarizations at the same time. (b) Another event example registered as well by the end of Dec '06, of a primary energy of $3 \cdot 10^{17}$ eV coming from North North-West. One can clearly see a dominant signal recorded in the EW polarization direction only. Both events have geomagnetic angles $\alpha > 70°$, and thus the amplitude of the signal is rather high (in agreement with the α dependency of $\vec{v} \times \vec{B}$ model). The full lines indicate the CC_{beam} of each polarization and the dotted lines the applied Gaussian fit, respectively.
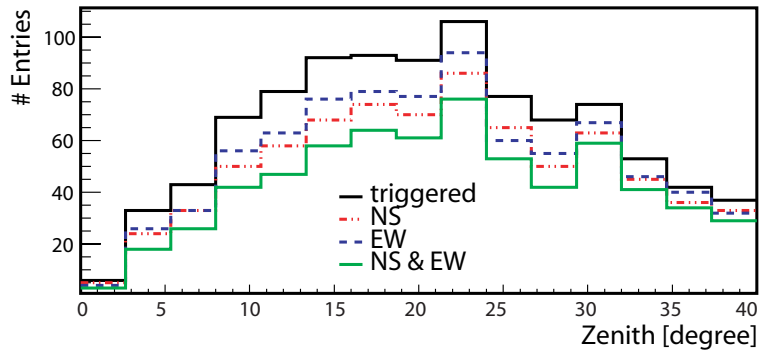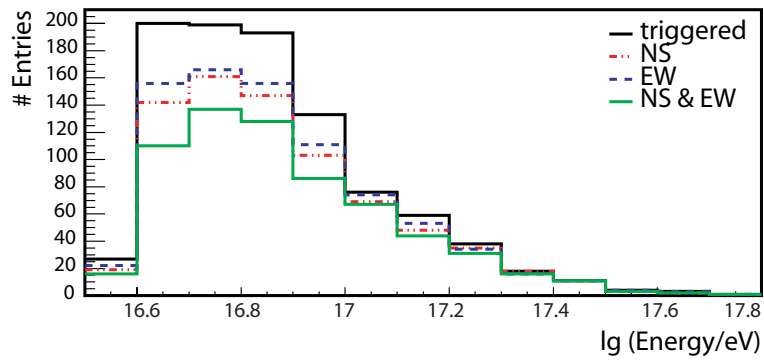
(a) KASCADE selection
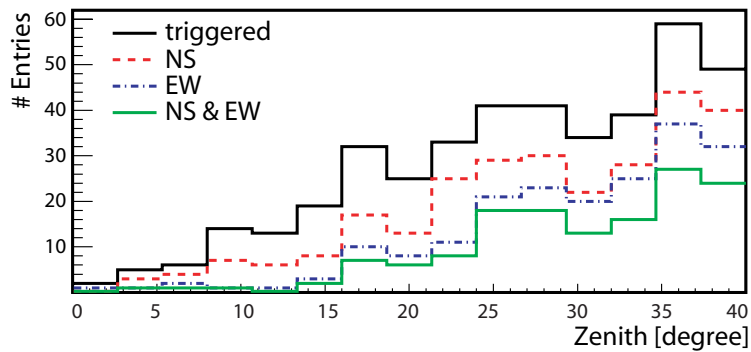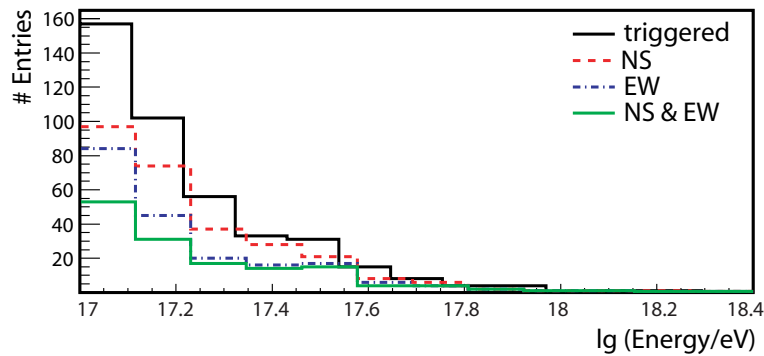
(b) Grande selection

Figure 6.4: Energy and zenith distributions of the KASCADE and Grande event selections; included are all triggered and selected events, the east-west and north-south detected events, as well as events with detection in both EW and NS polarizations (shown by different colour and line style).

pulse in all antennae. Quantification of these parameters, so that the classification can be done automatically, seems not to be easy. One possibility is to classify all selected events by eye as good or bad, but it turned out not to be the most effective way, when the number of events is high. For the analysis in the present work, a cut on the radio observable CC_{beam} > 1 μV/m/MHz, including a required signal-to-noise ratio ($SNR = CC_{beam}/RMS(CC_{beam})$ > 4) of the field strength reconstructed in each polarization direction is applied. Fig. 6.4 shows the energy and azimuthal distributions of the KASCADE and Grande selected air showers. Included are all triggered and selected events, the east-west and the north-south detected events in radio (i.e. CC_{beam} reconstructed in each polarization direction), as well as events with detection in both polarization components. The mean zenith angle from the distributions of the KASCADE selected events is about 21° and for the Grande selected events (which are more than 100 m distance from the LOPES antenna array) is about 27°.

As the KASCADE data-set consists mostly of events with primary energy below 10^{17} eV, the expected signal strength is relatively low, and the SNR has large variations depending on the shower geometry and the core position (close to or far from the LOPES antenna array) of the selected KASCADE or Grande events (see Figs. 4.5, 4.6). Thus, for the present analysis of the radio signal a high primary energy ($E_p > 10^{17}$ eV) is required to avoid any threshold (mainly in radio) effects on lower energies. No cut on other shower observables is considered, except for the fact that both KASCADE and Grande selections are performed for zenith angles below 40 degrees. Within these quality cuts of EAS observables, the air shower reconstruction by the particle detectors is of high accuracy.

Mainly due to the energy cut, from 976 KASCADE triggered and selected events, only 159 events passed all cuts of radio observables (i.e. SNR and CC_{beam}) with good reconstruction in the EW polarization component and 151 with good reconstruction in the NS polarization component (see Figs. 6.4, 6.5) respectively. 124 events are detected in both polarization components. Not all of these final selected events have a coherent signal, though high primary energy ($E_p > 10^{17}$ eV) is considered (see Fig. 6.6). There are missing events because of the cut on the SNR. In the KASCADE selection, the shower cores are too close to the radio antennae, therefore the background noise is high. On the other hand, in the Grande selection (427 events in total) are also missing events (because of the low signal at large distances), even though there is access to higher energy, i.e. above 10^{17} eV. The advantage of the Grande shower selection is that it allows investigation of distant events. Though, with the large distance between the antennae and the shower axis the recorded field strength is lower, therefore the efficiency is lower.

Polarization (the focus of this work) is the key to study the radio emission mechanism in air showers. It contributes to an improved knowledge of the emitted radio signal. It is directly related to the shower geometry, which is described by the azimuth, zenith and geomagnetic angles. For the two event selections we have generated a sky-map implemented on the air shower angles of azimuth and zenith, which allows to examine the direction of the incoming EAS per polarization. Such sky-maps are shown in Figs. 6.7, 6.8, where both event selections are displayed. It proves that in Karlsruhe, the EW-oriented LOPES antennae are sensitive to showers mainly coming from the North direction, i.e. maximum of the field strength is registered for
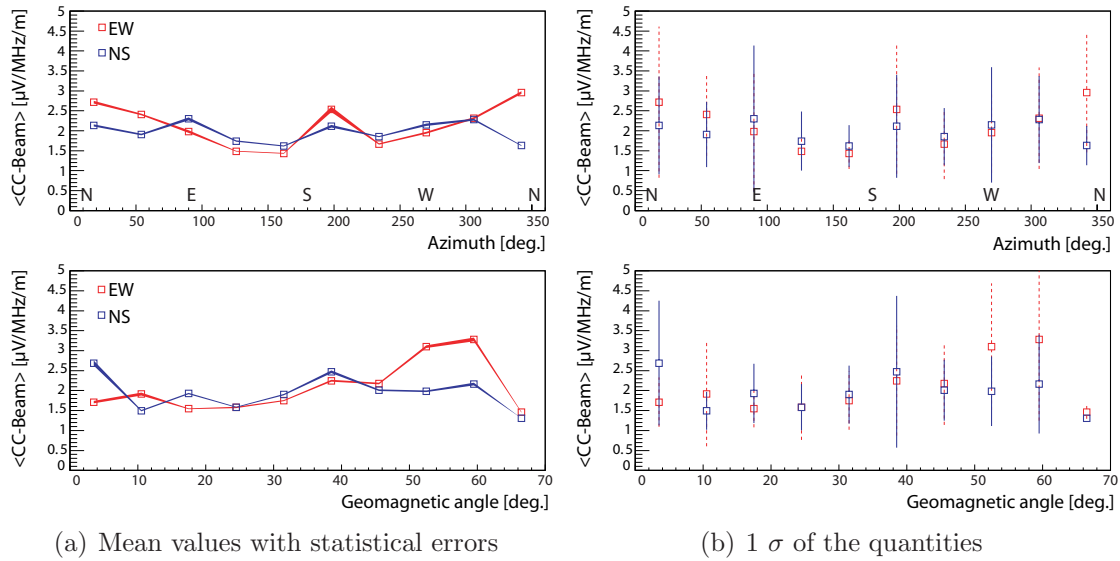
(a) Mean values with statistical errors   (b) 1 σ of the quantities

Figure 6.5: Reconstructed pulse height (uncorrected for e.g., incident direction, distance to shower axis, primary energy), with error on the mean, for KASCADE showers in each polarization (east-west (159 ev.) and north-south (151 ev.)) with SNR above 4, field strength above 1 μV/m/MHz, and primary energy above 10^{17} eV. Same distributions with azimuth and geomagnetic angles are shown in the right panels, but the error bars show the rms (root mean square) of the quantities.)

showers coming from the Northern hemisphere (see color code: red), and less sensitive for showers coming from the South ($270° > \phi > 90°$); the NS-oriented antennas are more sensitive to incoming air showers from the West and East hemispheres. The dependencies of the polarized field strength (CC_{beam} reconstructed in each polarization component) with azimuth and geomagnetic angles of the air shower are displayed in Fig. 6.5, which reflect the same feature characteristics. The amplitude of the signal is higher for large geomagnetic angles, what obviously is directly related to the azimuth angle for the given range of zenith angle ($\theta = 0°$ - $40°$), as given by the KASCADE array, for which the air shower reconstruction accuracy is pretty high. Systematic differences between the two polarization components are observed. For the EW polarization component a field strength increase is seen in the North direction, as well as in the South, but with a larger rms because of less statistics (see the azimuthal dependences). The same is true for the geomagnetic angle; a field strength increase is observed with higher geomagnetic angles (i.e. above 30 degrees) for the EW polarization component, but a slightly different distribution for the NS polarization component is found. These characteristics seen in the measured data are in agreement with the analytical calculations and support the geomagnetic effect in the radio emission mechanism.

6.3.1 Study of the CC_{beam}^{ratio}

In considering polarization aspects of the measured radio signal we analyze the CC_{beam}^{ratio} (i.e. $CC_{beam}^{NS}/CC_{beam}^{EW}$, the ratio between the relative pulse height reconstructed in the NS polarization direction versus the pulse height reconstructed in the EW direction). The ratio is adopted to be independent of the total field strength and primary energy or mass, when looking for its dependencies with the EAS geometry. From detailed examinations of the pulse height ratio, it is found that dependencies
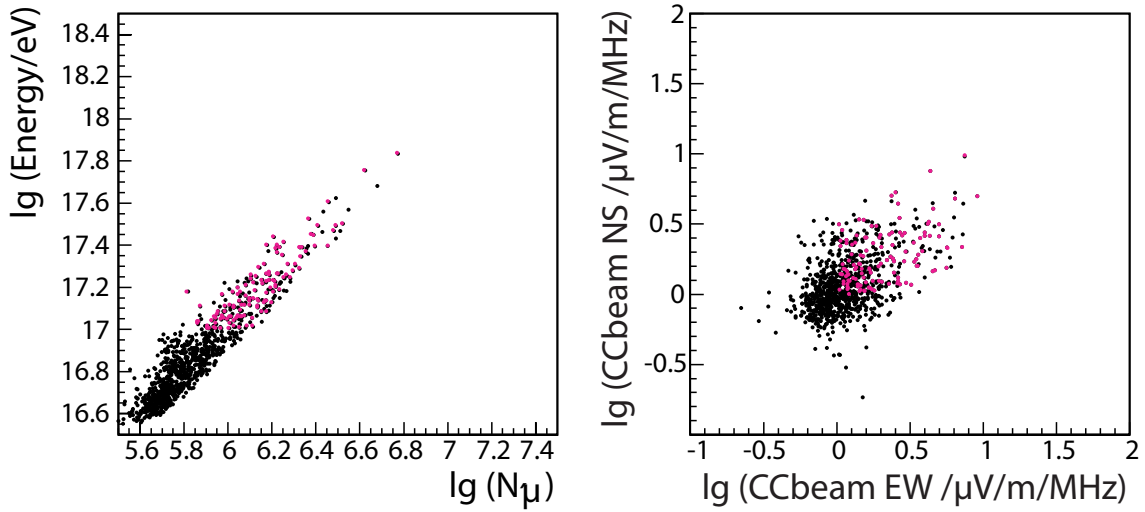
(a) The KASCADE data-set
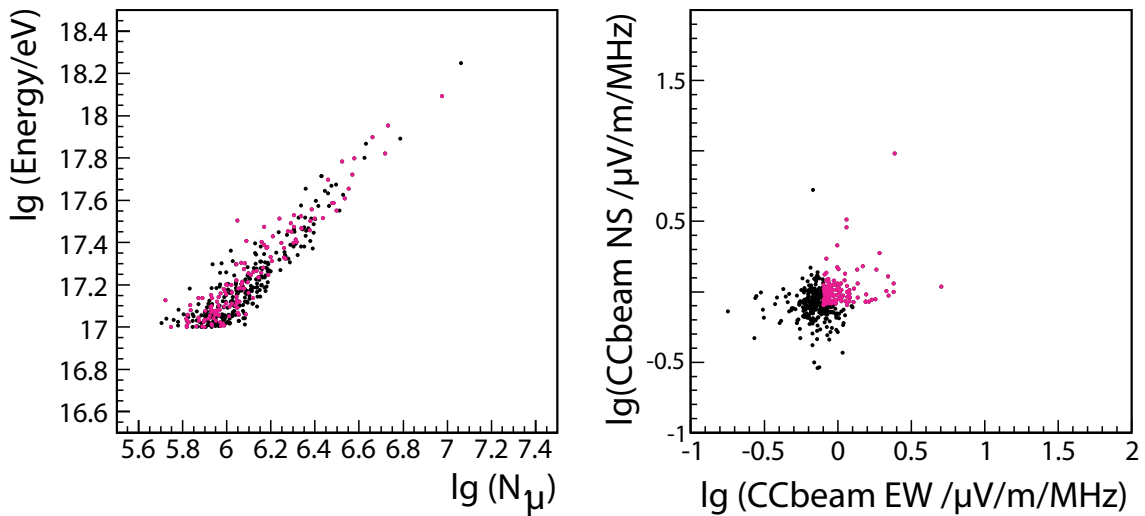
(b) The Grande data-set

Figure 6.6: Scatter plots of primary energy versus total muon number (left panels). Scatter plots of the reconstructed radio pulse height in the EW polarization direction versus NS, respectively (right panels). Black points represent the events with pulse height above zero (956 events for (a) and 406 events for (b)). Pink points represent the events with $CC_{beam} > 1$ μV/m/MHz, SNR > 4 and $E_p > 10^{17}$ eV (resulting in 124 events with detection in both polarization (a) and 141 for (b) respectively).
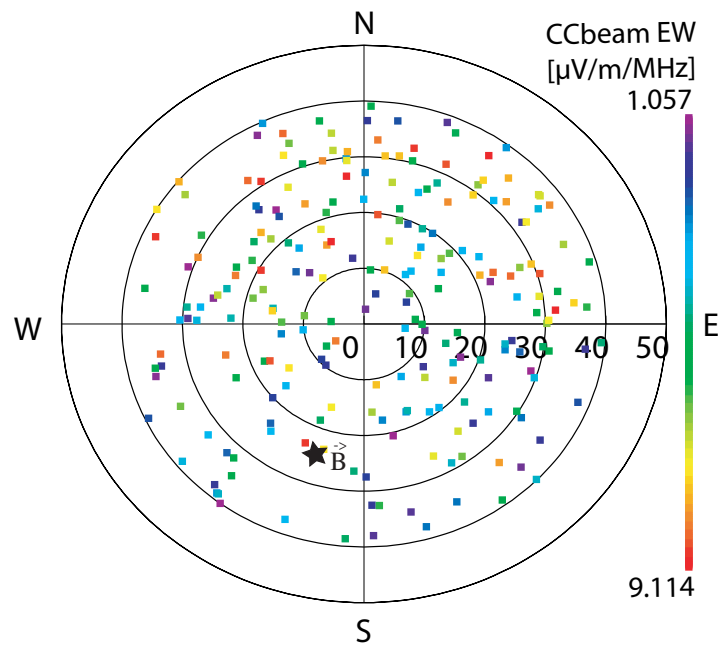
(a) Events with signal response in the EW polarization direction
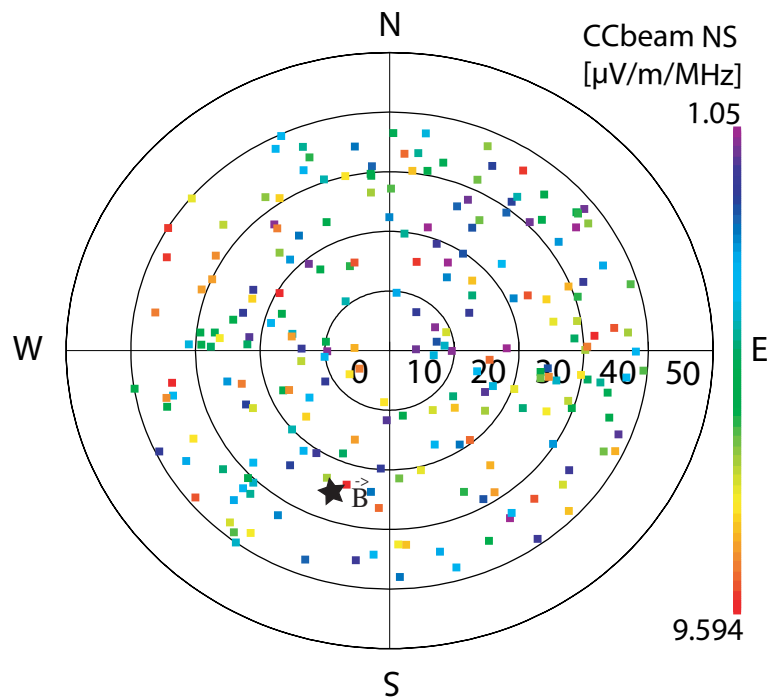
(b) Events with signal response in the NS polarization direction

Figure 6.7: Sky-map, as azimuth relative to zenith, of EW (top) and NS (bottom) detection of KASCADE showers. The color code represents the reconstructed pulse height in each polarization, with values larger than 1 μV/m/MHz; the red color represents the largest value of the CC_{Beam}.
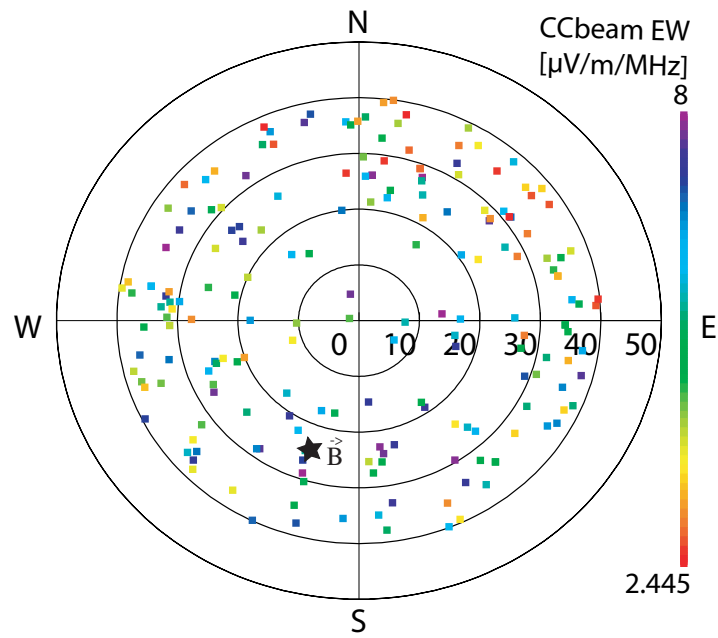
(a) Events with signal response in the EW polarization direction
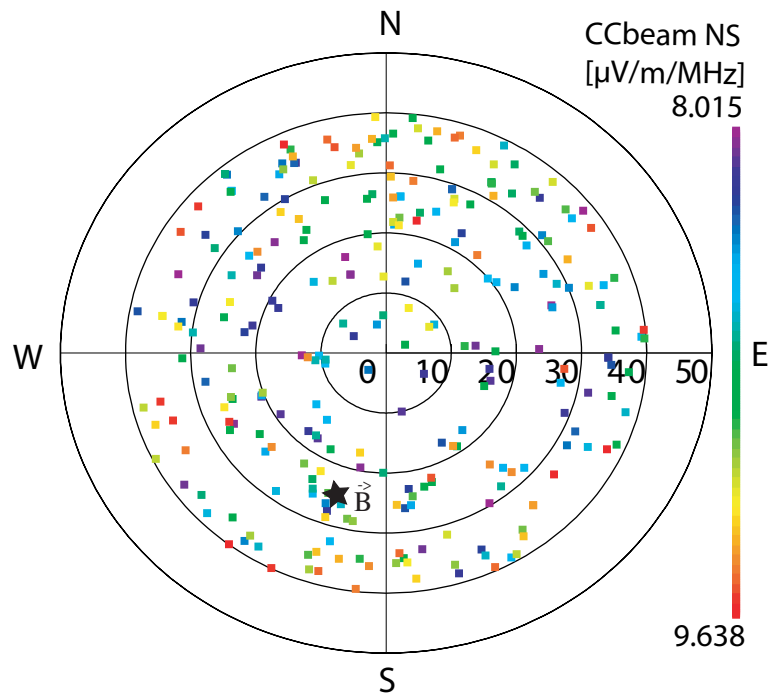
(b) Events with signal response in the NS polarization direction

Figure 6.8: Sky-map of azimuth relative to zenith of EW (top) and NS (bottom) detection of Grande showers. The color code represents the reconstructed pulse height (CC_{beam}) in each polarization (i.e., CC_{beam}^{NS} and CC_{beam}^{EW}), with values larger than 1 μV/m/MHz; the red color represents the largest value of the CC_{beam}.

on azimuth and geomagnetic angle are of main relevance. There seems to be a characteristic dependency between the CC_{beam}^{ratio} and the shower geometry (see Fig. 6.9), which we will try to explain it with the simplified geomagnetic model. In these investigations included are only showers which are detected in both polarization directions (in difference to Fig. 6.5).

The CC_{beam}^{ratio} values of measured data show characteristic dependencies with geomagnetic and azimuth angle, not in agreement with a uniform distribution (bottom panels, open circles). The large scatter of measured values of CC_{beam}^{ratio} in dependency with azimuth angle reflect the systematic uncertainty in the measurements. But, the width of the distributions also express the different zenith angles (from 0° to 40°) for the ratios in dependency with the geomagnetic angle.

For the CC_{beam}^{ratio} assumption, 99 events with detection in both polarization directions are used. They are also simulated with the REAS3 code based on their corresponding air shower parameters (e.g. $\alpha, \theta, N_\mu, N_e, E_p$). Comparison between their simulation results with the measured data will be discussed in Sec. 6.5 with respect to the lateral distribution per individual event and per individual polarization, as the CC_{beam} calculation of the simulated events is not possible yet (e.g. due to non-properly treated noise behaviour in the beam-forming process). All 99 events have a good radio detection in both (EW and NS) polarization directions and allow proper physical investigations for primary energies above 10^{17} eV.

The observed characteristic features in the CC_{beam}^{ratio} distribution of the measured events can be explained by the assumed simplified geomagnetic model (see Fig. 6.9), based on a pure shower geometry via the Lorentz force approximation (see Sec. 5.1). The simplified $P_v = \vec{v} \times \vec{B}$ model is incorporating the shower direction $\vec{v}$ and the geomagnetic field $\vec{B}$ (see Appendix). The polarization vector is projected to each polarization component (i.e. the east-west (P_v^{EW}) and north-south (P_v^{NS}). The ratio of the values ($P_v^{ratio} = P_v^{NS}/P_v^{EW}$) shows that: for $P_v^{ratio} > 1$, dominant detection is expected for the P_v^{NS} projection, and for ratio $P_v^{ratio} < 1$, dominant detection is expected for the P_v^{EW} projection (see Fig. 5.3). The visible positive maxima corresponding to the zenith angles of 30, 40 and 60 degrees occur because of the incoming direction of the radio wave relative to the Earth magnetic field (i.e. radio wave parallel to the Earth magnetic field). The larger the geomagnetic angle, for a given zenith angle, the larger the P_v -amplitude.

In Chapter 5, by using a sample of simulated events, we have seen that the $\vec{v} \times \vec{B}$ model does not describe the full radio emission, especially for the NS polarization component. To check whether the $\vec{v} \times \vec{B}$ expected relations, or their same deviations, are also seen in the measured data, we calculate the P_v^{ratio} in terms of the P_v-amplitude for each individual measured event (Fig. 6.9, bottom panels, full circles). Thus, we apply the simplified model to the measured shower geometry of the 99 KASCADE events which has signal detected in both polarization components of $E_p > 10^{17}$ eV. The characteristic dependencies of P_v^{ratio} with azimuth as well as with the geomagnetic angle are obvious. Same figure (bottom panels, open circles) shows the distribution of the measured events in their CC_{beam}^{ratio}. Comparable qualitative behaviours are observed in their main characteristics, despite of the fact that the widths of the distributions per bin (error bars) are large in the experiment, as well as they include the dependencies of the amplitude (per polarization) on zenith angle, primary energy and distance, which is not the case for the P_v^{ratio}. In addition,
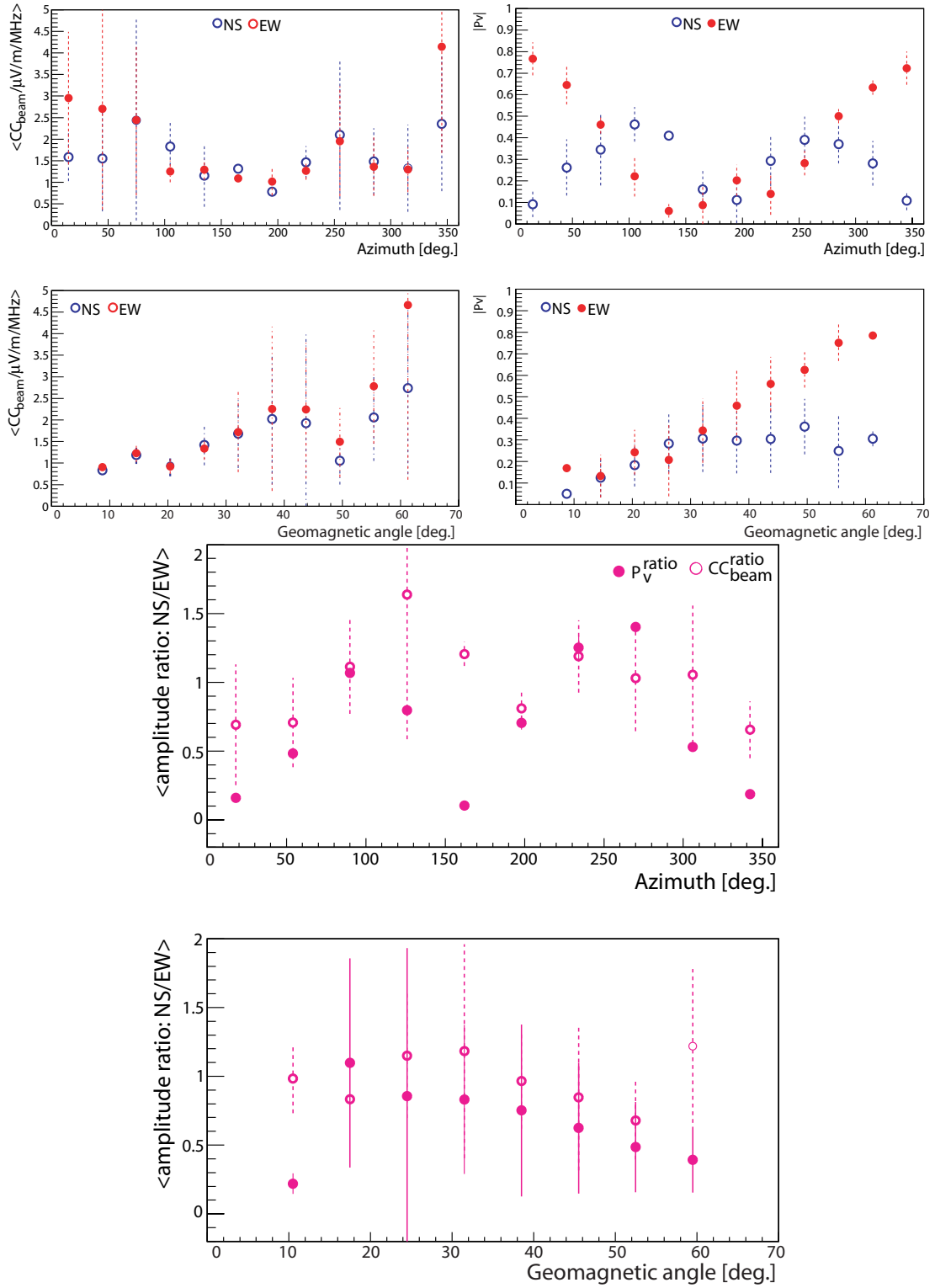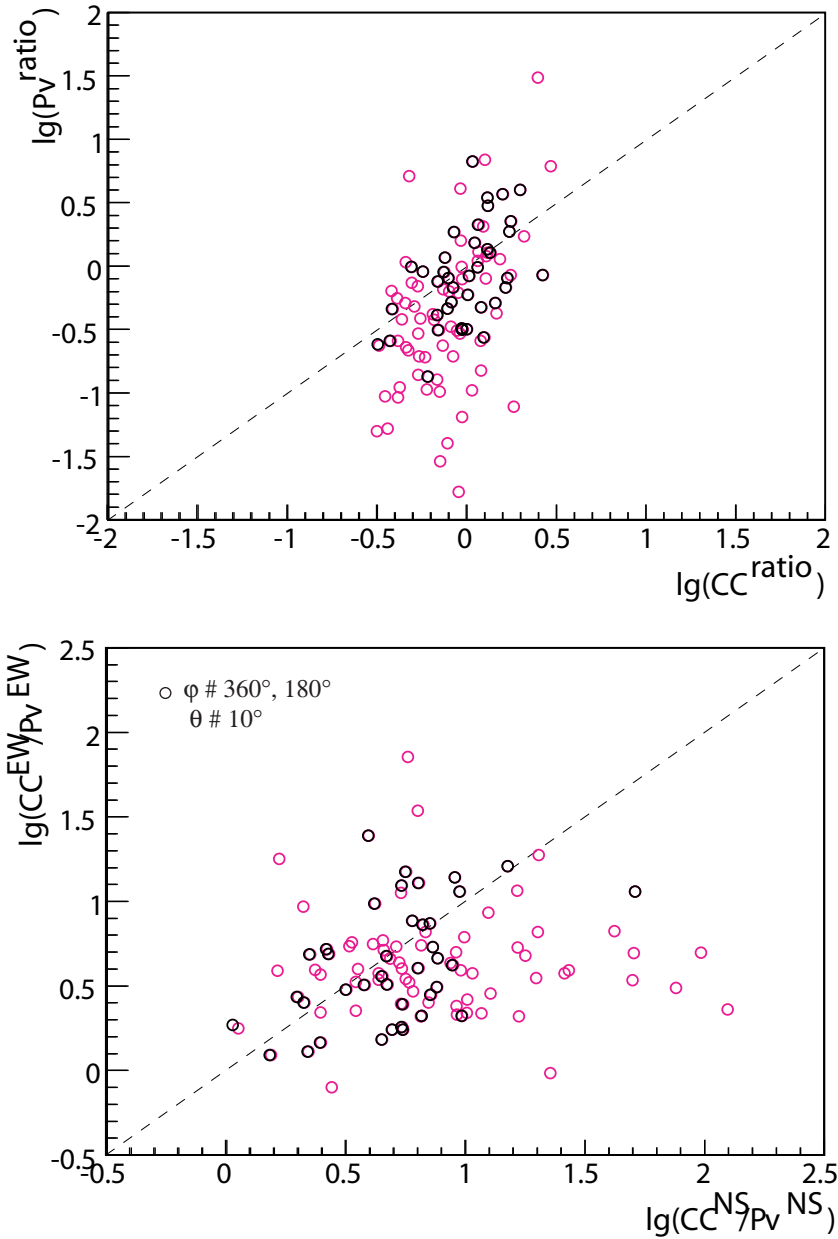
Figure 6.9: Correlation of the measured data and analytical (in terms of $P_v = \vec{v} \times \vec{B}$) amplitude with azimuth and geomagnetic angles. The error bars show the rms (root mean square) of the distribution inside the bin. Binned data of 99 KASCADE showers are displayed.

Figure 6.10: Top panel: Scatter plot between the ratio of $\vec{v} \times \vec{B}$ -amplitude and of measured amplitude (ratio=NS/EW polarization directions). Bottom panel: Ratio between the reconstructed measured radio signal (in the EW polarization) and $\vec{v} \times \vec{B}$ -amplitude (projected to the EW polarization direction): Y-axis. Same but for the NS polarization direction: X-axis. Each circle represent a shower. The pink ones are the showers from the North and South directions, or with $\theta < 10°$. It is obvious that black points fit better to P_v. Showers from North and South, predictions of NS-oriented antennae, are not in agreement with the P_p -model, i.e. considering pure geomagnetic origin of the signal.
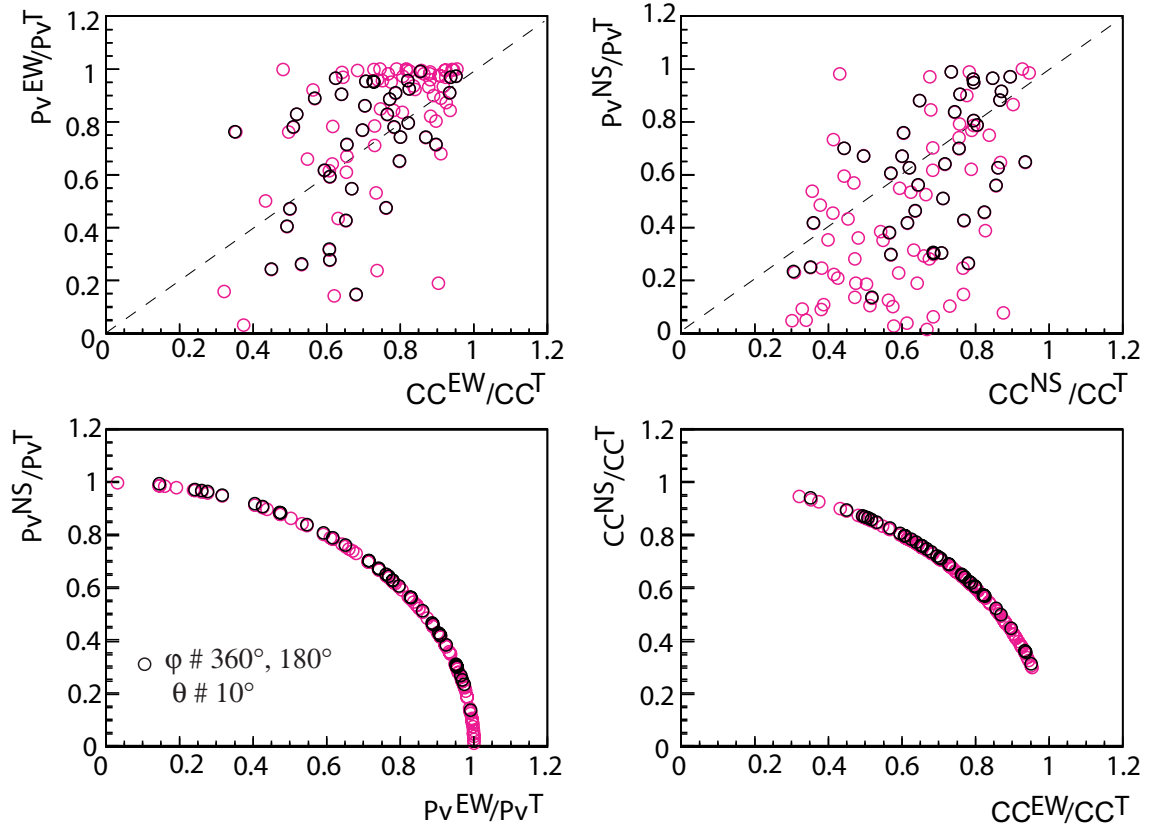
Figure 6.11: From left to right: scatter plot between $\vec{v} \times \vec{B}$ -amplitude in the EW polarization direction divided by the total amplitude and the measured reconstructed radio signal in the EW polarization direction divided by the total amplitude. Same for NS polarization direction, for which it is observed that for incoming showers from Northern and Southern hemispheres, as well as for vertical showers ($\theta = 0°$), the polarization vector given by the $\vec{v} \times \vec{B}$ -amplitude projected to the North direction is zero, while the simulated corresponding amplitude is not.

concerning the CC_{beam} values of the measurement, the EW-oriented antennae could catch some fraction from the NS and vertical components of the signal, and otherwise for the NS-oriented antennae. Thus, some small uncertainty from these aspects of the measurement has to be aware of.

Concluding the dependencies of the CC_{beam} values, reconstructed for each polarization direction of the electric field (EW and NS), the field strength in the different polarization direction has a different dependence on the geomagnetic field direction: the signal is linearly polarized mainly in the direction perpendicular to the air shower and magnetic field axis (at least at central regions of high emission), in good agreement with the analytical calculations (see Fig. 6.9, top panels, i.e. the comparison between measured data and application of the P_v to measured shower geometry using its separate projection for EW and NS polarization components). In particular, from the CC_{beam}^{ratio} which is independent of EAS observables, we compare the polarization characteristics relative to the shower geometry, e.g. azimuth and geomagnetic angles. They agree well with the responses of the simplified geomagnetic $\vec{v} \times \vec{B}$ model. From the scatter plot of P_v^{ratio} versus the CC_{beam}^{ratio} (e.g. Fig. 6.10, top panel) one can see that there is a good agreement for showers coming from East and West (black circles). But, there is a deviation for showers coming from North and South directions (and for more vertical showers with $\theta < 10°$). In the bottom panel of Fig. 6.10 is observed that the deviation in the ratio is mainly due to a disagreement in the NS polarization component. Looking now to the individual polarization contributions relative to the total amplitude (Fig. 6.11, where $CC^T = \sqrt{CC_{EW}^2 + CC_{NS}^2}$, $P_v^T = \sqrt{P_{EW}^2 + P_{NS}^2}$), one can see that showers coming from the North and South directions are not in agreement with the P_v expectations. It means, we see in data a contribution to the signal not stemming from geomagnetic origin, as in the P_v expectations only this source of emission is considered.

The Grande shower selection is not used for this investigation as only few events have reliable good reconstruction of the radio signal. This is reasoned by the large mean distance to the shower axis, though they allow access to high primary energy (i.e. $> 10^{17}$ eV).

With the results obtained so far, the prediction of polarization characteristics of the emission generated in the geomagnetic emission scenario is directly tested. However, major part of the radio emission process seems to underline the geomagnetic effect. The understanding of these polarization dependencies are mandatory for the interpretation of the experimental measurements.

6.4 Radio pulse parametrization

Already, from the previous studies of measurements with all 30 LOPES antennae sensitive in the east-west polarization direction only [39], the dependencies of the CC_{beam} were established on the following shower observables: the angle of incidence (i.e. the geomagnetic angle α), the distance to the shower axis D, and the primary energy E_p. These well-reconstructed shower parameters by the particle detector array KASCADE-Grande are considered in the parametrization of the radio signal (see equation 4.1, Sec. 4.5). They are obtained by applying different fit functions in three iterative steps. A linear fit to the angle of incidence, an exponential decay fit to distance, and a power low fit to the energy were established. In each fit the other

dependencies are cancelled by the division of the fit result from the previous iteration step. The fit functions are chosen in order to have one parameter as common factor for all events, and thus they can be used to account for an unknown systematic offset from the uncertain antenna calibration at that time.

Compared to the old considerations [39], in the present analysis of dual-polarization measurements, first the LOPES system is well calibrated and in addition the simplified geomagnetic model $\vec{v} \times \vec{B}$ is used in the parametrization of the radio signal for the shower direction (in which the azimuth, zenith and the geomagnetic angles of the shower are accounted for), instead of a $1 - cos(\alpha)$ dependence as was previously considered for the east-west polarization measurements. The distributions of the EAS observables, e.g. azimuth angle, zenith and geomagnetic angle, as well as the P_v value for the events included in the present studies (KASCADE sample) are displayed in Fig. 6.12, where the EW (dotted line) and NS (continuous line) polarization components are shown. The geomagnetic angle has values in the range of 0-60 degrees, because of the restricted zenith angles in the range of 0-40 degrees. A different azimuthal distribution per polarization can also be observed, i.e. an increase around the North and a decrease in the South for the EW polarization component, and vice-versa for the NS polarization component. The magnetic field has an important influence on the polarization characteristics of the radio emission. The EW projection of the polarization vector P_v is favored because of the 0.5 Gauss $\smile$ 70° inclined magnetic field present in Europe (whereas a 0.3 Gauss horizontal magnetic field is present in the equatorial region). The effect is visible in the P_v distribution per polarization, i.e. the maximum of the EW projection can reach values close to 1, whereas the maximum for the NS projection is already reduced to 0.6.

The individual projection of the polarization vector on each polarization direction is now taken into account for the parametrization of the radio signal. With the CC_{beam} reconstructed independently for each individual polarization direction, the following function is considered for the east-west and north-south direction respectively in the parametrization of the signal: $f(P_v^{EW}, D, E_p)$ and $f(P_v^{NS}, D, E_p)$ respectively. The parametrization function incorporates the three main shower dependencies, in respect to the direction (P_v), distance (D), and energy of the primary particle (E_p). For the three-step parametrization procedure see Appendix A. The pulse height (CC_{beam}) can be parametrized with the measured shower geometry provided by the KASCADE-Grande experiment. The KASCADE event selection is favoured, because it allows the well-reconstructed shower parameters of cores fallen inside the LOPES antenna array, for which a low mean distance to the shower axis is available, and therefore a coherent radio signal can be reconstructed.

In Fig. 6.13 the result after the third final iteration of the parametrization is shown. Each polarization is treated separately. First, the CC_{beam} is normalized with the distance to shower axis (D) and the primary energy (E_p), and applying a linear function to the P_v signal dependence gives a index of $\smile$ 0.7 (top panel). Second, the CC_{beam} is normalized with P_v and the primary energy (E_p), and fitted with an exponential function resulting in a scale parameter of $\smile$ 200 m (middle panel). Third, the CC_{beam} is parametrized with P_v and distance to shower axis (D), and fitted with a power law function where a slope of $\smile$ 0.9 is obtained. The associated fit parameters per polarization are listed in Table 6.1, including their uncertainties. Not all the events are included in the power law fit, because of the energy threshold of $E_p >$
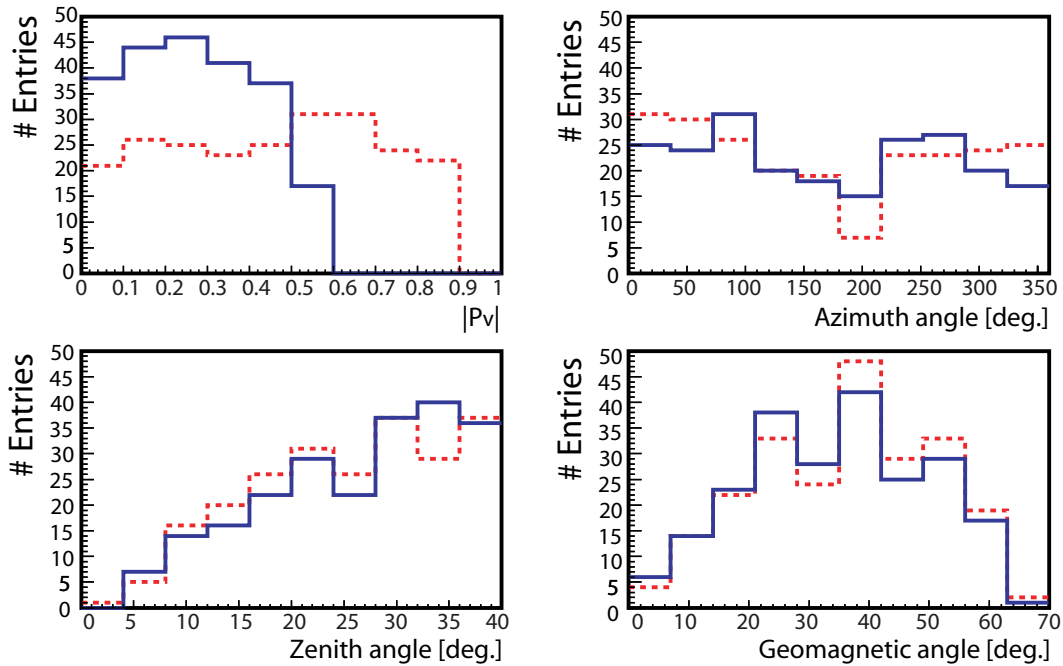
Figure 6.12: Distributions of the EAS observables (azimuth, zenith and geomagnetic angles; 228 events in the EW polarization direction and 223 in the NS) used in the calculation of the unit cross product vector: $\vec{v} \times \vec{B}$ for both polarization components of the electric field (east-west: dotted line, and north-south: continuous line) are displayed.

10^{17} eV, which is related to the efficiency problem of the LOPES antennae located too close to the KASCADE particle detectors (i.e. close to the shower core the noise level is high, because of the possible activation of some nearby electronics). The error bars for the single events include 20% systematic uncertainty of the amplitude calibration as well as the 20% systematic uncertainty of the primary energy estimation by the KASCADE experiment. With the help of these found dependencies, which are very similar for both polarization components, the radio pulse height can be estimated for each EW and NS polarization directions, for given shower parameters. Combining the parametrizations (results compiled in Table 6.1), for the radio pulse height a formula (which incorporates the shower dependencies) is established per individual polarization, as follows:

$$\varepsilon_{EW} = 1.17 \cdot (|P_v^{EW}| + 0.67) \cdot \exp(\frac{-D}{209.7m}) \cdot (\frac{E_p}{10^{17}eV})^{0.90} [\frac{\mu V}{mMHz}] \qquad (6.1)$$

$$\varepsilon_{NS} = 1.89 \cdot (|P_v^{NS}| + 0.55) \cdot \exp(\frac{-D}{156.4m}) \cdot (\frac{E_p}{10^{17}eV})^{0.95} [\frac{\mu V}{mMHz}] \qquad (6.2)$$

where P_v, D, E_p are the free variables which represent the air shower properties, given by the KASCADE experiment. The only difference in the estimation of the two equations concerns the polarization aspects. For the pulse height estimation in the EW polarization direction, the measured field strength reconstructed in this direction, and respectively the P_v^{EW} projection, including the shower parameters, are applied. The same procedure is applied for the pulse height estimation in the NS polarization direction: the measured pulse height is reconstructed in the NS
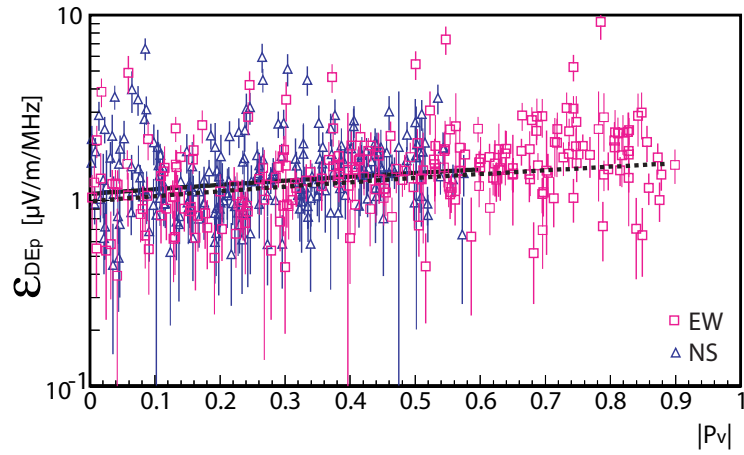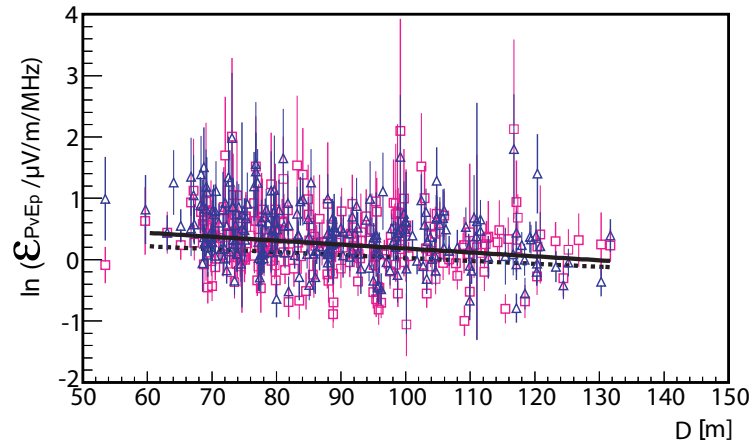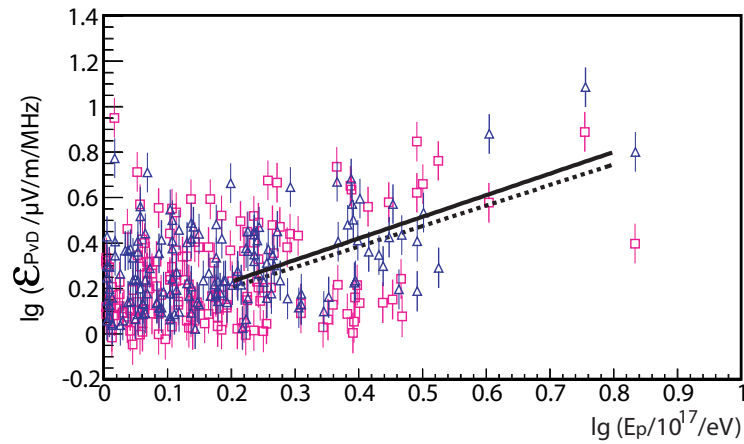
(a) Parametrized CC_{beam} with E_p, D vs. P_v vector model

(b) Parametrized CC_{beam} with P_v, E_p vs. D distance

(c) Parametrized CC_{beam} with P_v, D vs. E_p energy

Figure 6.13: Parametrized CC_{beam} in the east-west (dotted line) and north-south (continuous line) polarization directions in correlation with $P_v = |\vec{v} \times \vec{B}|, D, E_p$. P_v is the vector model, D the distance to shower axis, and E_p the primary energy. The KASCADE shower observables are used here. See Appendix for the parametrization procedure. The error bars for the single events include systematic uncertainties of the calibration procedure.

(a) KASCADE events   (b) Grande events
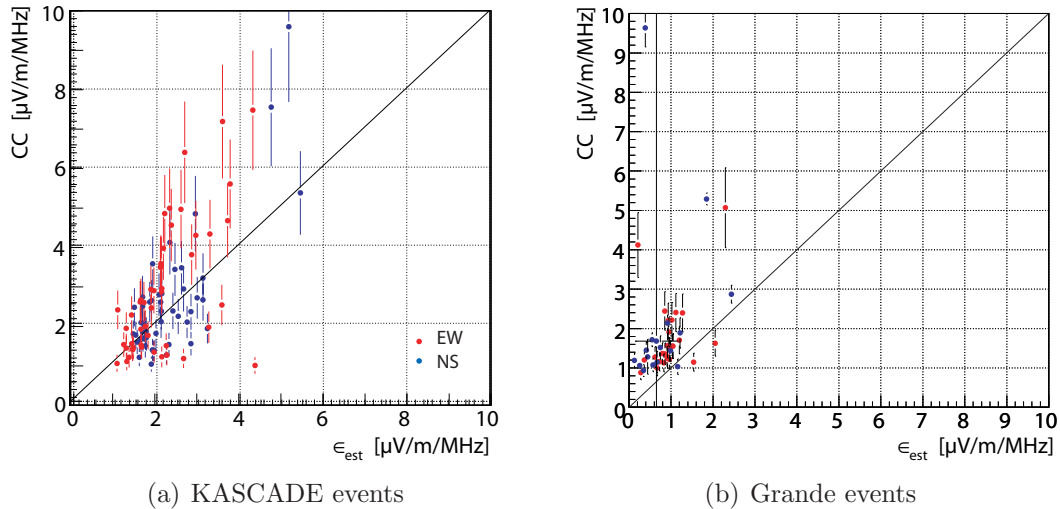
Figure 6.14: Estimated signal amplitude per polarization using the KASCADE shower selection. Radio signal reconstructed in EW and NS polarization directions together with shower parameters, like primary energy, distance to showers axis and $\vec{v} \times \vec{B}$ -polarization vector projected to each EW and NS polarization components are used for primary energy $> 10^{17.2}$ eV (49 KASCADE events per polarization component, while for Grande: 26 events are in EW and 17 in NS). Statistical errors are seen per event.

Table 6.1

Summary of the fit results			
Info (3-steps)	$(Fit\ func.)$	$(Fit\ res.)_{EW}$: a/b	$(Fit\ res.)_{NS}$: a/b
ϵ_{D,E_p}	$a1 \cdot |\vec{v} \times \vec{B}|$	$0.67\pm0.09/0.99\pm0.04$	$0.65\pm0.14/1.08\pm0.04$
ϵ_{P_v,E_p}	$a2 \cdot e^{\frac{-R}{b2}}$	$1.66\pm1.14/209.7\pm61.5$	$2.27\pm1.12/156.4\pm30.5$
$\epsilon_{P_v,D}$	$a3 \cdot E_p^{b3}$	$1.05\pm1.08/0.90\pm0.1$	$1.09\pm1.08/0.95\pm0.1$

polarization direction, and the polarization vector is projected into the NS direction P_v^{NS} respectively, including the shower parameters.

By assuming a pure geomagnetic emission the $\vec{v} \times \vec{B}$ -model should contain both aspects: shower geometry and polarization. The important characteristics of the radio emission (e.g. the dependence on the primary particle energy, the dependence on the mean distance to shower axis (in this case, mean distance from LOPES antennae), the dependencies of the P_v vector) are all counted in the radio pulse estimation per individual polarization, i.e. the formulas 6.1, 6.2 which deliver the calibration of the radio emission. Considering the different polarizations (given by the theory of geomagnetic origin of the radio emission) the two calibration formulas agrees to each other within their uncertainties. This agreement is a clear hint, that the geomagnetic emission is the dominant factor for generating the radio signal.

But, even when P_v is zero we have measured a signal, which is not expected by the P_v -model. Therefore, it appears a discrepancy between the prediction and what we actually see in the measured data. The slope of the fit applied to the $P_v^{EW,NS}$ for each polarization direction is nearly 0.6, for which the theory predicts it to be zero. In addition, even after the parametrization, the scatter of the events is still
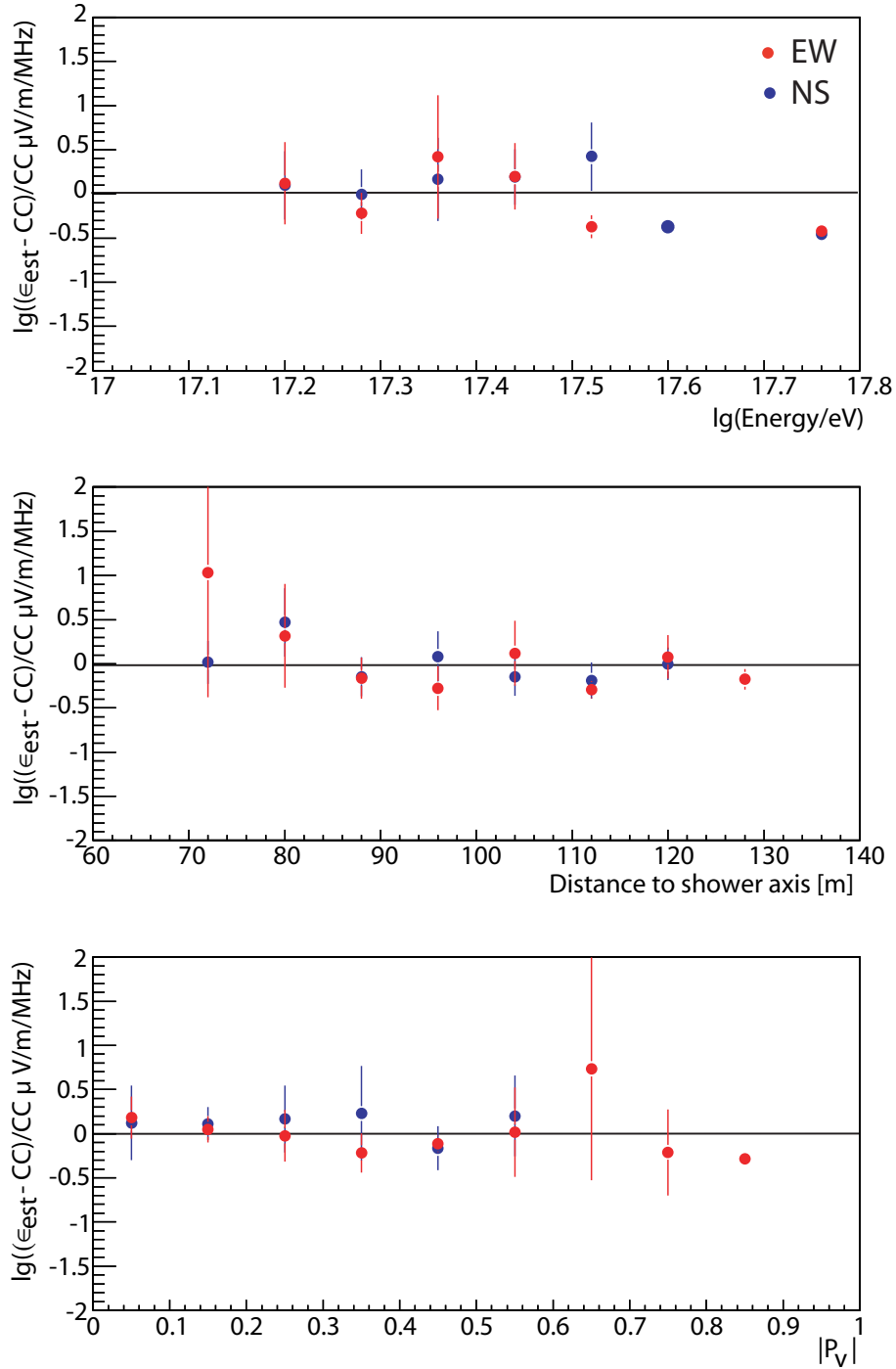
Figure 6.15: Profiles of the relative contribution of the estimated radio signal relative to the measured field strength using the KASCADE events. No contribution is seen in correlation with main showers dependences used in the parametrization, e.g. primary energy, distance to shower axis and $\vec{v} \times \vec{B}$ -polarization vector projected to each EW and NS component of $E_p > 10^{17.2}$ eV. The error bars show the widths of the distributions.
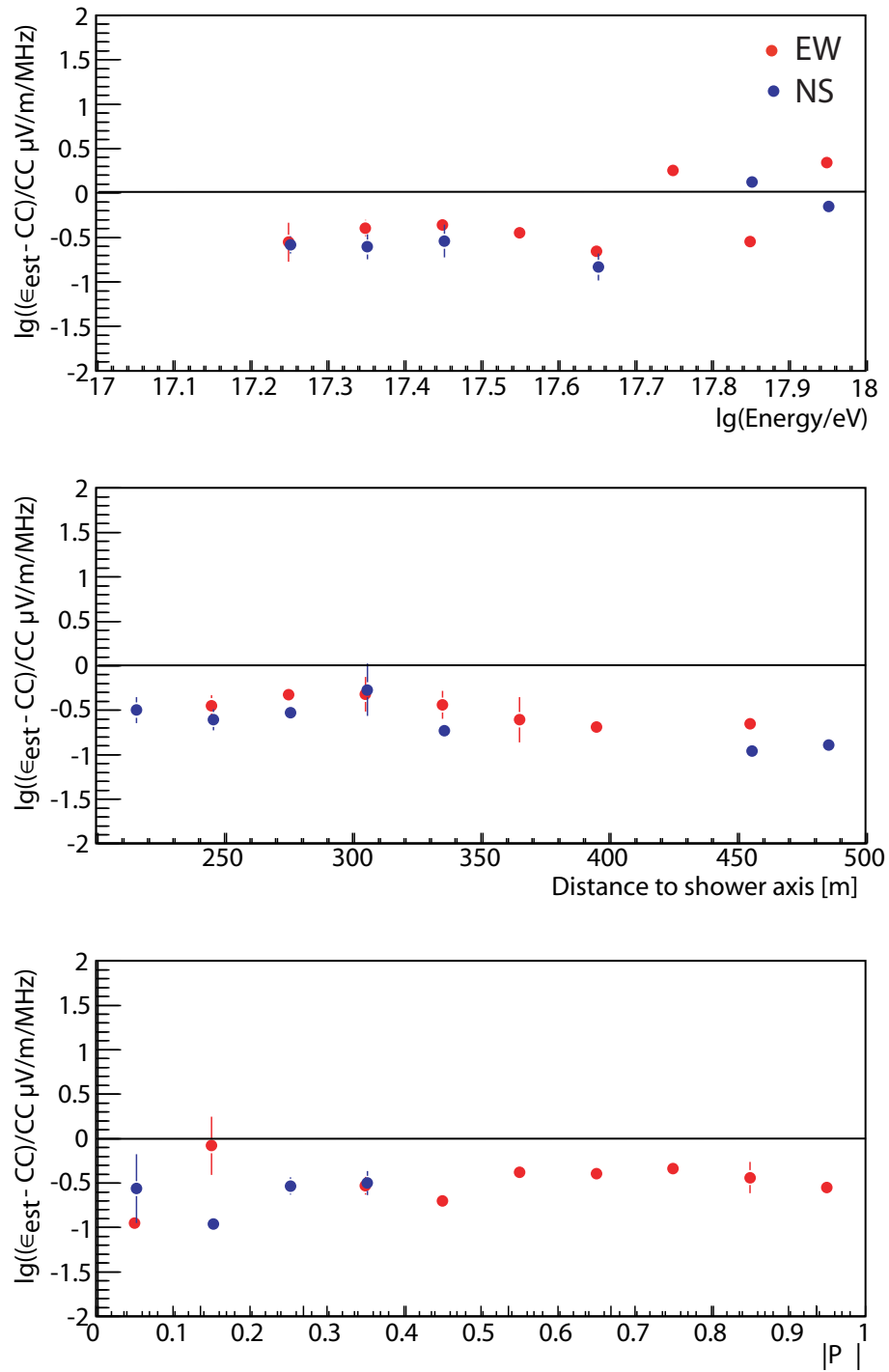
Figure 6.16: Same as Fig. 6.15, but for Grande events (26 in EW and 17 in NS)
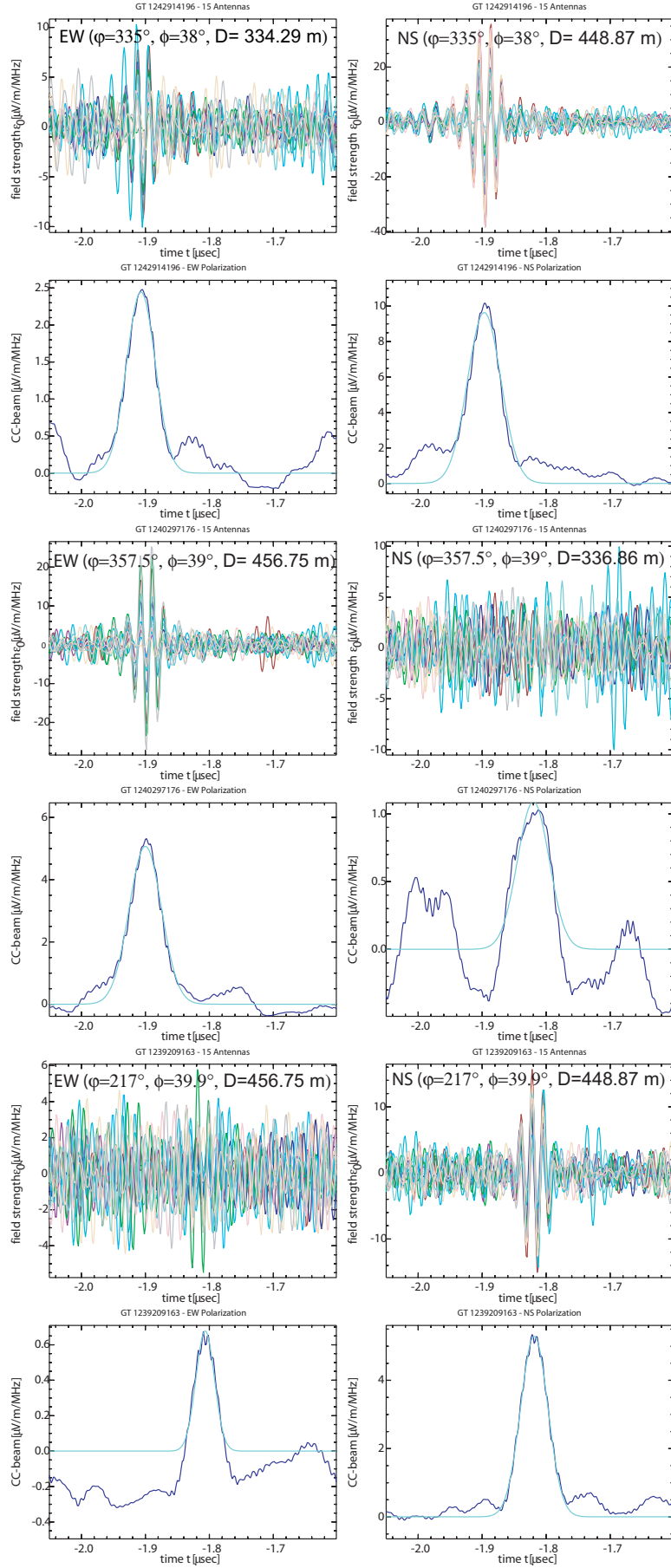
Figure 6.17: Field strength and CC_{beam} of three 'Grande' events with $E_p > 10^{17.7}$ eV.

large (see Fig. 6.13). This either is related to the relatively low statistics in our data of high energetic events $> 10^{17}$ eV (i.e. we are affected by threshold and efficiency effects, despite the absolute amplitude and timing calibration of our antennae. Or, the P_v model does not fully describe the emission mechanism. Another hint to this, is that the scale parameter of the lateral distribution is slightly different. This will be studied in more detail in the next Section.

The radial distance in both polarization cases is given by an exponential decay, and the resulting scale parameters in our parametrization corresponds to ~ 209 m for the EW polarization and to ~ 156 m for the NS polarization respectively. In the previous work of parametrizing the radio signal on a single (EW) polarization direction only, using LOPES-30 data, the scale parameter was found to be in the order of 236 m, and a power law index of the primary energy dependence of about 0.95 (see [39]). The scaling of the CC_{beam} with the primary particle energy is approximately linear, following a power low $\propto E_p^{0.90}$ for the EW polarization component and $\propto E_p^{0.95}$ for the NS polarization component respectively. An approximately linear scaling of the emission with energy of the primary particle is expected for coherent emission [15]. In the coherent regime, the field strength directly scales with the number of emitting particles. The dependence on shower zenith angle is more complexly treated now within the P_v model, than a simple $(1 - cos(\alpha)) \cdot cos(\theta)$ approach by [39], or the $sin(\alpha) \cdot cos(\theta)$ approach by [8]. Thus the obtained formulas per polarization are difficult to be compared directly with the previous results. In addition, uncertainties regarding the absolute amplitude calibration of the historical data remain.

Having analysed the qualitative dependence of the radio signal on EAS observables, the derived equation for the estimated radio signal of KASCADE showers ($E_p > 10^{17}$ eV) can be applied to any other shower data-set, if the shower geometry is known. In Fig. 6.14 the comparison between the measured radio signal in its CC_{beam} reconstructed value and the estimation of same events is shown (left panel). For the KASCADE selection it is seen that the parametrization was dominated by the smaller CC_{beam} -amplitudes. But for higher values, the parametrization seems not to be describing very well the measurements. The relative difference between the estimated pulse height and the measured-reconstructed values are displayed in Fig. 6.15 for each single shower dependency used in the parametrization (e.g. E_p, D, P_v). No significant differences are found, as the data are in agreement with the zero line for both polarization components.

The Grande event selection allows access to large mean distances to the shower axis, and thus the ability of the radio technique in recording distant events is tested, i.e. > 100 m mean distance from the center of the shower core to the LOPES antenna array. Therefore, the efficiency energy of Grande detectors is higher compared with the efficiency energy of KASCADE showers limited to 10^{17} eV, the good radio detection rate is decreased for Grande showers because of the bad signal-to-noise ratio with the increased distance from the shower core to the observer. The radio signal is mainly incorporated in the noise, and thus a signal can be hardly distinguished as radio detected (e.g. by using a signal-to-noise ratio) if the primary energy is not sufficiently high. However, at Fig. 6.17 three event examples are shown with their field strength and quantified CC_{beam} shown per polarization (EW and NS components). First event (two upper panels) shows detections in both polarization components. Second event (two middle panels) shows detection only in the EW

polarization component. Third event (two bottom panels) shows detection only in the NS polarization component. Considering the arrival direction, this behaviour is in agreement with the $\vec{v} \times \vec{B}$ expectation (see Fig 5.3). The incoming showers are from the North-West, North and South directions respectively, of zenith angles ~ 40 degrees and of $E_p > 10^{17.7} \ eV$. They are the best candidates in radio detected Grande events, which clearly show coherent radio signal in a single or in both polarization components (depending on the shower direction) with a corresponding high CC_{beam} value. Such good radio (distant) detected events in Grande are not sufficient in statistics for a pulse height parametrization, as it is performed by using the KASCADE showers. Thus, the Grande events of primary energies above $10^{17.2}$ eV and high $SNR > 6$ are used to test the pulse height estimation from the KASCADE showers (see Figs. 6.14, 6.16). A systematic underestimation of the field strength (CC_{beam}) using formulas 6.1, 6.2 is seen for the Grande events. The reasons for this can be due to a different experimental behaviour of the lateral distribution function for large distances, or the resolution of the parametrization is not properly enough. Nevertheless, the statistics for Grande events are too low for a deeper investigation.

6.5   Lateral distribution

For this issue we examine the lateral distribution of the signal, recorded in each (EW and NS) polarization directions. Due to a precise amplitude and phase-delay calibration of each LOPES antenna, and because of the good-reconstruction information about EAS obtained from the particle detector array KASCADE-Grande, we can study in detail with high accuracy the field strength seen in each individual antenna as function of distance to the shower axis on an event-by-event basis. The lateral distribution can be described by the decay of an exponential function, i.e. $\epsilon = \epsilon_0 \times \exp(-D/R_0)$, as derived from simulation studies [51]. This results in two fit parameters: R_0, the scale parameter (i.e. the slope of the distribution) and ϵ_0, the extrapolated field strength at the shower core at observation level. The lateral distributions can also be fitted with a power law function [40], which seems to over-estimate the field strength close to the shower axis. Of particular interest is the scale parameter which describes the amount of signal decrease as function of distance to the shower axis, and its dependence on parameters of the EAS. Knowledge of the lateral extension with respect to polarization contributes to the understanding of the emission mechanism of the radio signal, as indicated by simulations [53]. In addition, the lateral characteristics can be related to important physical quantities, such as the energy or mass of the primary particle.

While the CC_{beam} is an average property over the measured radio signal in all LOPES antennae, the present research requires the investigation of the field strength recorded in individual antennae. Therefore, we use up-sampled data with a zero-padding method, to extend time series or spectra. The up-sampling method [40] is performed to reconstruct the original form of the signal between the sampled data points (12.5 ns spacing, 80 MHz frequency). Zeros are added in one domain and after Fourier-Transformation an interpolated series is obtained in the other domain. The zero-padding is applied in the frequency domain and gives a band-limited interpolation in the time domain. The up-sampling algorithm increases the sampling frequency artificially by a given factor (in this case to 640 MHz, with 1.5625 ns).

Moreover, when looking at the lateral profiles with an antenna-by-antenna and event-by-event basis, the question to be answered here is the following: does the form of

the lateral distribution for the EW polarization component differ from the NS polarization component? Despite considerations of measured events, from the KASCADE event selection (see Sec. 4.3) a sample of 99 LOPES events with signal recorded in both polarizations are simulated with the REAS3 Monte Carlo code. This allows the investigation of the lateral profiles for each polarization direction (EW and NS), for shower cores located close to the LOPES antenna array (within 90 m radius).

In Figs. 6.18 three different events are shown with the recorded field strength and the corresponding lateral profiles per polarization. The first event shows a dominant signal recorded in both polarization directions, the second event shows a dominant signal recorded only in the north-south polarization direction, and the third event shows a dominant signal only in the east-west direction respectively. Within them, three different cases of radio signal detection concerning the dual-polarization measurements are emphasized. Each case, shows a different lateral profile per polarization for the corresponding detection. The applied exponential fit function is estimated for each individual event and for each polarization respectively. Also for these examples, it can be seen that there is a flattening tendency in the lateral extend for both EW and NS polarization components, separately.

For the fitting procedure of the lateral profiles, a minimum number of 6 antennae with a signal-to-noise ratio > 3 for each individual antenna is required, including good quality of the fit (given by the relation $\chi^2/NDF \curvearrowright 1$). The fit results ($R_0$, ϵ_0) for the selected events are investigated for each polarization component. Showers with values of extrapolated field strength ϵ_0 between 0-100 μV/m/MHz, and values of scale parameter R_0 between 10-1000 m are selected as "good" candidates for the investigations discussed in the next Section. 86 events in the EW polarization component and 79 in the NS polarization component respectively, survived these requirements. No further cuts on EAS observables are applied, neither on energy of the primary particle, nor on the geometry of the shower.

6.5.1   Comparison between simulation and measured data

A sample of 99 LOPES events with recorded radio signal containing east-west and north-south polarization components are discussed. Not discussed are the events for which the applied exponential fit was not valid in east-west or in north polarization direction only, because of high noise level relative to the radio signal. The shower direction, particle number (N_e and N_μ), shower core position, and the primary energy of these (measured) selected events are used as input for REAS3 simulation of the radio emission. Protons are used as primary particles. To compare the simulation results with measured data, REASplot is used in order to filter the effective frequency band of the LOPES experiment (43-76 MHz). The output obtained from REASplot gives information about the maximum amplitude seen in each individual LOPES antenna, including the distance from single antenna to the shower axis for a corresponding arrival time. Results from both, simulation and measured data are called together for the fitting procedure of the lateral extend per polarization component. From the 99 successfully simulated showers, 86 events have "good" lateral fits in the EW polarization direction and 79 in the NS polarization direction respectively, while 71 events have good fits for both polarization at the same time per event-by-event basis. Their lateral distributions are studied for both polarization components (see Appendix B).
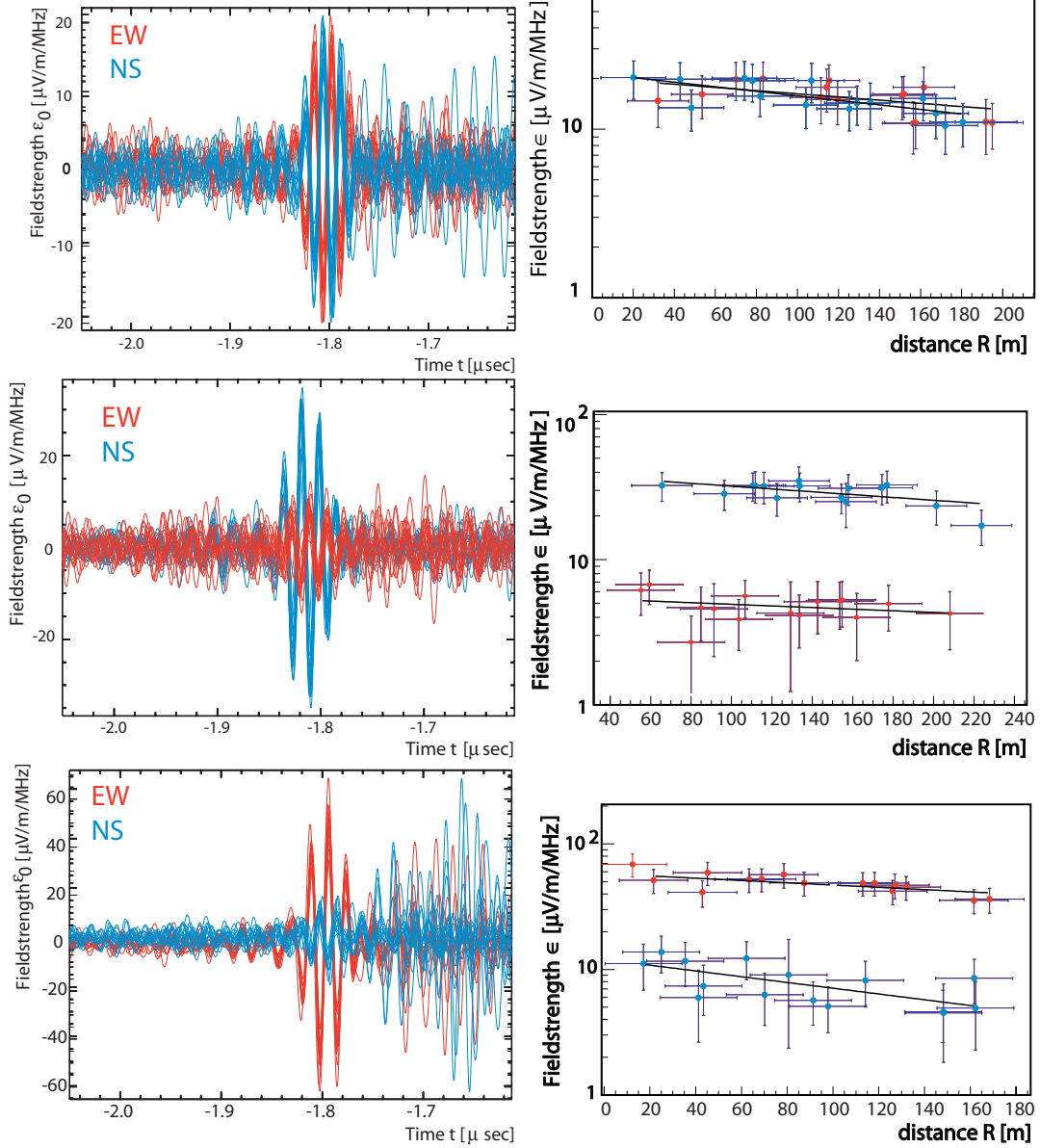
Figure 6.18: 1st event example, top panel ($\phi = 281°, \theta = 38.9°, \epsilon_0^{EW} = 20.19, R_0^{EW} = 457.9, \epsilon_0^{NS} = 23.3, R_0^{NS} = 302$) wi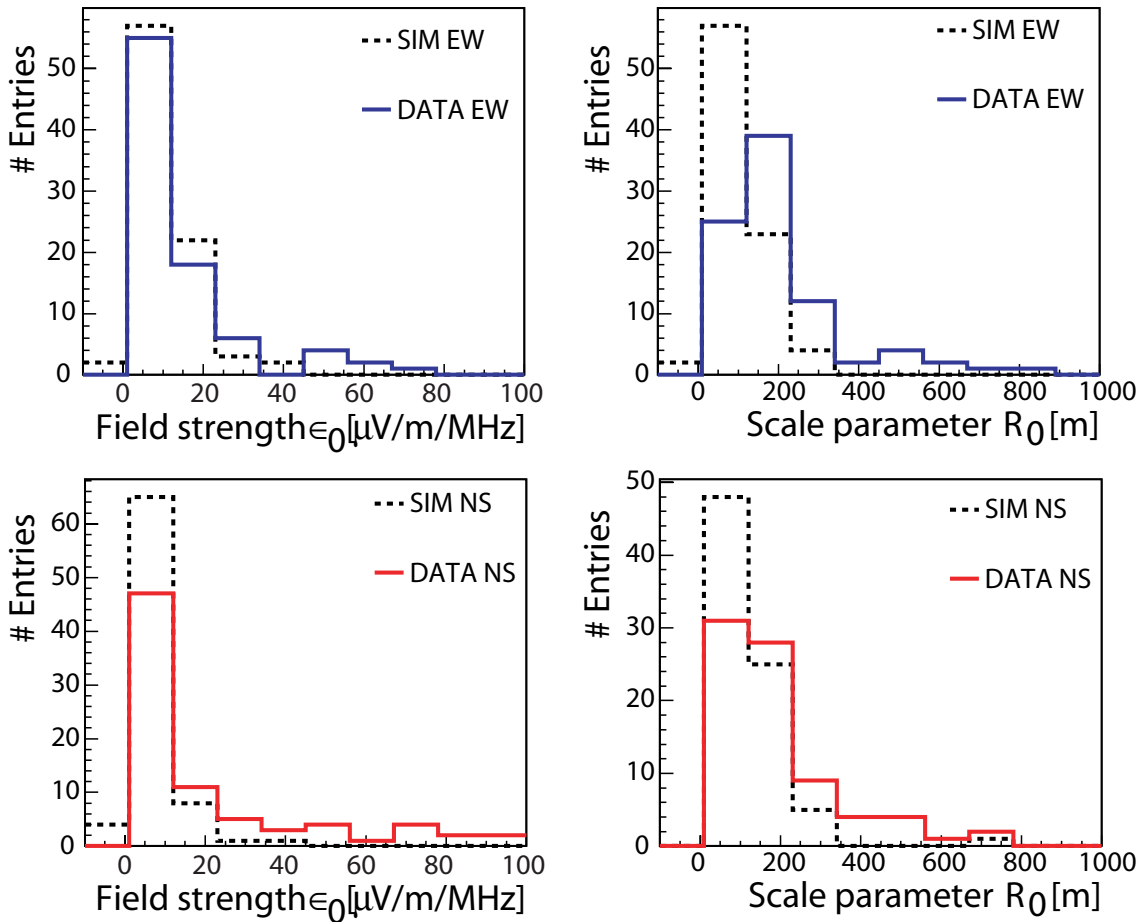th radio detection dominant in both polarization directions. 2nd event example, middle panel ($\phi = 245°, \theta = 42.5°, \epsilon_0^{EW} = 8.3, R_0^{EW} = 614.2, \epsilon_0^{NS} = 40, R_0^{NS} = 446.7$) with radio detection dominant mainly in the NS polarization direction. 3rd event example, bottom panel ($\phi = 352°, \theta = 37.5°, \epsilon_0^{EW} = 58, R_0^{EW} = 477.9, \epsilon_0^{NS} = 17.8, R_0^{NS} = 222.3$) with radio detection dominant mainly in the EW polarization direction.

Figure 6.19: Distributions of the field strength ϵ_0 and scale parameter R_0 from the lateral distribution of the sample of LOPES measured and simulated events. Black-dashed-line: entries of the simulation, and blue(red)-continuous-line: entries of the measurement. Both polarization directions are displayed (east-west: top panels, north-south: bottom panels)

The fit parameters, ϵ_0 and R_0, as results of the exponential function ($\epsilon = \epsilon_0 \times \exp(-D/R_0)$), are taken into account for the investigations. Comparing the extrapolated field strength (see Fig. 6.19) there is an remarkable agreement between the individual distribution of both polarization components, though measurements have a larger tail to higher field strength. Regarding the scale parameter, one can see that for simulations R_0 has a mean value of about 100 m, while measurements indicate values of R_0 of about 200 m. Again, the tendency for flatter measured lateral distribution, compared to simulations, is true for both polarization components.

In Fig. 6.20, the relation of ϵ_0 with R_0 for both, simulation and data, for each polarization direction, is shown. ϵ_0 values of both simulation and measured data have about similar order of magnitude. This is true for events detected in both polarization directions. It is different for showers detected in only one polarization component. When the simulation predict a low ϵ_0 in one polarization direction (i.e. below the threshold for detection), the measurements give a higher ϵ_0. This is due to the influence of the noise level on the reconstruction procedure. Values of R_0 are larger for measurements as well as larger errors of the fit occur. Also the flat events (large R_0) are not seen in simulations. No dependency between R_0 and mean distance to the shower axis is found (see Fig. 6.20, bottom panels).
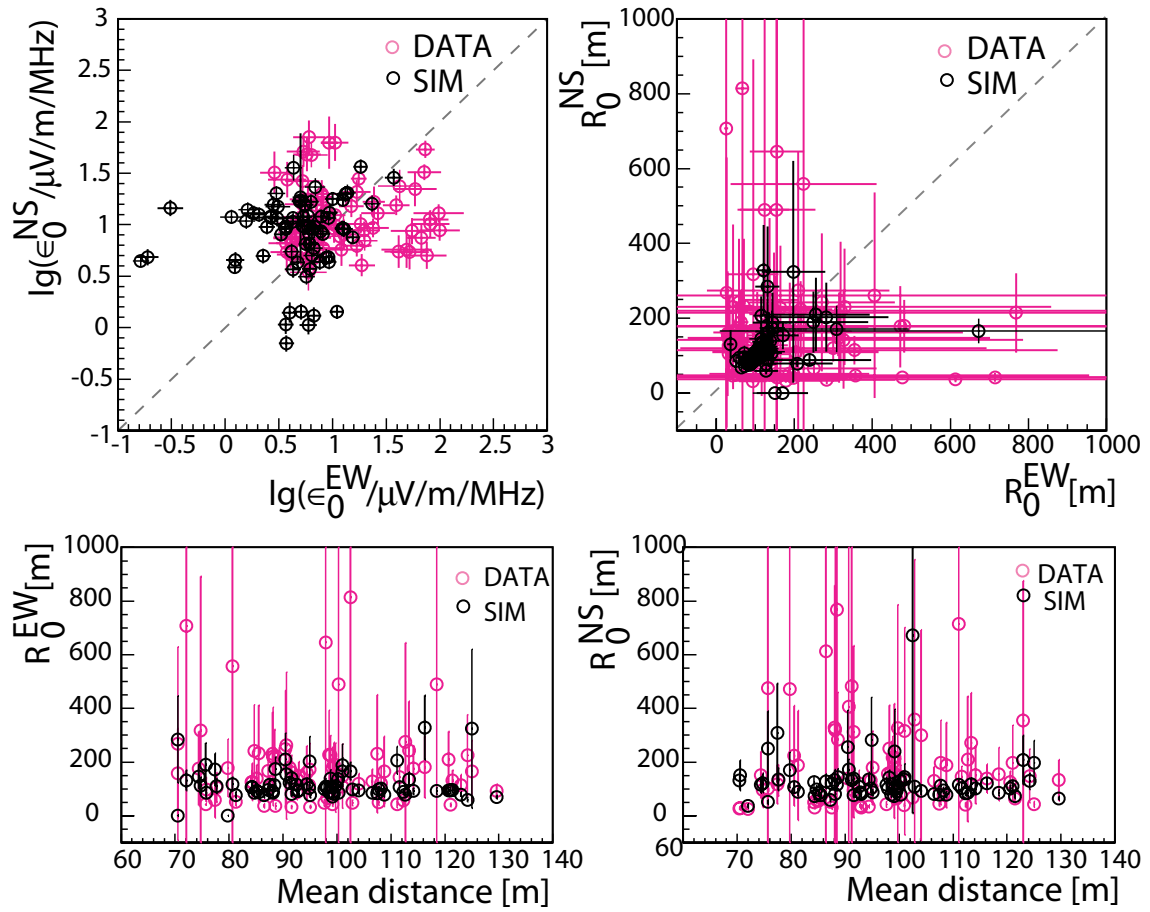
Figure 6.20: Relation of ϵ_0 (top left panel) with R_0 (top right panel) of east-west and north-south polarization directions, for both, measurement (pink) and simulation (black) results of the lateral profiles, independently. Large scatter is seen in the measured data compared with the simulation data, as well as large error for R_0 of values $> 200\ m$. Distributions of R_0 with the mean distance from observer to the shower axis, for both simulation (black) and measured (pink) data, per polarization (east-west: bottom left panel, north-south: bottom right panel). No correlation between them is seen.
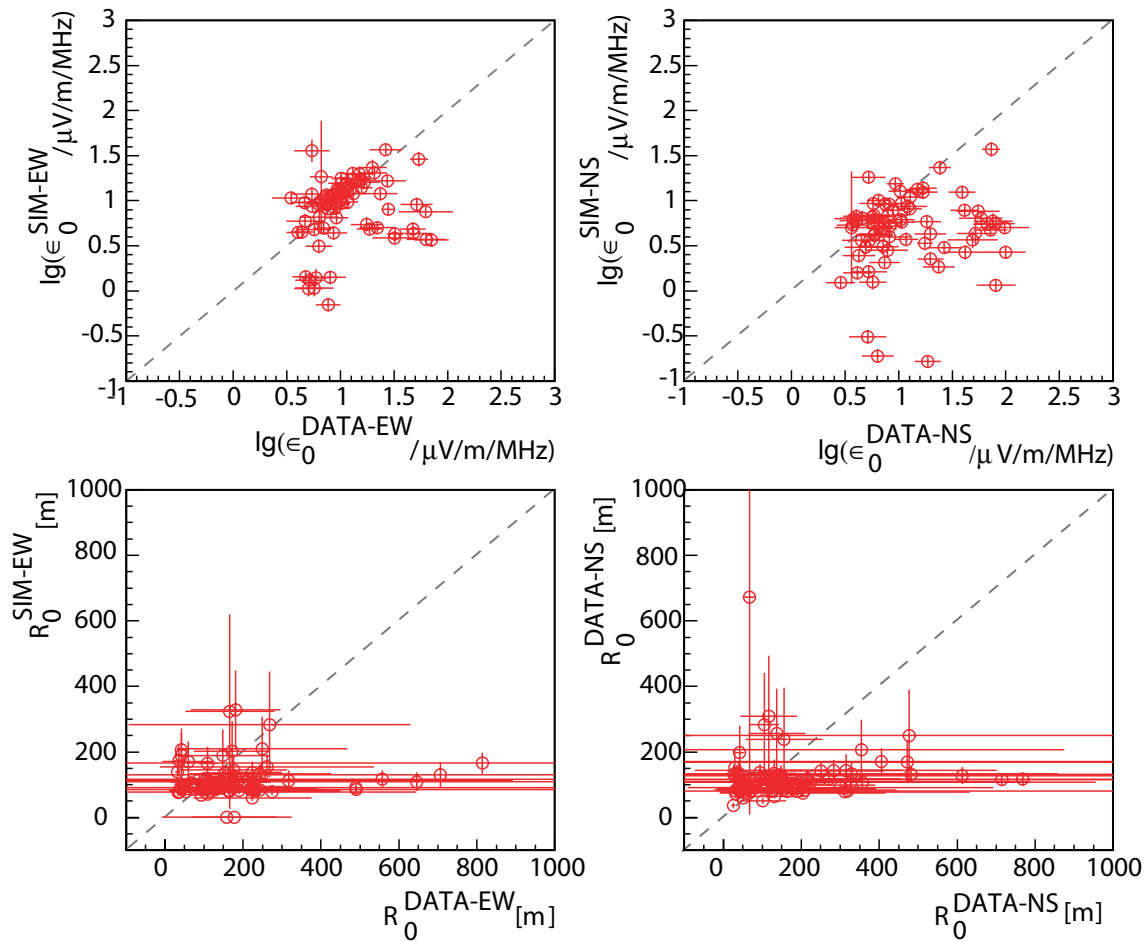
Figure 6.21: Relation of ϵ_0 (top panels) and R_0 (bottom panels) between simulation and measured data, per polarization direction (east-west: left panels and north-south: right panels). Good correlation of ϵ_0 between simulation and measured data is seen in the east-west polarization direction, with more scatter in the north-south, except that in measured data the scale parameter R_0 has larger values than 400 m (bottom panels), which can reflect the scatter seen in ϵ_0.
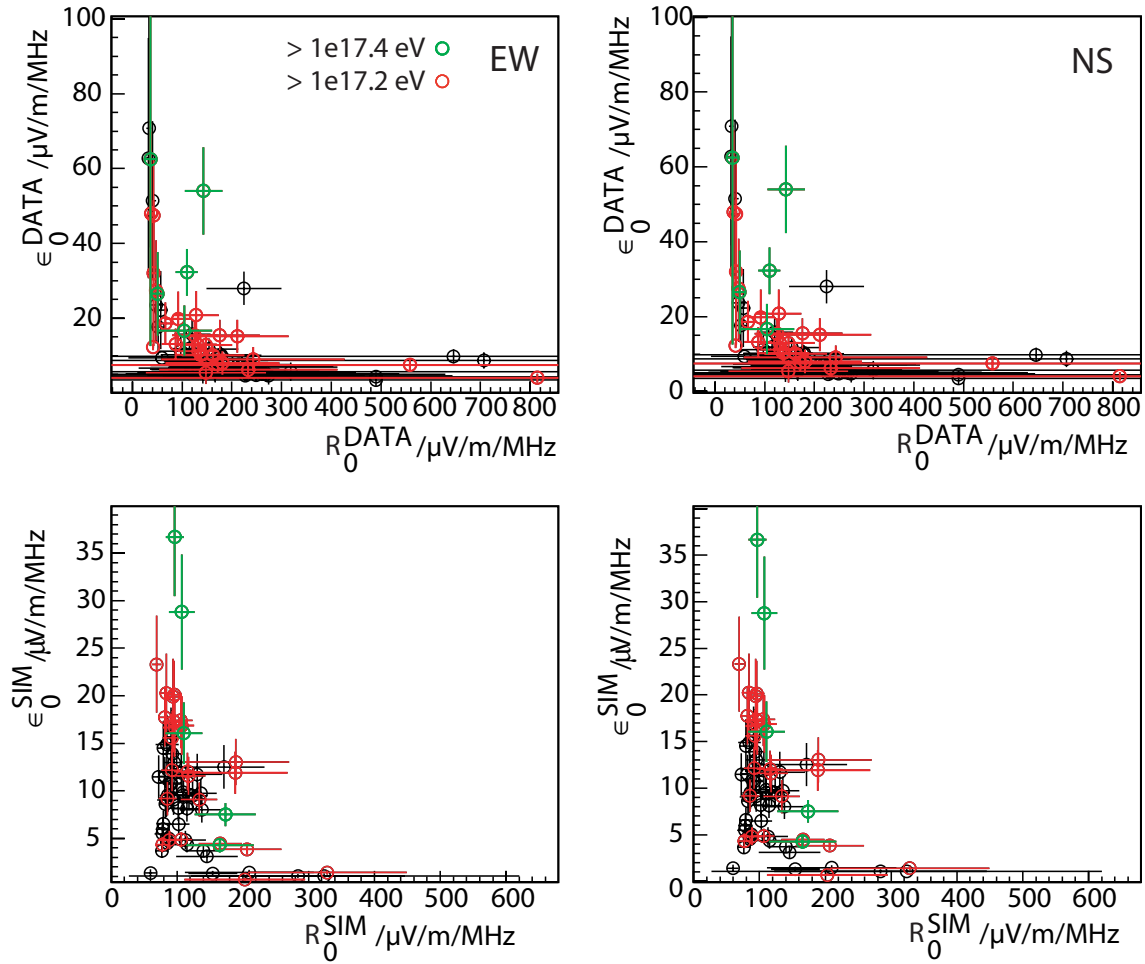
Figure 6.22: Relation of ϵ_0 with R_0 of measured data (top panels) and simulation (bottom panels) per polarization, for different ranges on the primary energy. No large values of R_0 for $E_p > 10^{17.4}$ eV (5 events) are found. No differences between the polarization components are found. The simulated values of R_0 are mainly around 100 m, as for measured data the scale parameter varies from about 100-200 m.
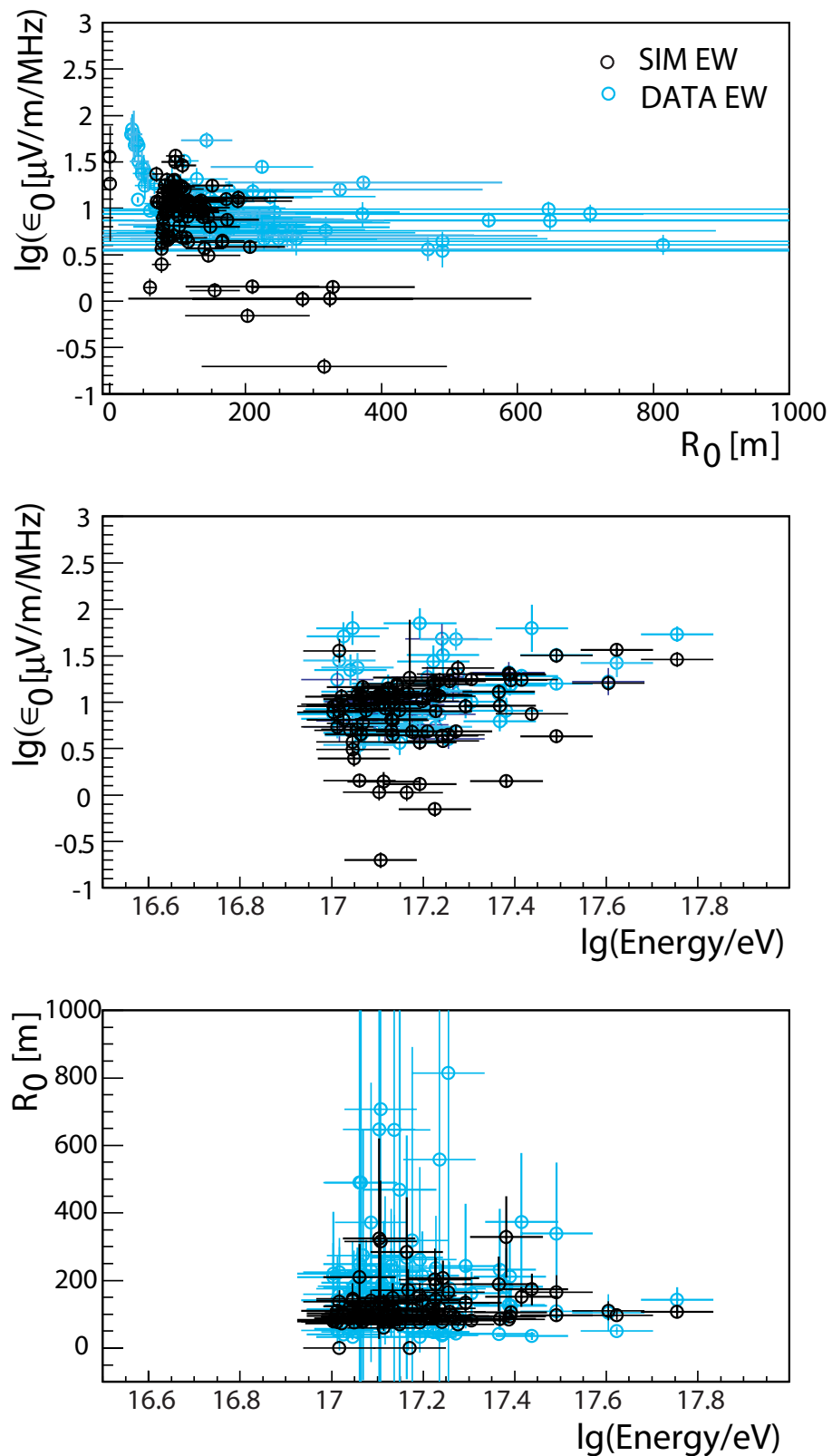
Figure 6.23: Distributions of ϵ_0 and R_0 as results of the fits on the lateral distributions for the sample of LOPES measured and simulated events with the primary energy. Blue open-circles represent the measured data and black open-circles the simulation data (both for the EW polarization direction). Included is also the distribution of the fit results (top panel). The statistical error bars are included. 20% error of the primary energy estimated by the KASCADE array is considered in simulations.
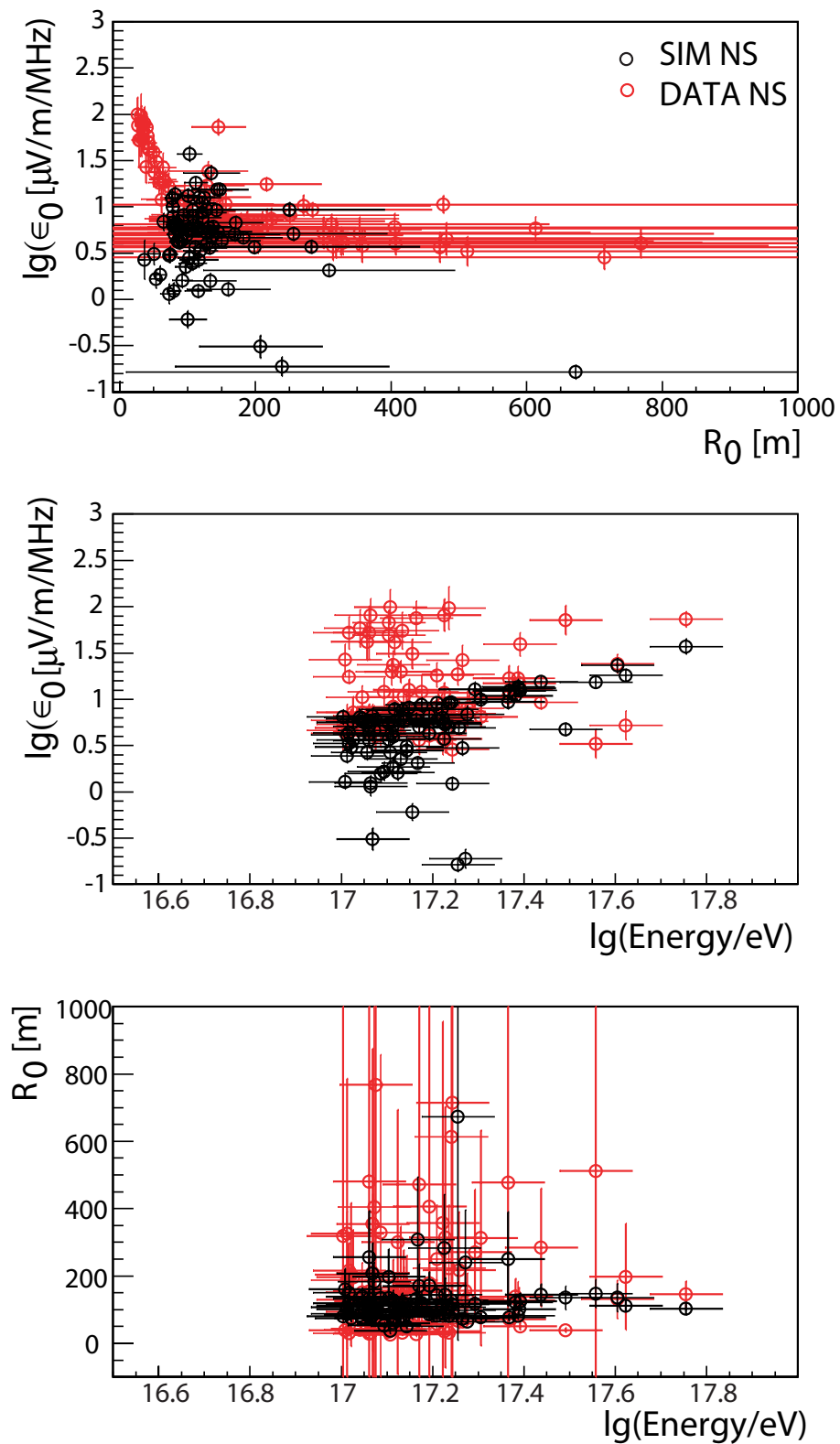
Figure 6.24: Same as Fig. 6.23, but for the NS polarization component.

In Fig. 6.21 the parameters of the fits for measurements and simulations are directly compared. It is clearly seen, that the simulations agree better with data in the EW polarization direction compared to the NS polarization direction.

The detection efficiency of LOPES antennae is significantly increased for shower cores within 90 m radius inside the antenna array at the KASCADE array. Thus, only KASCADE showers were used for comparisons with simulations. Since most of the non-reliable lateral profiles are having a large value of R_0 (fitting into the noise level makes R_0 large), a cut on the scale parameter was required. Events with scale parameter higher than 500 m show large systematics compared with the lower statistical errors of the scale parameter for values in the range of 100-200 m. This aspect is confirmed by the large corresponding values of the field strength seen in each antenna, e.g. for values of R_0 higher than 100 m, while for values lower than 100 m a tendency to flattening is observed instead (see Fig. 6.22). The flattening related to the high values of the scale parameter can be explained by the noise. The primary energy and the incoming shower direction might play an important role in this particular case. If we look now at the distribution of the fit parameters (ϵ_0 and R_0, see Fig. 6.22), by applying several cuts on the primary energy, one can see that for e.g. $E_p > 10^{17.4}$, high value of ϵ_0 gives low value of R_0, with low error bars per single event.

In Figs. 6.23, 6.24 the distributions of ϵ_0 and R_0 with primary energy are shown, as well as their intrinsic correlation (top panel) for simulation and data. An interesting feature is the obvious correlation of the ϵ_0 with R_0, at least for small R_0 values at a part of the measured events in both polarization directions. A clear dependence of ϵ_0 with primary energy is found (middle panel). However, no dependence for R_0 is observed (neither in simulation, nor in data: bottom panel). It should be claimed again, that the comparison between simulations and data lead to a better agreement for the EW polarization component than for the NS polarization component, where definitely a higher field strength is measured than expected. As the EW polarization component is more sensitive to the geomagnetic origin of the signal, and NS polarization component has a higher sensitivity to the charge excess contribution to the total signal, this can be another hint that this part is underestimated in the REAS3 simulations.

In conclusion, there is no major difference between simulation and measurement regarding the extrapolated field strength for each polarization component separately. The new definition of the start- and end-point in the particle track [54], which is assumed now in the current version of REAS3, seems to fit much better with the measurements than the old version of REAS2 [40]. Additionally, a dependence between ϵ_0 and R_0 can be observed in the measurement, but not in the simulation. A dependence of ϵ_0 on energy for both polarization components is found in both simulations and measurements. However, no dependence for R_0 is found, neither on the primary energy nor on the mean distance to shower axis. Overall, lower values for R_0 are found in the simulations (in both polarization directions), with mean value of about 126.4 m in NS and 118.2 m in EW respectively. Besides the usual exponential decay behaviour of the applied fit on the lateral extend, a flat profile for a few showers is found in data and for first time also in simulations (see Appendix B, e.g. Fig. B.1, panels 5,6 from top down). This phenomena is not fully understood, though may be explained by the low distance to the shower axis, as it is the case for

these selected events (triggered by the KASCADE array). The same features were also observed in the previous studies of LOPES-30 measurements of the east-west polarization direction for the electric field only [40].

6.6   Polarization vector

This analysis is dedicated to directly examine the polarization of the signal at antenna level. Within the LOPES-pol set-up 5 antennae with sensitivities for both polarizations (EW and NS) are installed at the same place. This allows the record of the radio signal in both polarization components at the same place and at the same time. From the reconstruction of the radio signal (including up-sampling) the maximum field strength of each individual antenna (for each polarization direction) is obtained for individual events. In addition to the lateral distribution analysis, here also the sign (+ or -) of the field strength is considered. By this, we can gain information on the polarization direction $P_{directivity} = \tan^{-1}(FS_{NS}/FS_{EW})$ and its magnitude ($P_{magnitude} = \sqrt{FS_{EW}^2 + FS_{NS}^2}$) respectively. For all selected events we calculate these values for all 5 antennae (i.e. 10 channels). For the recorded signals in both (EW and NS) polarization directions a signal-to-noise ratio larger than 2 is required. The KASCADE event sample is used for this analysis. Either the positive or negative maximum of the highest absolute value of the radio signal is used in further calculations, e.g. in Figs. 6.25, 6.26.

Fig. 6.25 shows the distribution of the field strengths, of the magnitude and directivity of the polarization vector, and of the distance of the antennae to the shower center. No special behaviour in these distributions are found, except that due to the requirement of a minimum field strength for detection not the full range of directivity is populated. Fig. 6.26, left panel, shows the correlation of the NS with the EW polarization components of the measured field strength (pink colour), including their individual prediction as given by the $\vec{v} \times \vec{B}$-model (green colour), which shows values close to zero (while measured data does not). Same figure, right panel, shows the correlation between the field strength reconstructed in the NS and EW polarization directions divided by the total amplitude ($\equiv P_{magnitude}$). One can clearly see the four quadrants of the circle, which describe the $\mp$ sign of the signal. The vector directivity is defined with zero degree at the positive X-axis and going counter-clockwise to 360 degree. The signal sign of measured data is uniformly distributed along all quadrants, while this is not true in the case of $\vec{v} \times \vec{B}$-directivity (mainly distributed along the - + and - - quadrants).

Fig. 6.27 displays the sky maps (as function of azimuth and zenith angles) of the field strength recorded in EW and NS polarization components respectively, where the information of the radio ($\pm$) and the height of the field strength is combined. We observe that for the EW polarization component positive signs are dominating for showers coming from the North direction, and for the NS polarization component positive signs are dominant in East and West directions.

The sign of the field strength was already studied by the CODALEMA experiment [46], where the simplified geomagnetic model $\vec{v} \times \vec{B}$ was assumed. The $\vec{v} \times \vec{B}$-unit vector predicts that for the EW polarization detection, a signal with positive sign is expected to be dominant for showers coming from the Northern part of the geomagnetic angle (in Karlsruhe), and negative sign for showers coming from

the Southern part. For the NS polarization detection, signal with positive sign is expected to be dominant for showers coming from East, and signal with negative sign to be dominant for showers coming from West. This behaviour get's even a bit clearer by looking to Fig. 6.28, where the number of signals with positive and negative signs are displayed in dependence with the azimuth angle of the incoming showers.

In Figs. 6.29 6.30 the dependencies of the vector magnitude and the directivity of the data is compared with expectations of the $\vec{v} \times \vec{B}$ -model. In the model only the geometry of the measured events is taken into account, and thus its vector magnitude and directivity are calculated (see Chapter 5). For all plots, the corresponding profiles (with the rms of quantities) are plotted on top of the scatter points. The clear correlation of the vector magnitude with the primary energy is seen in Fig. 6.29 (right hand, 4th panel from top). A power law is fitted to the profile of the primary energy, which results in a slope of index $\backsim$ 1. There is no dependence, as expected, between vector directivity and energy of the primary particle (see Fig. 6.30).

If one compare now the dependence of the vector magnitude with the azimuth, zenith and geomagnetic angles in measured data, there are some hints for similar features compared to the model. But the spread, showing the influence of the amplitude in the measured data, is too large to make any conclusive statement. Also, the position of the shower core to the dual-polarized antennae may play a role here. The correlations of the $\vec{v} \times \vec{B}$ -model's magnitude and directivity applied to shower geometry are well understood, if one remembers that $\vec{v} \times \vec{B}$ describes only the dependencies of the geomagnetic emission on the shower geometry, as follows:

(i.) the magnitude does not correlate with energy of the primary particle;

(ii.) the magnitude increases with geomagnetic angle;

(iii.) the magnitude is larger for showers coming from North (also from South);

(iv.) the magnitude depends dominantly on azimuth and slightly on zenith angle;

(v.) the directivity concentrates on the angular range from 90° to 270°;

(vi.) the directivity does not depend on the energy of the primary particle, zenith and geomagnetic angle;

(vii.) the directivity depends on azimuth angle where a flip in the sign is observed for events coming from South (parallel to Earth magnetic field)

The surprisingly clear dependence of the $\vec{v} \times \vec{B}$ -directivity on the azimuth angle is not seen in the data. The uncertainty assigning the sign to the maximum measured amplitude in the individual antenna signal is probably too large ($\approx 20\%$) for detailed comparisons. But, due to these clear dependencies in the $\vec{v} \times \vec{B}$ -model, such an analysis can be very promising in justifying the emission mechanism and needs further more detailed investigation.
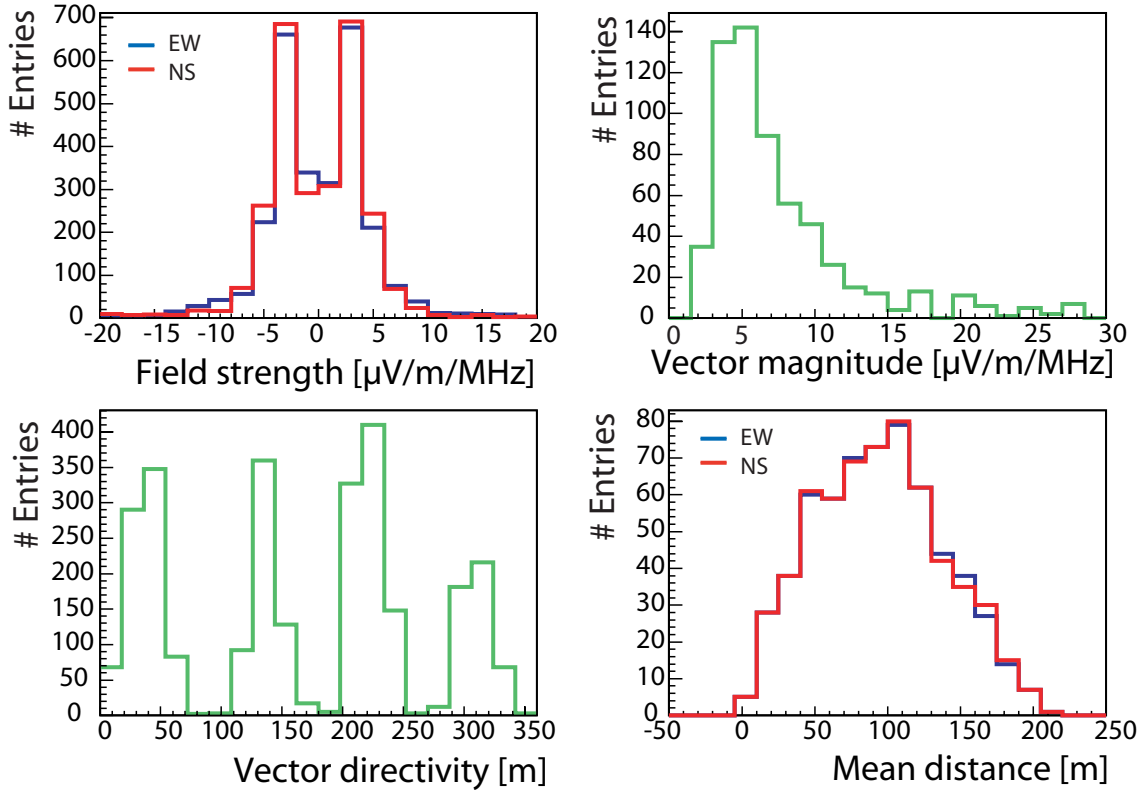
Figure 6.25: Histograms (from left to right) of reconstructed field strength, calculated vector magnitude, vector direction, and distance to the shower axis. KASCADE showers with energy larger than 10^{17} eV as seen by the 5 dual-antennae.
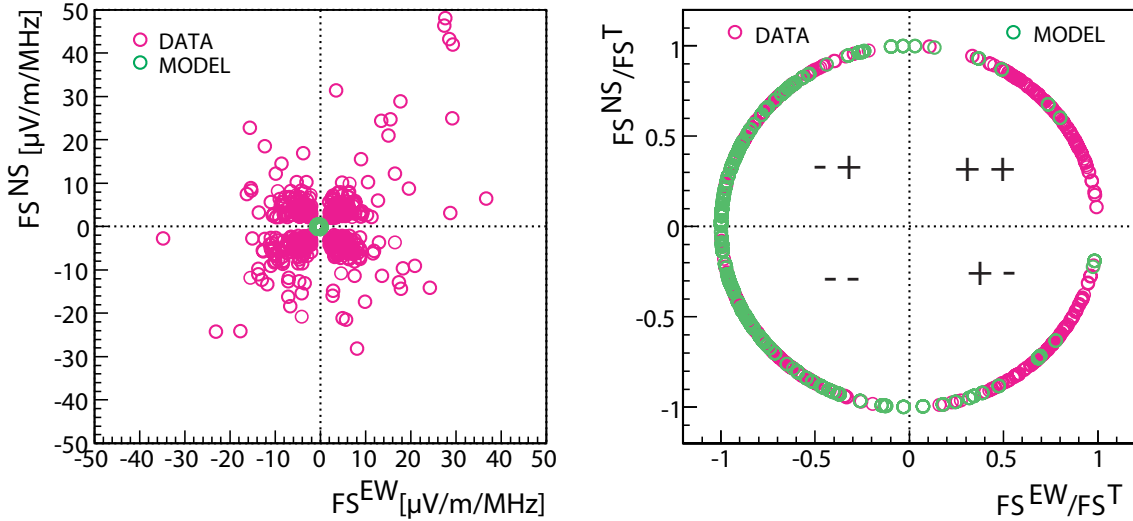

Figure 6.26: In the scatter plot, left panel, the signal recorded in the EW polarization component versus the signal recorded in the NS, respectively (pink colour: data, green colour: $\vec{v} \times \vec{B}$ -model) is shown. Values of $\vec{v} \times \vec{B}$ -amplitude are close to zero, as by definition the maximum value is one. In the right panel, the field strength in the NS polarization component divided by the total amplitude versus the filed strength in the EW polarization component divided by total amplitude is shown.
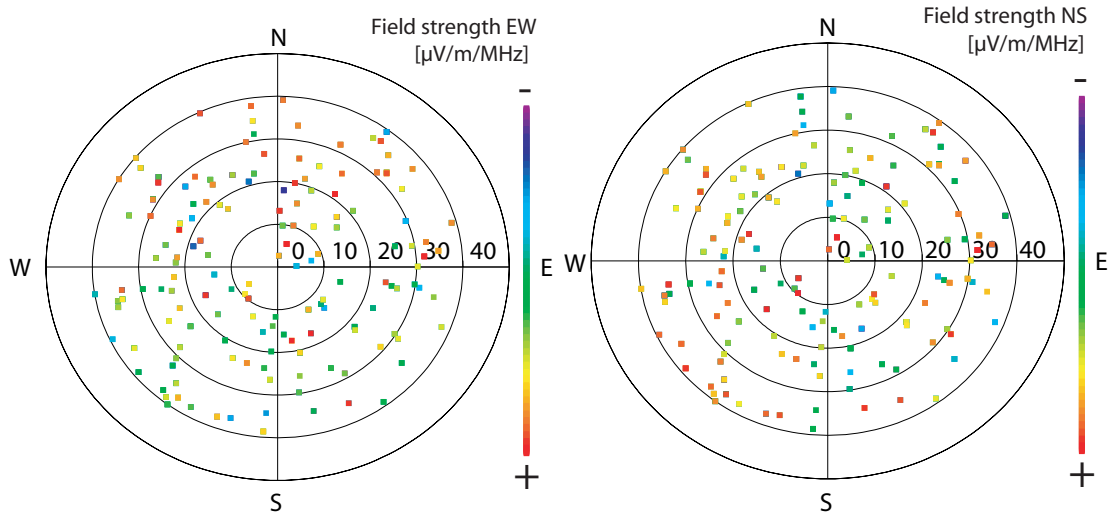
(a) Field strength seen by the east-west polar-(b) Field strength seen by the north-south po-
ized channels. larized channels.

Figure 6.27: Sky maps of the events seen by the 5 dual antennae, with the sign $\pm$ of the
field strength. A cut on absolute values of the field strength (recorded in EW and NS
polarization components) larger than 2 μV/m/MHz was applied, in order to avoid biased
events with field strength values close to the noise.
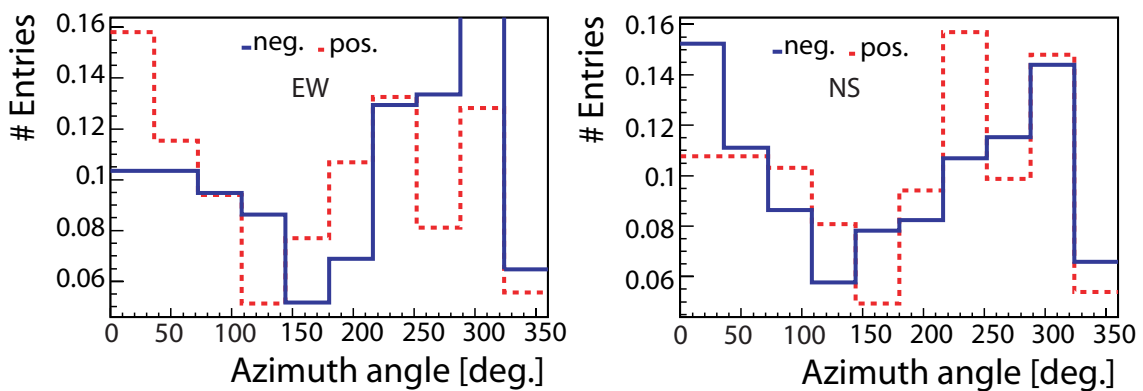
Figure 6.28: In the normalized histogram the distribution of the azimuth angle for each
polarization (east-west (left panel) and north south (right panel)) the signal sign $\pm$ is
shown. For the east-west detection the positive sign is dominant in the north, and for the
north-south detection the positive sign in dominant in the west.
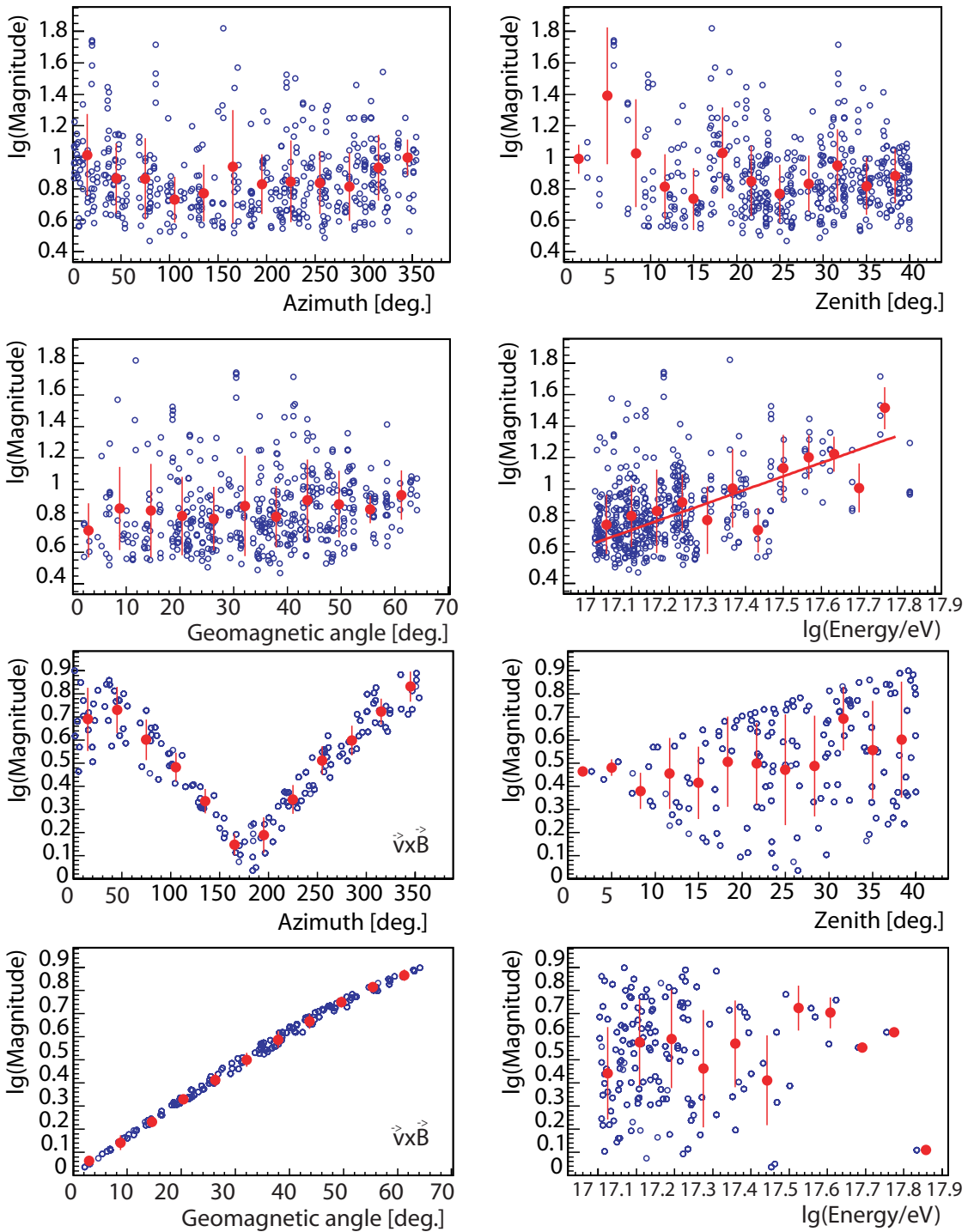
Figure 6.29: The vector magnitude (i.e. $P_{magnitude} = \sqrt{FS_{EW}^2 + FS_{NS}^2}$) of measured data is shown in dependency with the air shower angles (e.g. ϕ, θ, α, including the primary energy $E_p > 10^{17}$ eV. A power law function is applied to the binned data (red full circles) plotted on top of the scatter points (blue open circles) with a index ~ 1 (4 top panels). Same dependences but as application to the $\vec{v} \times \vec{B}$ -amplitude. Clear dependencies with azimuth and geomagnetic angle are seen instead, with much spread in the zenith dependency, because of $\theta = 25°$ which is similar with the incidence or the Earth magnetic field.
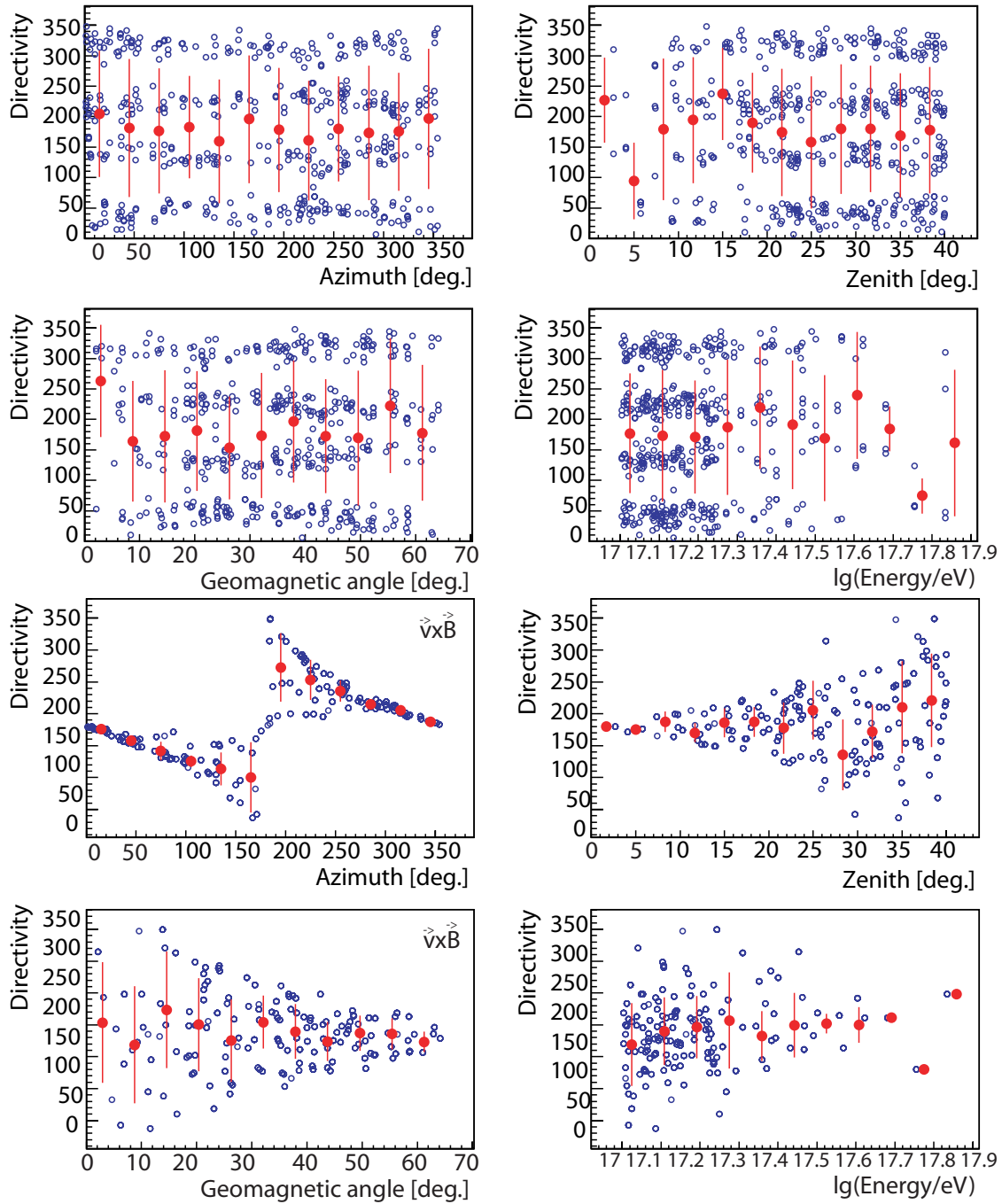
Figure 6.30: Same as Fig. 6.29, but for the vector directivity ($P_{directivity} = \tan^{-1}(FS_{NS}/FS_{EW})$) applied to measured field strength (4 top a panels), as well as to $\vec{v} \times \vec{B}$ -model

7. Summary and Outlook

By coincident measurements of LOPES and the KASCADE-Grande experiment valuable characteristics of the radio signal is investigated, e.g. the dependence on primary energy, direction and distance to shower axis. Radio detection of extensive air showers is an important issue because it can help in the understanding of the energy spectrum and mass composition of high energy cosmic rays, see [55]. The aim of this thesis was to understand and investigate the radio signal, analysing related dependencies with shower parameters in respect to the polarization issue. In particular, the knowledge of the polarization characteristics is mandatory for the interpretation of experimental measurements to verify the geomagnetic origin of the radio emission initiated by the atmospheric showers.

The LOPES experiment was performing dipole measurements for about 3 years, from end of 2006 until end of 2009. From the large number of events detected in both polarization directions two shower selections on both, KASCADE and Grande trigger information, were used in this studies for energy of the primary above 10^{17} eV. With the pulse height reconstructed independently for each polarization direction, east-west and north-south, valuable knowledge of the radio signal was obtained with respect to the polarization aspects. Instrumental corrections (e.g. calibration of amplitude, phase and time), radio frequency interference narrow band RFI suppressions, Fourier transforming data to frequency domain are considered in the standard pipeline reconstruction. A beam forming is performed into the direction to the shower axis. The used radio observable in the EAS investigations is the so-called cross correlated beam (the CC_{beam}). But, to be independent of the amplitude, the pulse height ratio was also studied (the recorded signal in the north-south polarization direction versus the signal recorded in the east-west direction). Investigating this ratio in individual showers allowed us to study the polarization characteristics of the signal independent of primary energy and distance of the antennas to the shower axis, i.e. in particular the dependence of the polarization on the direction of the incoming primary particle. Correlations of the pulse height ratio of both polarization components with the azimuth, as well as with the geomagnetic angle were compared with predictions of a first order approximation of models based on a geomagnetic origin of the emission, as well as with full simulations.

The dependence on the primary energy, direction of the incoming shower axis (by its azimuth, zenith and geomagnetic angle) and distance to shower axis were used in the parametrization of the radio pulse on each polarization direction. This allows the estimation of the radio pulse by integrating in a formula only the parameters of the measured shower geometry (in the LOPES case, EAS information provided by the KASCADE-Grande particle detector array). The lateral extent of the field strength seen in each antenna as distance to the shower axis could be fitted by an exponential function. The fit results were investigated and no correlation between the scale parameter of the lateral profile with any EAS observables could be found. For the first time, the estimation of the polarization vector per dipole LOPES antenna was possible now. The dependence of the vector magnitude with the primary energy was found, with the index of the fitted power law with index close to 1.

The emission is polarized in the direction perpendicular to the air shower axis and geomagnetic field. The polarization characteristics follow a behaviour described by a unit polarization vector: $\vec{v} \times \vec{B}$. The absolute amplitude of the electric field in a first approximation can be considered to be proportional to the Lorentz force. As the polarization measurements are required for the full measurement of the radio signal, detailed comparisons between measurements and simulations of radio emission were performed. Having analysed the full Monte Carlo simulation of the radio emission (which includes the charge excess), as well as the simplified geomagnetic model (which treats the pure shower geometry), it allowed us to compare both with measured data. Analysing a sample of simulated events, we could find a disagreement between the REAS3-simulated amplitude and the $\vec{v} \times \vec{B}$ -amplitude, concerning showers coming from the North and South directions and of vertical showers. Thus, REAS3 predicts detection in both polarization directions (EW and NS), while the $\vec{v} \times \vec{B}$ model gives zero amplitude in the NS polarization component. Comparing both approaches with the measured data, for which we have access to full azimuth ($\phi = 0° - 360°$) and zenith ($\theta = 0° - 40°$) angles, we found that indeed there is valid detection in both polarization directions for showers arriving mainly from North directions. This behaviour is also confirmed by investigating the pulse height ratio (NS/EW polarization components).

Summarising, four different analysis were performed for related investigations toward polarization aspects, as follows:

(i) CC_{beam} dependencies: Looking for shower dependencies on the amplitude of the EW and NS polarized signals. The result here is that generally, predictions of a pure geomagnetic origin of the radio emission are confirmed (in particular for the EW polarization component), but there are some deviations (in particular for the NS polarization component) which can be linked to a contribution from charge excess in the shower.

(ii) CC_{beam} parametrization: Verifying whether NS and EW polarization components have same "calibration". The result is that generally, yes, they are similar if one takes into account the $\vec{v} \times \vec{B}$ polarization dependence of the geomagnetic effect. First hints seen so far are that for large distances the exponential function does not describe well the lateral distribution function (LDF).

(iii) Lateral distribution: Verifying whether NS and EW polarization components have same LDF (analysis on a single-antenna basis). The result shows similarities

between the two polarization components, except of the fact that in the case of the NS polarization component the deviation to the simulation is larger than in the EW polarization component. This can be interpreted as hint that the contribution from non-geomagnetic emission (e.g. by charge excess) is slightly underestimated in simulations (in this case, performed with the REAS code).

(iv) Polarization vector (analysis on a single-antenna basis): Looking if the geomagnetic effect describes the polarization features. From comparison with theoretical predictions, the $\vec{v} \times \vec{B}$ -model clearly shows azimuthal dependencies (for both, vector magnitude and its directivity), while this is not obvious in measured data. The uncertainty assigning the sign to the maximum measured amplitude in the individual antenna signal ($\approx 20\%$) is probably hampering more detailed comparisons. Further experiments will have a better sensitivity to the polarization vector. Than such analysis will be very convincing, as the simplified geomagnetic model expectations are very promising for distinguishing different radio emission mechanisms.

In conclusion, the geomagnetic effect is dominant, but definitely there is additional contribution (most probably from the charge excess induced during the shower development in the Earth'atmosphere), where the amount of this contribution is still an open question. The reason to looking for all these investigations (more quantitatively than qualitatively) is that the radio signal is not fully understood, i.e. there is always a large uncertainty if the models or expectations are really true. However, the geo-synchrotron effect proposed as the main emission mechanism in the radio emission initiated by the atmospheric showers could generally be confirmed by the clear dependence of the recorded radio signal on the ground and the geometry of the shower. The dependence of both polarization components of the signal, east-west and north-south, independently (as well as of their ratio), is seen in the correlation with the azimuth and geomagnetic angles. This verifies the geomagnetic effect as (mainly) dominant mechanism in the radio emission mechanism.

7.1 Research & Development for large scale application

The digital interferometry (e.g. LOPES, the pioneer experiment in the radio technique) is the re-discovered technique which is being used in a modern generation of the air shower experiments. Traditional ground particle detector, optical telescope and digital interferometry all together play an important role in measuring cosmic ray air showers, yielding separate and complementary observations. A digital radio antenna records the radio flashes of charged cosmic particles produced in the air shower. Due to the interaction with the Earth's magnetic field electrons and positrons as the main part of the shower body produce the radio flashes, which may be measured 24h a day.

The LOPES experiment was proposed to test the properties of air shower radio emission, and it has been proven so far that it can be used for the measurement of high energy cosmic rays. Its objectives are to understand the recorded radio pulse and correlate it with air shower parameters, understand the emission mechanism and pave the way for the use of the radio technique in current and future experiments. For applications at the Pierre Auger Observatory, inside LOPES we have developed

$LOPES^{STAR}$ (a Self Trigger Array of Radio detectors for LOPES [30]). Preliminary tests of self triggered antennas have been done, at both sides by LOPES and by the Pierre Auger Observatory. The possibility to use LOPES as a self-triggering antenna system is now investigated at the South part of the Pierre Auger Observatory (by AERA - an Auger Engineering Radio Array [56]). Besides this, at AERA different antenna types provided by the French-pioneer CODALEMA [47] and by the Dutch-designed LOFAR astronomical telescope array [57] are also tested. For example, the good directional accuracy reachable with radio interferometers will significantly improve clustering studies in search for point sources [57].

Once we have understood how the radio techniques works, how to handle the instrumental effects in the detailed digital processing (the reconstruction) of the radio signal, we open a new window in measurements of the most energetic particles coming from the Universe. Furthermore, we improve and optimize the hardware of the radio technique for large scale application in ultra high-energy cosmic ray experiments, like Pierre Auger Observatory and LOFAR. First approaches using the radio technique at the Pierre Auger Observatory and at a first LOFAR station are in progress. The highly important experience for such applications will be provided by the LOPES measurements. With the unique opportunity to have the LOPES radio antenna array placed inside the traditional and well-developed particle detector array KASCADE-Grande, LOPES allows the most valuable information of the radio signal achieved so far. Valuable dependencies of the radio signal with the EAS observables were found. A very promising area involves composition studies. The number of electrons integrated over the entire shower, revealing the primary particle energy, is difficult to determine with particle detectors: only a small fraction of these electrons reach the ground, due to their short absorption length. Muons, on the other hand, reach the ground largely unharmed, and their number is higher for showers produced by an iron nucleus compared to proton-induced, or even γ-induced, showers. Hence, a super-hybrid (combined radio and muon-detector, including fluorescence) detector array could determine the spectrum and composition of energetic cosmic rays.

Besides of the fact that inclined air showers provides a larger range of geomagnetic angles, they allow the vertical polarization component to be recorded. Taking this aspect into account, the polarization configuration of the LOPES antennas has been changed. Tests of a new design of three-pole antennas are under investigations at the LOPES site. The three-pole antenna configuration, and thus incorporating all three polarization components of the electric field (east-west, north-south and vertical) allows the measurement of the full signal. This follows as the fourth configuration in the life-time of the LOPES experiment.

A. Pulse height parametrization

A.1 Method: Iterative procedure

For the parametrization of the pulse height, an iterative procedure is being used on the three dependencies for the EAS observables: the incoming shower direction by the simplified geomagnetic model, the distance from observer to shower axis, and the primary energy. With all the EAS information provided by the KASCADE-Grande experiment, now we can estimate the radio pulse on each singe polarization directions, east-west and north-south. The step-by-step procedure is presented here in three steps. The results of the third step are used in the final pulse height estimation.

First iterative step, I

I.a. "$P_v = \vec{v} \times \vec{B}$" approach

$$Y = \varepsilon^{'} = CC_{beam}^{EW} \times \frac{10^{17} \; eV}{E_p};$$

$$X = P_v^{EW};$$

$$Fit function : FB1 = Y = a + bX;$$

$$Assumption : q_{B1} + s_{B1}X;$$

$$Fitresults : q_{B1} = a_1, s_{B1} = b_1;$$

Notes:
α is the angle between the shower axis and the Earth's magnetic field;
CC_{beam}^{EW} is the reconstruction of the pulse height into the east-west direction;
E_p is the estimated primary energy by KASCADE-Grande;
a_1 and b_1 are the result parameters of the linear fit of the function $FB1$ applied to data.

I.b. "Mean distance" approach

$$Y = \ln(\varepsilon' \times \frac{FB1 \to Eval(0.45)}{FB1 \to Eval(fabs(P_v^{EW}))})$$

$$X = D[m];$$

$$Fit function : FD1 = Y = a - X/b;$$

$$Assumption : s_{D1} - X/R_{D1};$$

$$Fitresults : R_{D1} = b_2, s_{D1} = e^{a_2}$$

Notes:
D is the distance from observer to the shower axis;
a_2 and b_2 are the result parameters of the exponential fit of the function $FD1$ applied to data.

I.c. "Primary energy" approach

$$Y = \log_{10}(\varepsilon' \times \frac{FB1 \to Eval(0.45)}{FB1 \to Eval(fabs(P_v^{EW}))} \times \frac{\exp FD1 \to Eval(100m)}{\exp FD1 \to Eval(D)});$$

$$X = \log_{10}(E_p/10^{17})[eV];$$

$$Fit function : FE1 = Y = a + bX;$$

$$Assumption : s_{E1} \times E^{p_{E1}};$$

$$Fitresults : p_{E1} = b_3, s_{E1} = 10^{a_3}$$

Notes:
E_p is the estimated primary energy by KASCADE-Grande;
a_3 and b_3 are the result parameters of the linear fit proportional to a power low function which describes the energy dependence.

Second iterative step, II Obs: same fit function as Iterative normalization I

II.a. "$\vec{v} \times \vec{B}$" approach

$$Y = \varepsilon' \times \frac{FE1 \to Eval(10^{17}eV)}{FE1 \to Eval(E_p)} \times \frac{\exp FD1 \to Eval(100m)}{\exp FD1 \to Eval(D)};$$

$$X = P_v^{EW};$$

$$Fit function : FB2$$

II.b. "Mean distance" approach

$$Y = \log(\varepsilon' \times \frac{FE1 \to Eval(10^{17}eV)}{FE1 \to Eval(E_p)} \times \frac{FB2 \to Eval(0.45)}{FB2 \to Eval(fabs(P_v^{EW}))});$$

$$X = D[m];$$

$$Fit function : FD2$$

II.c. By primary energy:

$$Y = \log_{10}(\varepsilon' \times \frac{FB2 \to Eval(0.45)}{FB2 \to Eval(fabs(P_v^{EW}))} \times \frac{\exp FD2 \to Eval(100m)}{\exp FD2 \to Eval(D)});$$

$$X = \log_{10}(E_p/10^{17})[eV];$$

$$Fit function : FE2$$

Third iterative step, III Obs: same fit function as Iterative normalization II

III.a. "$\vec{v} \times \vec{B}$" approach

$$Y = \varepsilon' \times \frac{FE2 \to Eval(10^{17}eV)}{FE2 \to Eval(E_p)} \times \frac{\exp FD2 \to Eval(100m)}{\exp FD2 \to Eval(D)};$$

$$X = P_v^{EW};$$

$$Fit function : FB3$$

III.b. "Mean distance" approach

$$Y = \log(\varepsilon' \times \frac{FE3 \to Eval(10^{17}eV)}{FE2 \to Eval(E_p)} \times \frac{FB3 \to Eval(0.45)}{FB3 \to Eval(fabs(P_v^{EW}))};$$

$$X = D[m];$$

$$Fit function : FD3$$

III.c. "Primary energy" approach

$$Y = \log_{10}(\varepsilon' \times \frac{FB3 \to Eval(0.45)}{FB3 \to Eval(fabs(P_v^{EW}))} \times \frac{\exp FD3 \to Eval(100m)}{\exp FD3 \to Eval(D)});$$

$$X = \log_{10}(E_p/10^{17})[eV];$$

$$Fit function : FE3$$

A.2 Pulse height estimation

With the results from iterative step III, one can estimate the radio pulse height. Same procedure of the estimation of the pulse height is used for both polarizations, independently, by using the $|\vec{v} \times \vec{B}|_{NS}$-unit cross product vector projected in the north-south and east-west directions, separately, as follows:

This case: (b1 $\neq$ 0)

$$\epsilon = (a_1 \cdot a_2 \cdot a_3) \cdot (|P_v^{EW,NS}| + \frac{a_1}{b_1}) \cdot e^{\frac{-R_0}{b_2}} \cdot (\frac{E_p}{10^{17}eV})^{b_3} \frac{\mu V}{m \cdot MHz}$$

Other case: (b1=0)

$$\epsilon = (a_1 \cdot a_2 \cdot a_3) \cdot |P_v^{EW,NS}| \cdot e^{\frac{-R}{b_2}} \cdot E_p^{b_3} \frac{\mu V}{m \cdot MHz}$$

(a) The cross-product   (b) The right-hand rule
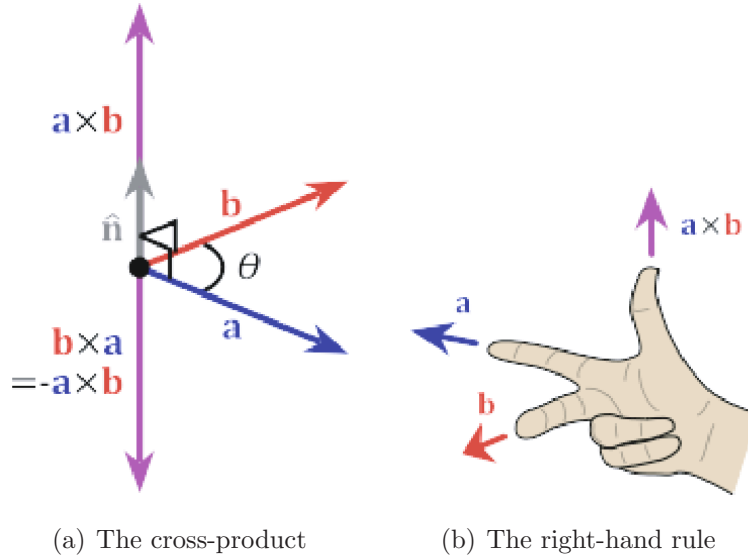
Figure A.1: The cross-product in respect to the right-handed rule

A.3   Unit vector cross product $\vec{v} \times \vec{B}$

The simplified geomagnetic model, $|\vec{v} \times \vec{B}|$, is treated as a unit cross product in the spherical coordinate system; the $|\vec{v}|$ vector is representing the shower direction (by its azimuth and zenith angles), and the $|\vec{B}|$ vector the Earth's magnetic field (by its azimuth and zenith angles) at the LOPES experiment location in Karlsruhe.

$$\vec{v} = \begin{pmatrix} v_x \\ v_y \\ v_z \end{pmatrix} = \begin{pmatrix} |v| \cdot sin(\theta) \cdot cos(\phi) \\ |v| \cdot sin(\theta) \cdot sin(\phi) \\ |v| \cdot cos(\theta) \end{pmatrix}$$

$$\vec{B} = \begin{pmatrix} B_x \\ B_y \\ B_z \end{pmatrix} = \begin{pmatrix} |B| \cdot sin(\theta) \cdot cos(\phi) \\ |B| \cdot sin(\theta) \cdot sin(\phi) \\ |B| \cdot cos(\theta) \end{pmatrix}$$

$$\vec{v} \times \vec{B} = \begin{pmatrix} v_y \cdot B_z - v_z \cdot B_y \\ v_z \cdot B_x - v_x \cdot B_z \\ v_x \cdot B_y - v_y \cdot B_x \end{pmatrix} = \begin{pmatrix} P_x \\ P_y \\ P_z \end{pmatrix} = \begin{pmatrix} North - South \\ East - West \\ Vertical \end{pmatrix}$$

In mathematics, the cross product is a binary operation of two vectors in a three-dimensional Euclidean-space that results in another vector which is perpendicular to the plane containing the two input vectors A.1(a). The vector direction is given by the right-hand rule and its magnitude equal to the area of the parallelogram that the vectors span A.1(b).

The cross product has the following properties:

$$a(b \times c) = (ab) \times c = b \times (ac);$$

$$a \times (b + c) = a \times b + a \times c;$$

$$(a + b) \times c = a \times c + b \times c$$

$$a \times b = -b \times a$$

Order is important in the cross product. If the order of operations changes in a cross product the direction of the resulting vector is reversed.

Recently, there have been suggestions, see [58], [48], that in addition to the polarization characteristics, also the absolute amplitude of the electric field in a first approximation can be considered to be proportional to this Lorentz force. Thus the vector magnitude and its directivity can be calculated as follows:

$$Magnitude = \sqrt{P_x^2 + P_y^2};$$

$$Directivity = tan(\theta) = \tan^{-1}(P_y/P_x);$$

hence,

$$P_x = P \times cos(\theta), \ P_y = P \times sin(\theta)$$

B. Lateral profiles
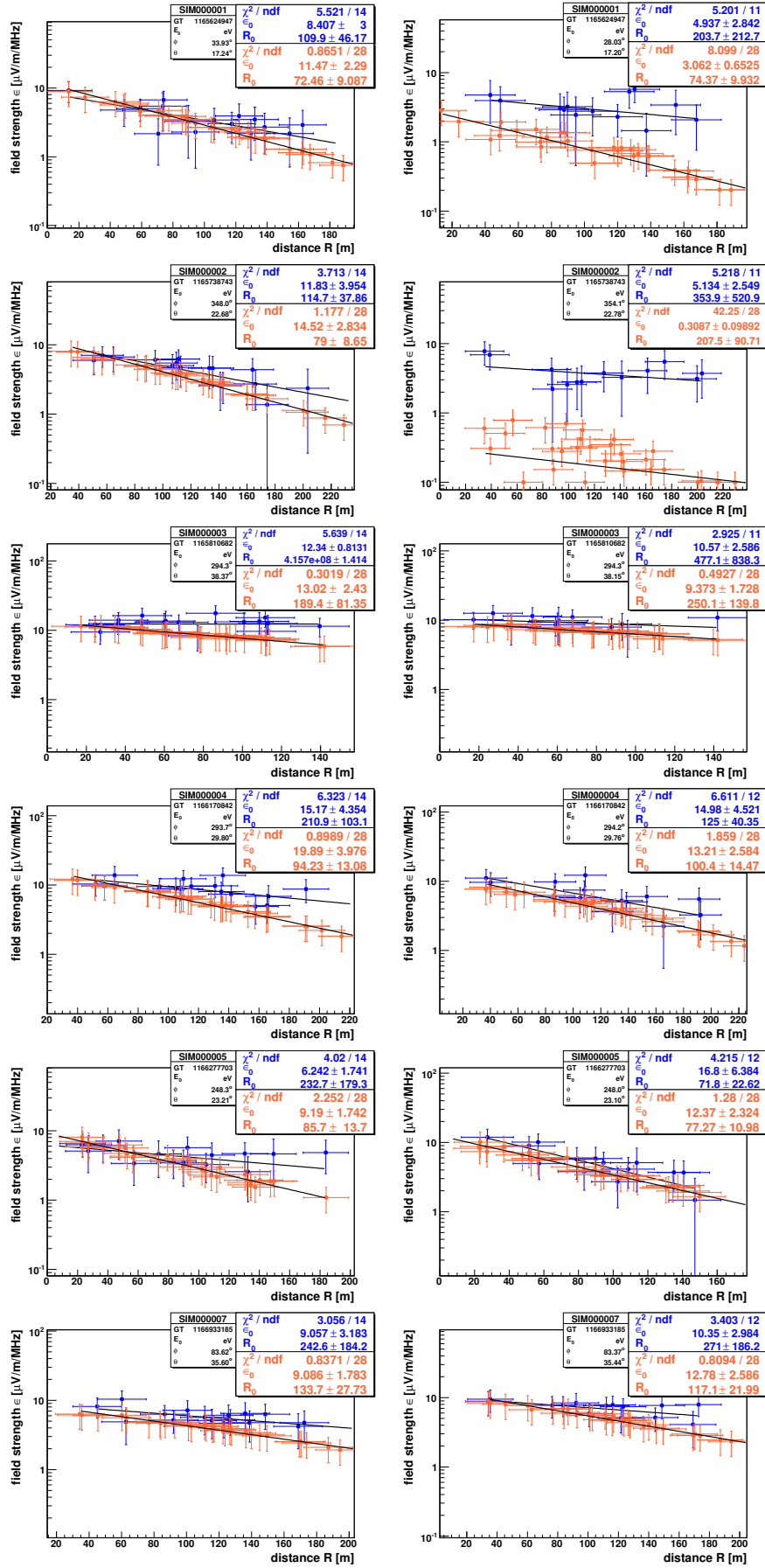
Figure B.1: Lateral distribution of single events of $E_p > 10^{17}$ eV. Left side: EW polarization. Right side: NS polarization. Blue: measurement. Red: Simulation.
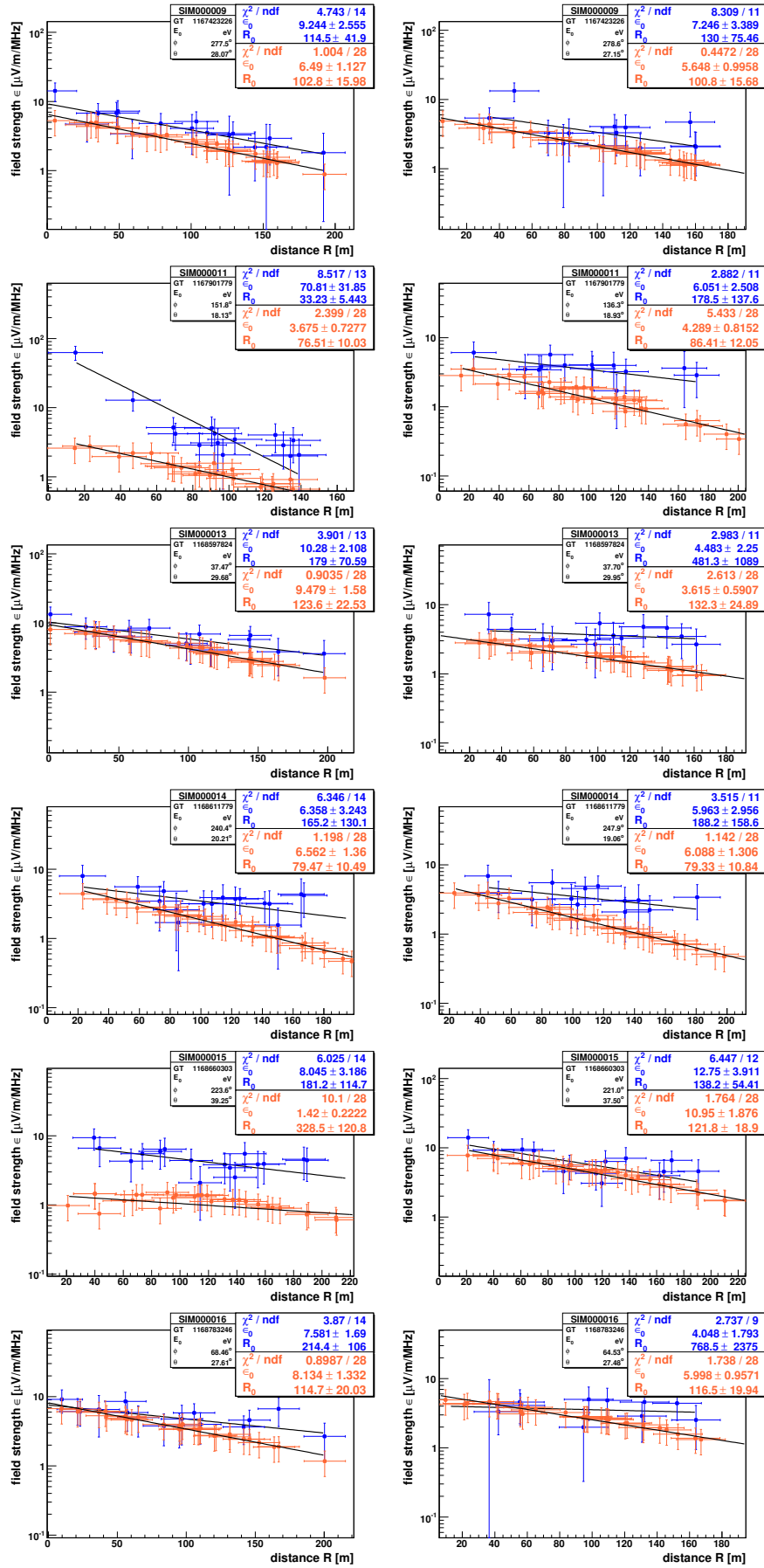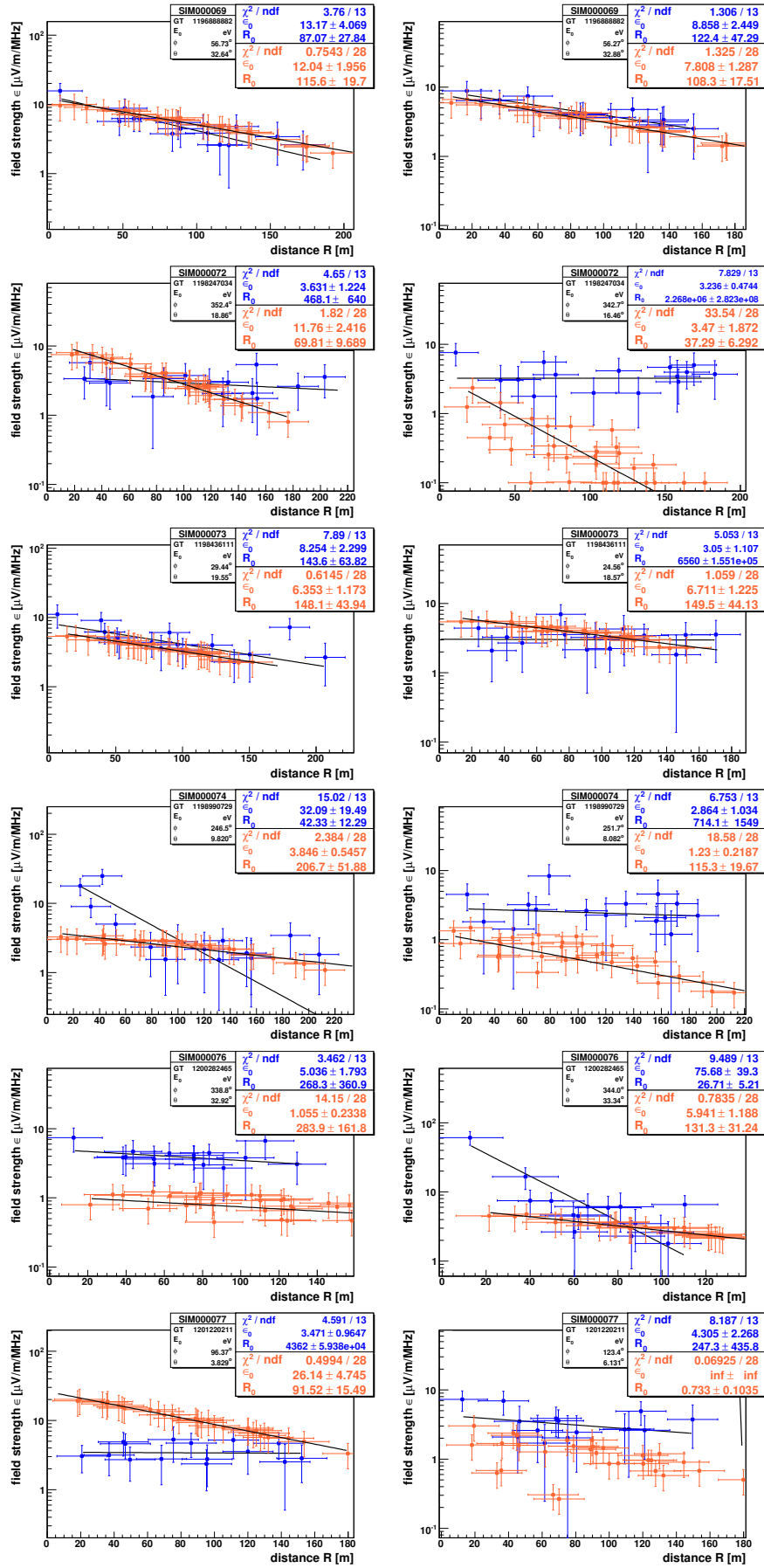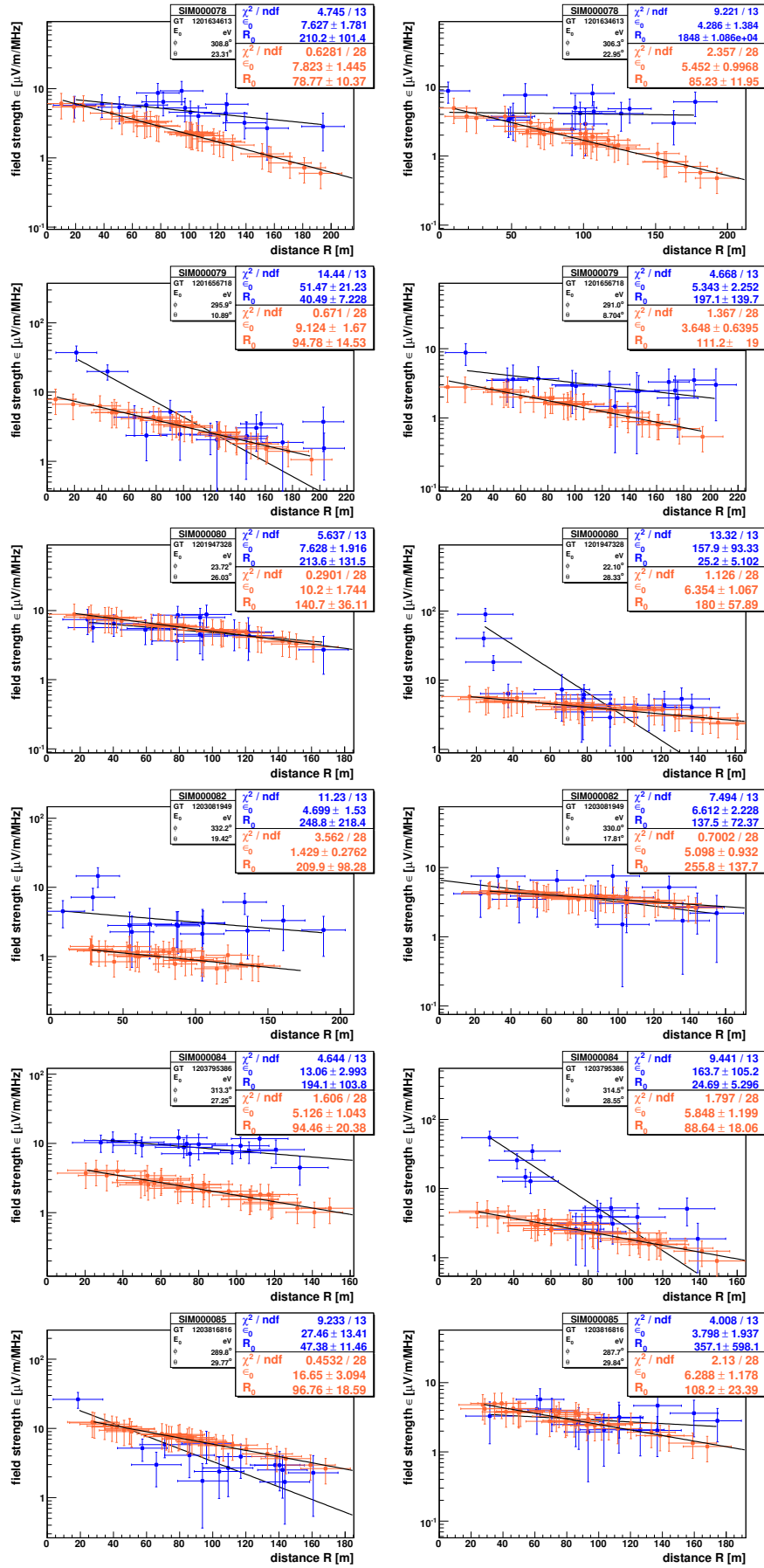
Figure B.2: Lateral distribution of single events of $E_p > 10^{17}$ eV. Left side: EW polarization. Right side: NS polarization. Blue: measurement. Red: Simulation.
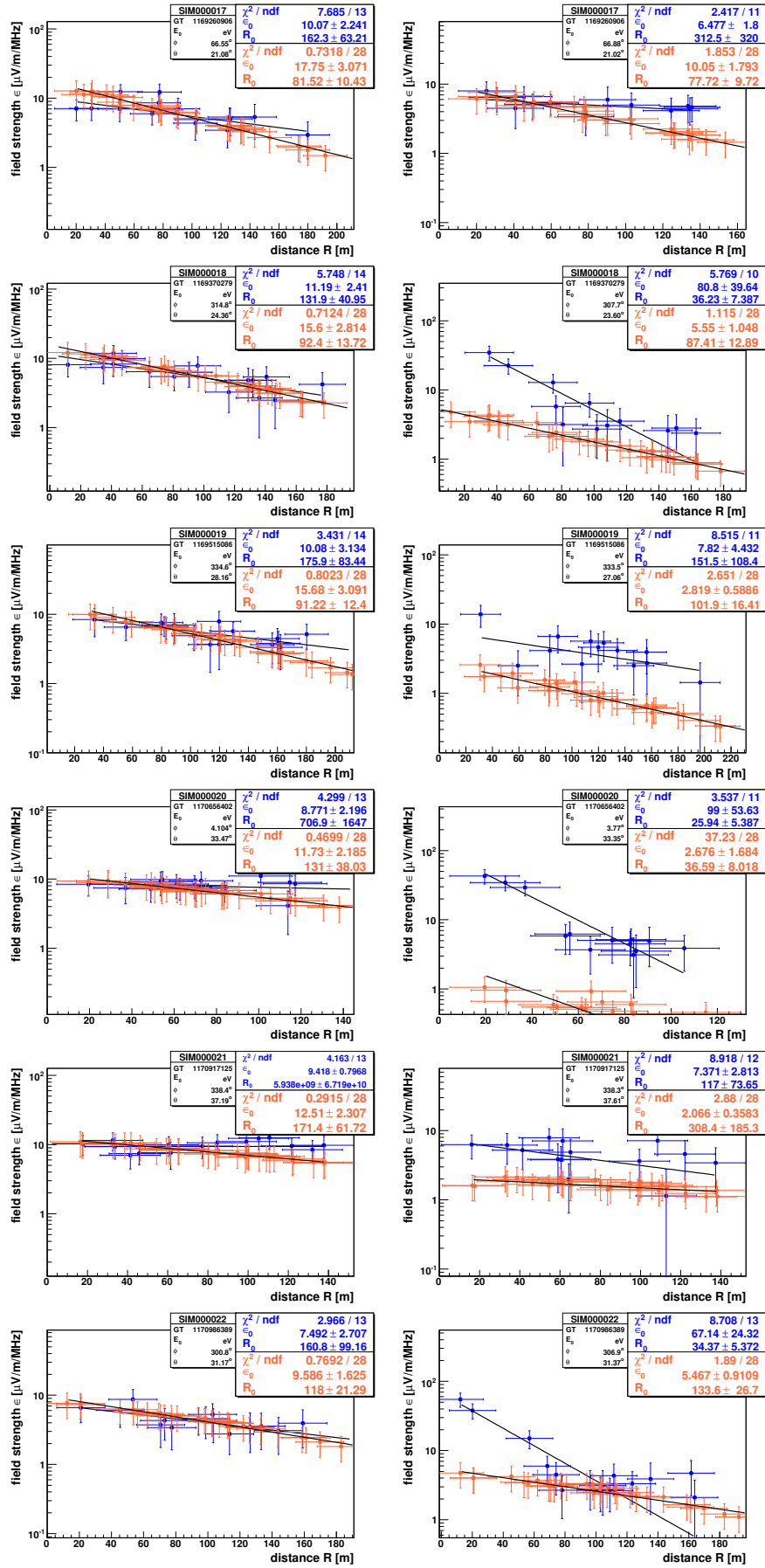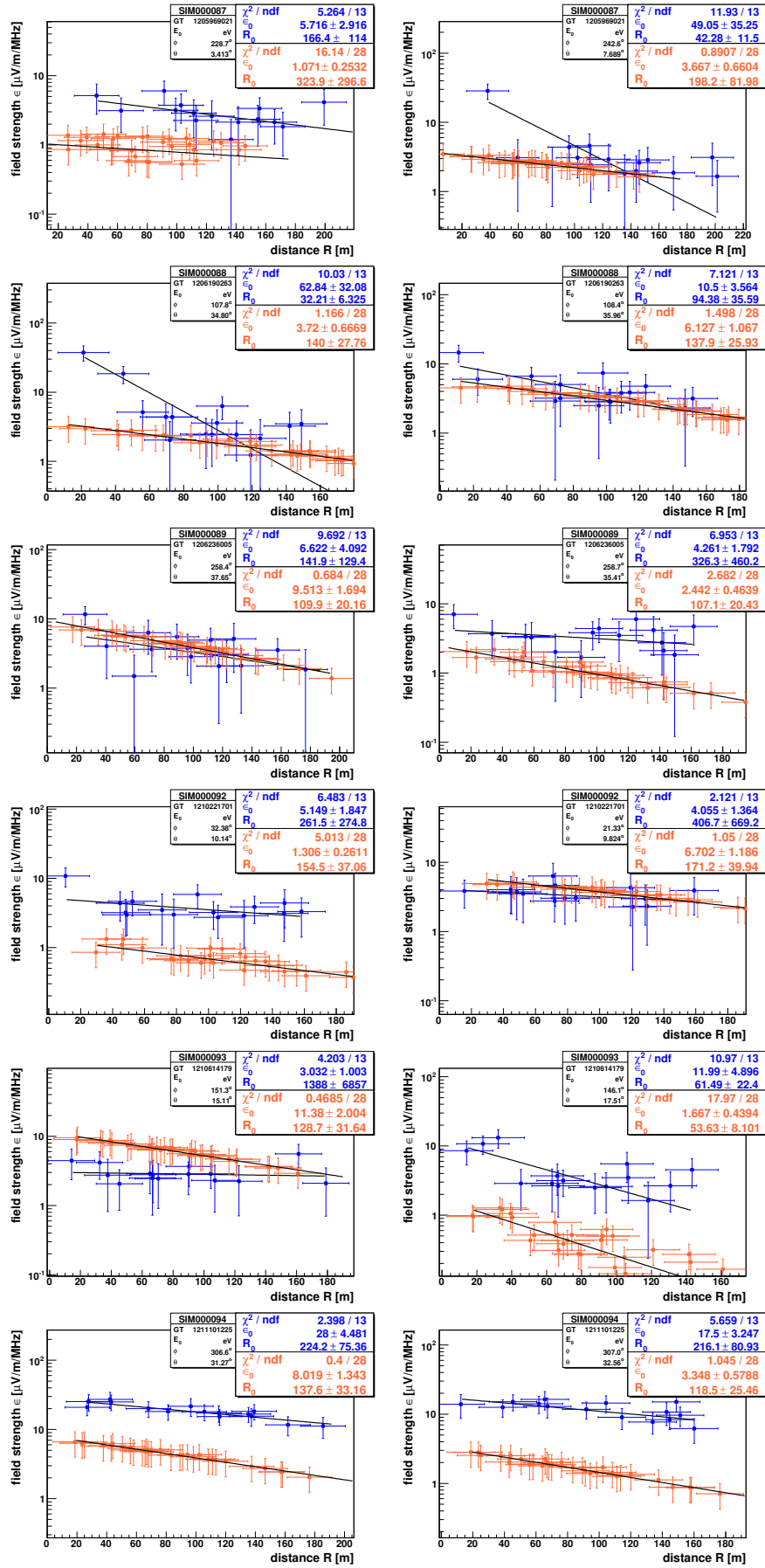
Figure B.3: Lateral distribution of single events of $E_p > 10^{17}$ eV. Left side: EW polarization. Right side: NS polarization. Blue: measurement. Red: Simulation.
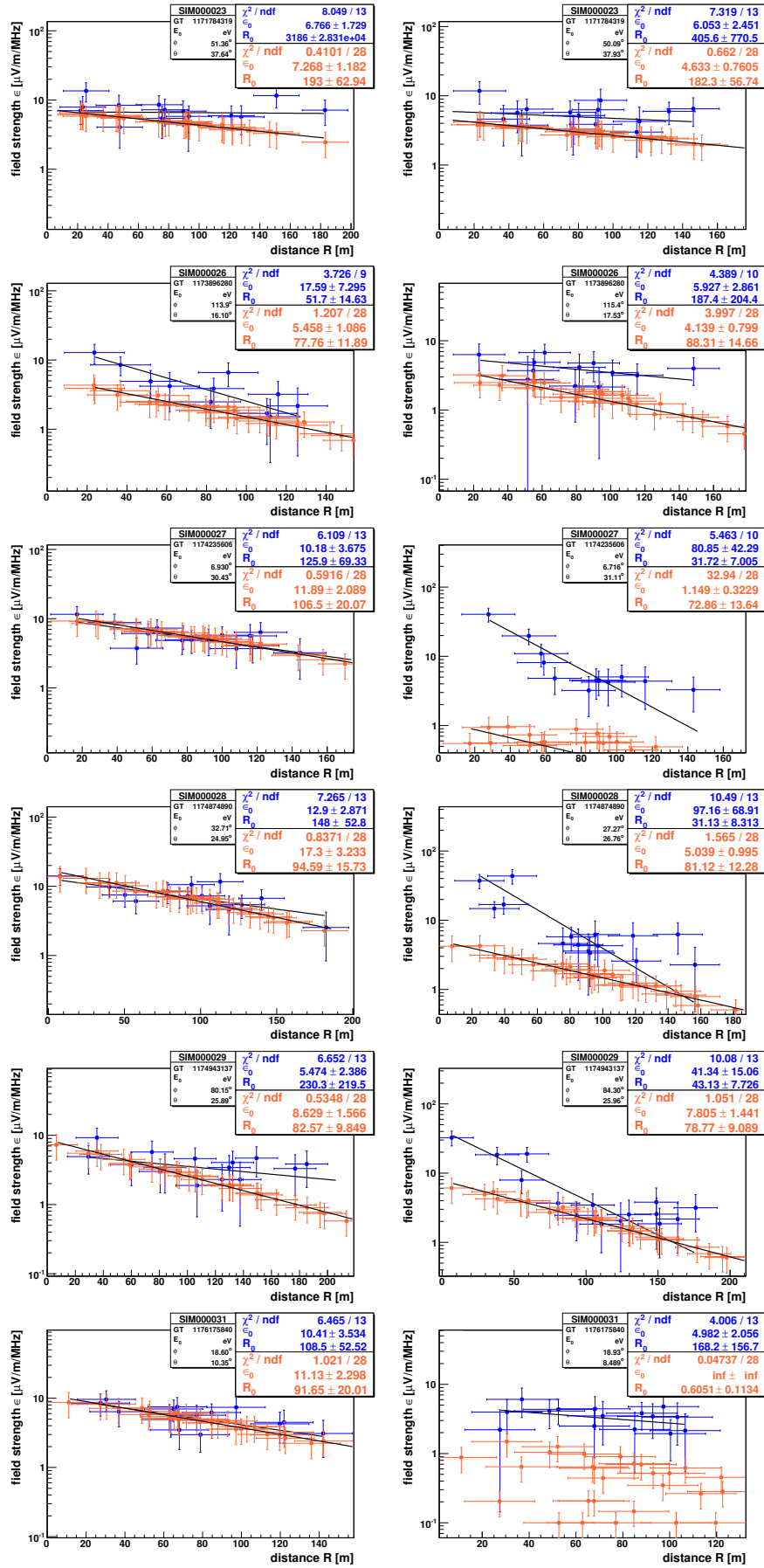
Figure B.4: Lateral distribution of single events of $E_p > 10^{17}$ eV. Left side: EW polarization. Right side: NS polarization. Blue: measurement. Red: Simulation.
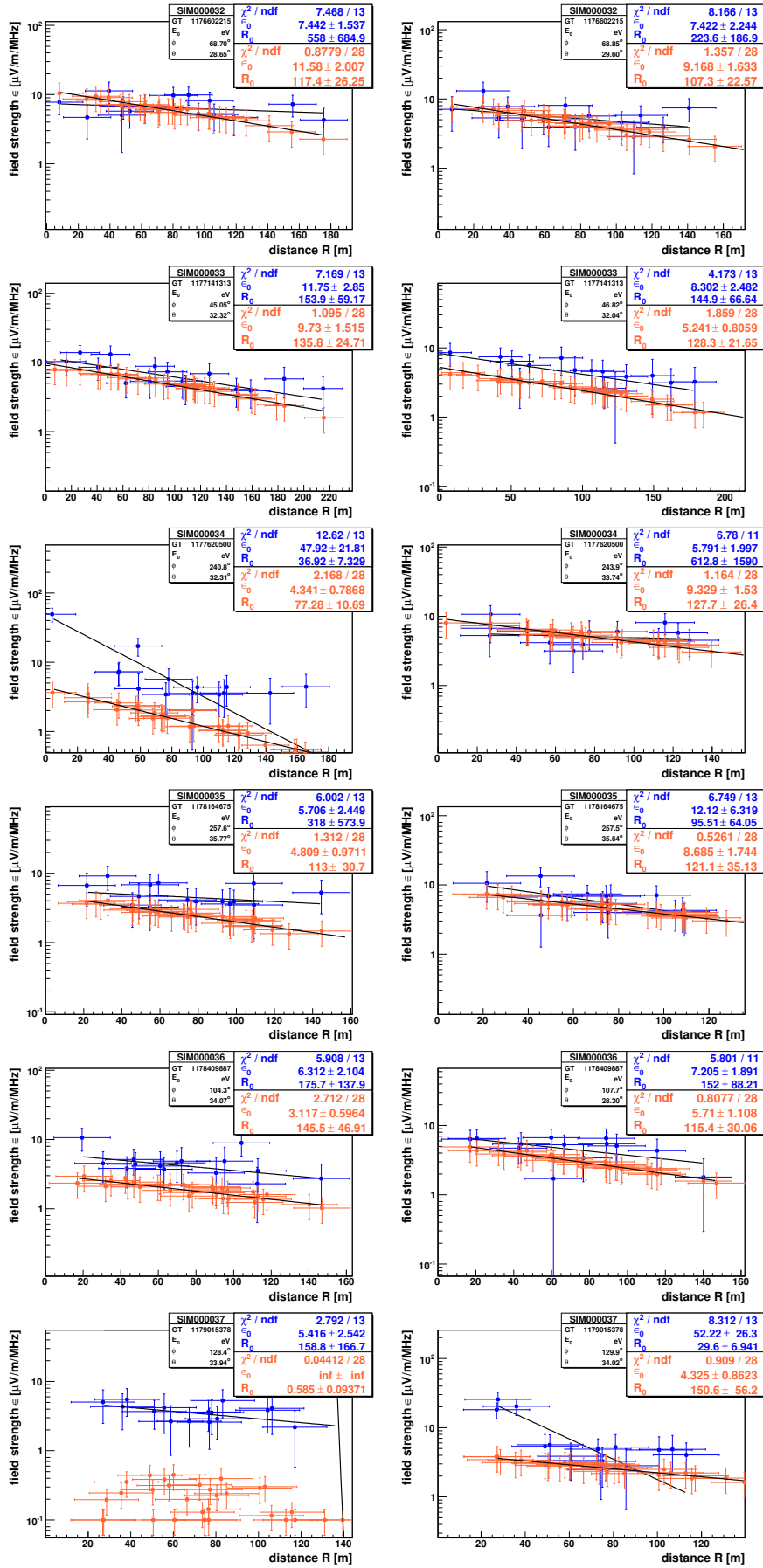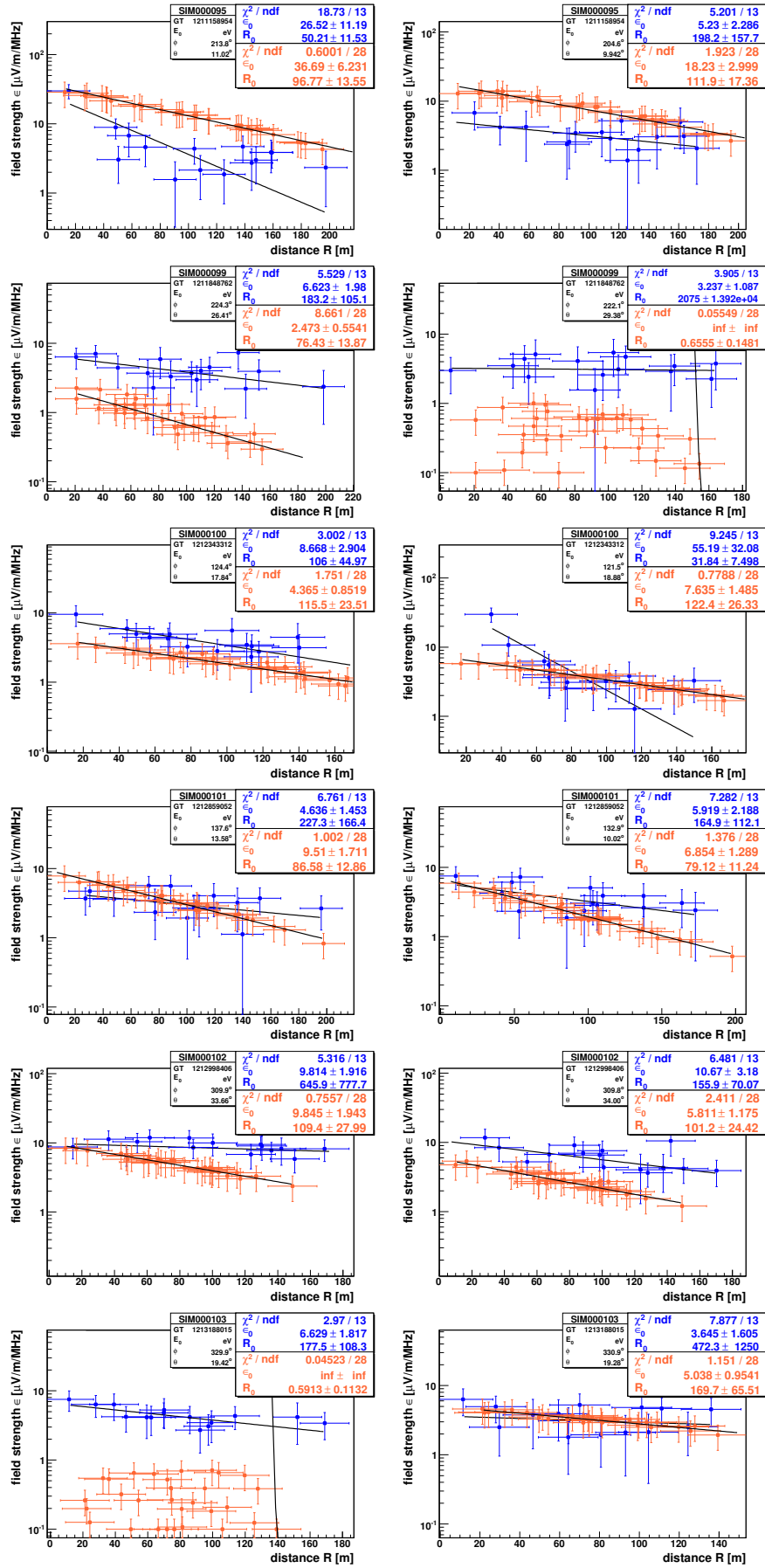
Figure B.5: Lateral distribution of single events of $E_p > 10^{17}$ eV. Left side: EW polarization. Right side: NS polarization. Blue: measurement. Red: Simulation.
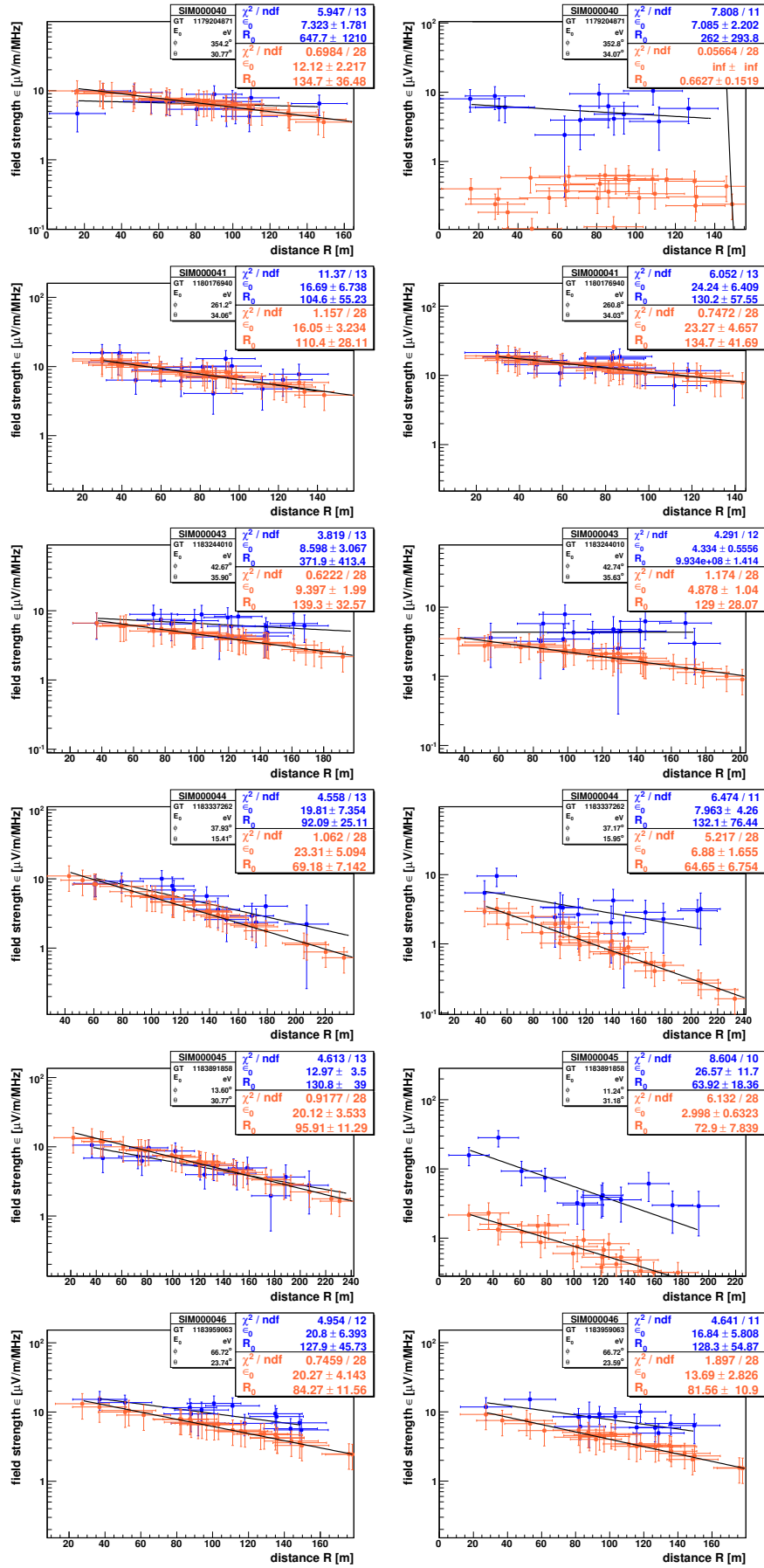
Figure B.6: Lateral distribution of single events of $E_p > 10^{17}$ eV. Left side: EW polarization. Right side: NS polarization. Blue: measurement. Red: Simulation.
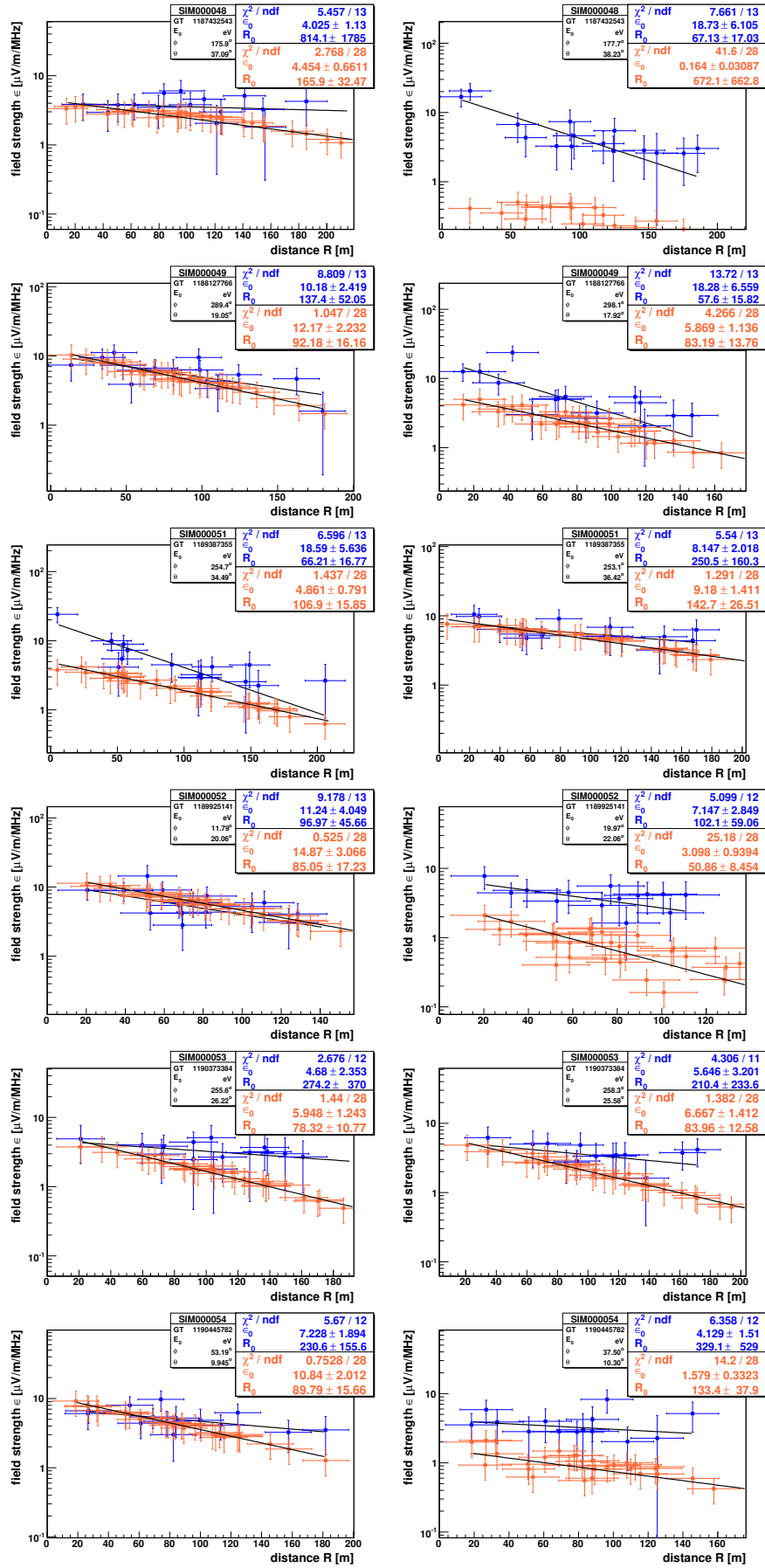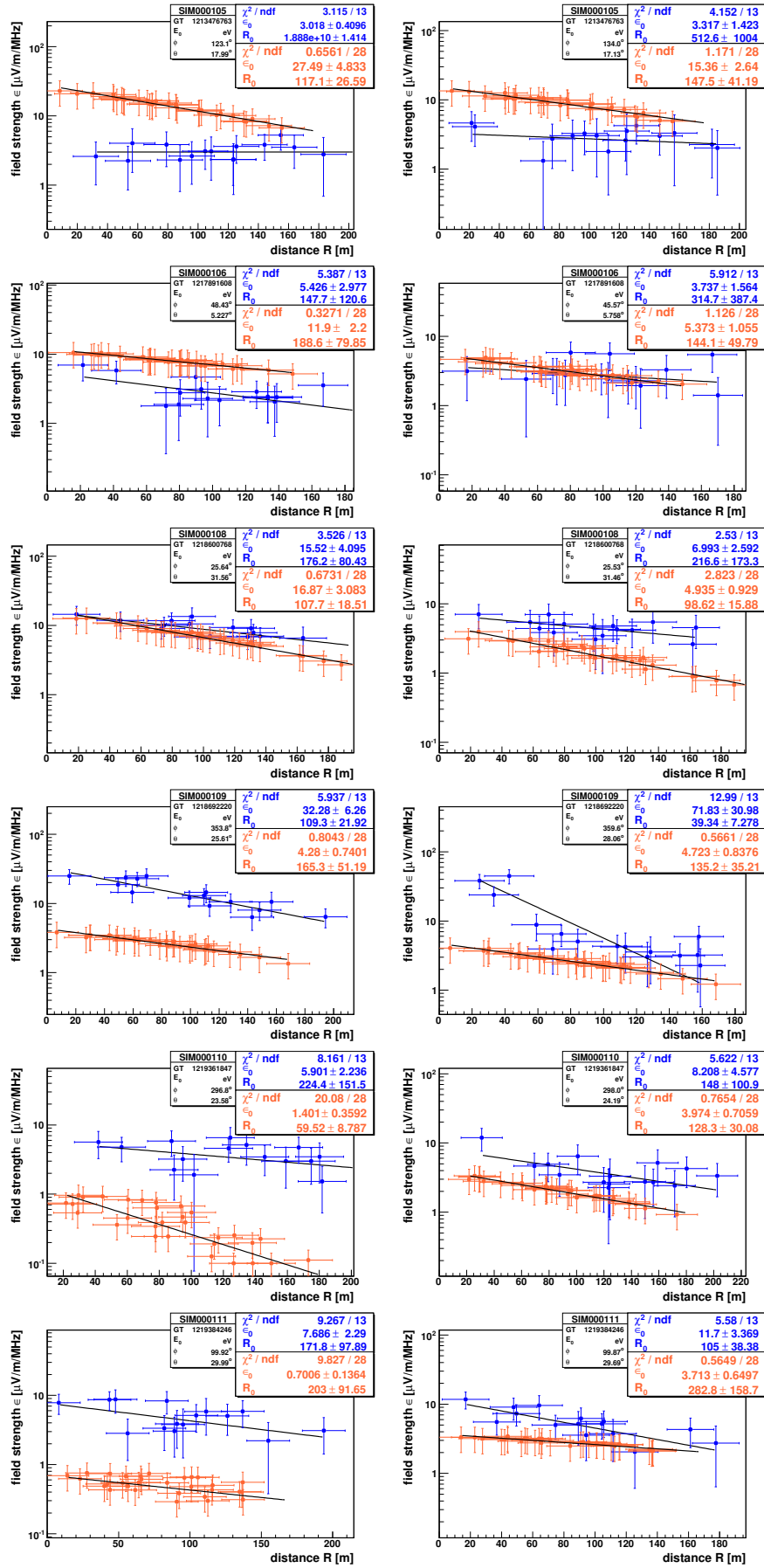
Figure B.7: Lateral distribution of single events of $E_p > 10^{17}$ eV. Left side: EW polarization. Right side: NS polarization. Blue: measurement. Red: Simulation.
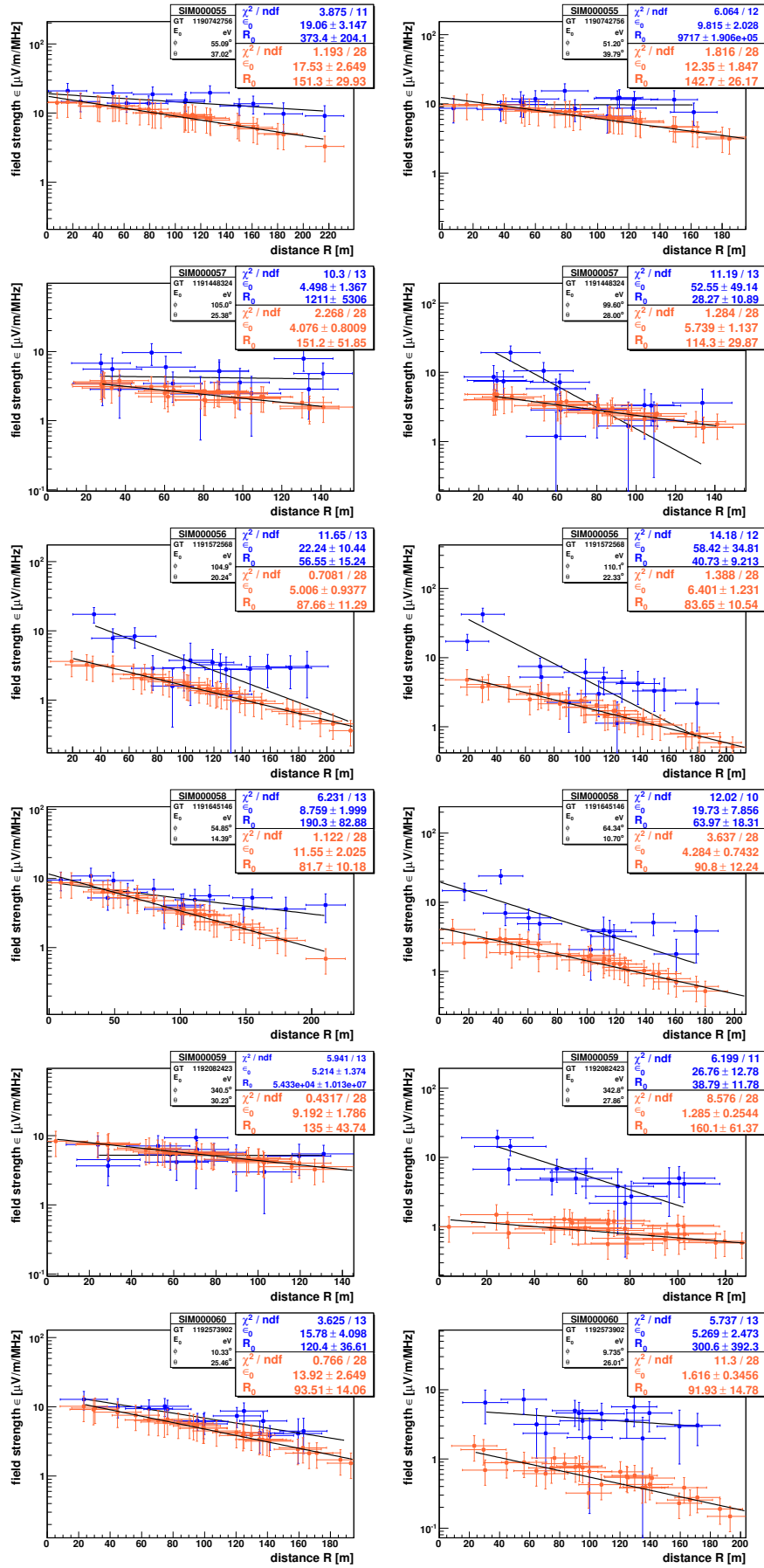
Figure B.8: Lateral distribution of single events of $E_p > 10^{17}$ eV. Left side: EW polarization. Right side: NS polarization. Blue: measurement. Red: Simulation.
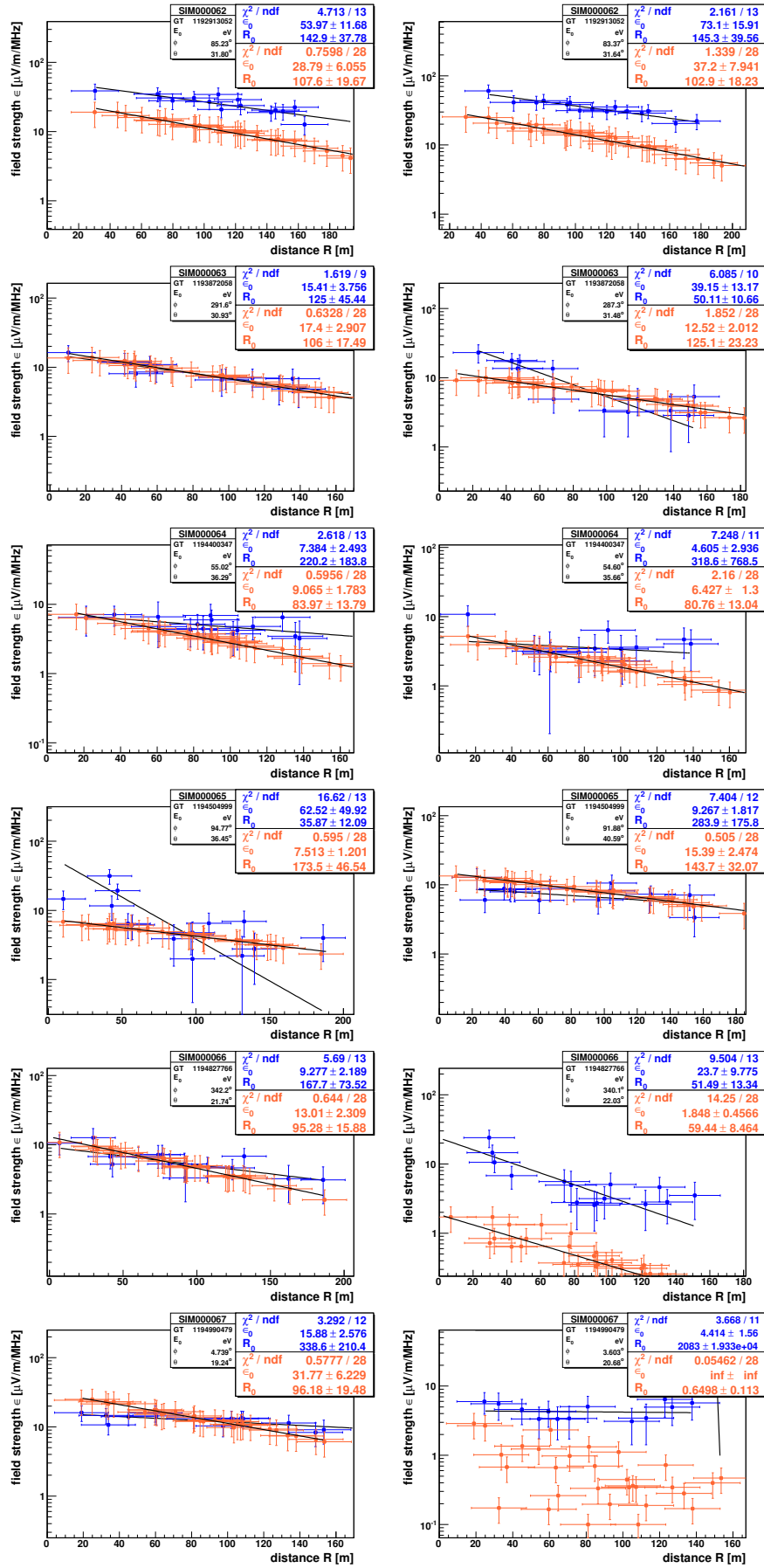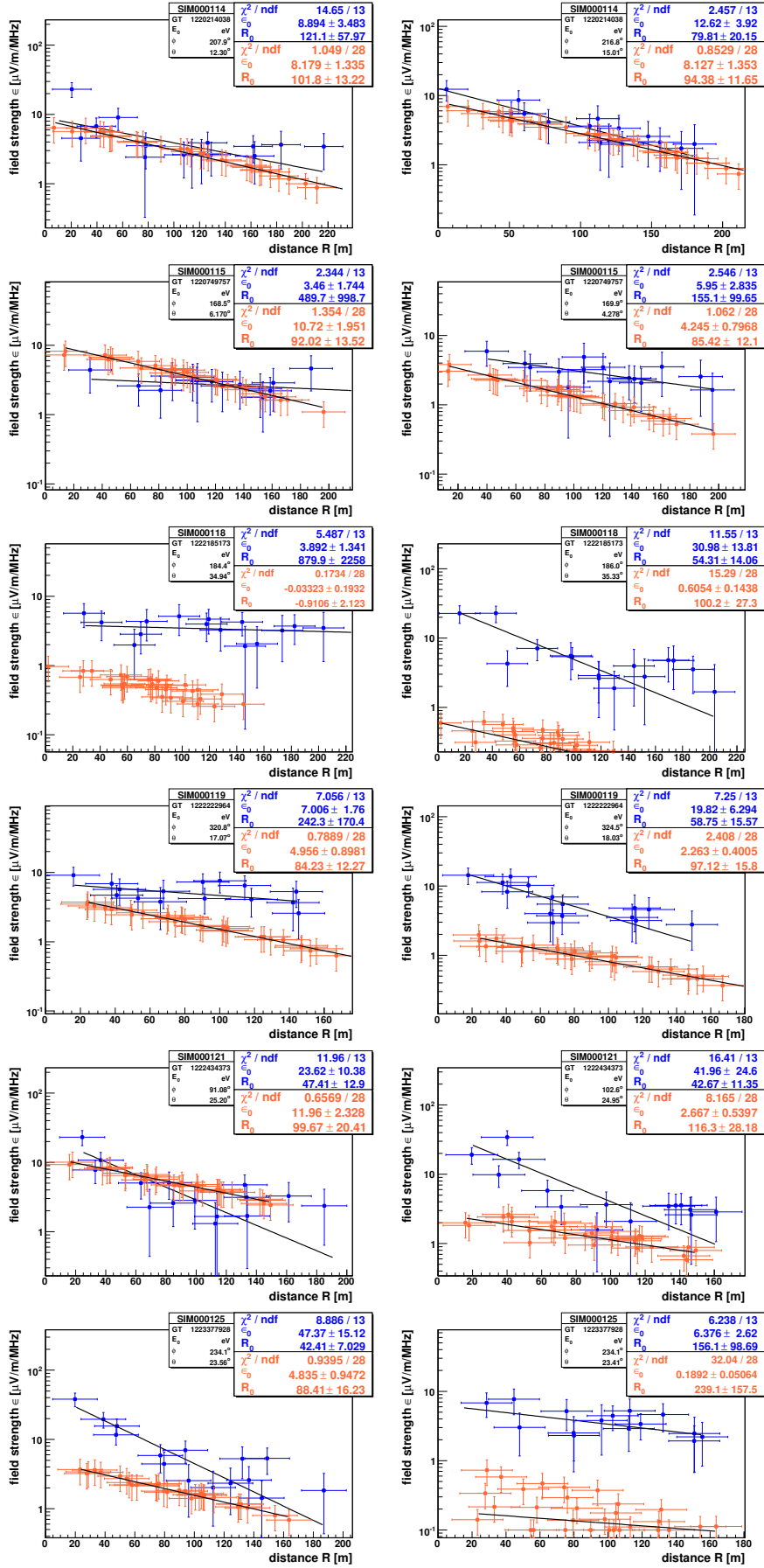
Figure B.9: Lateral distribution of single events of $E_p > 10^{17}$ eV. Left side: EW polarization. Right side: NS polarization. Blue: measurement. Red: Simulation.

Figure B.10: Lateral distribution of single events of $E_p > 10^{17}$ eV. Left side: EW polarization. Right side: NS polarization. Blue: measurement. Red: Simulation.
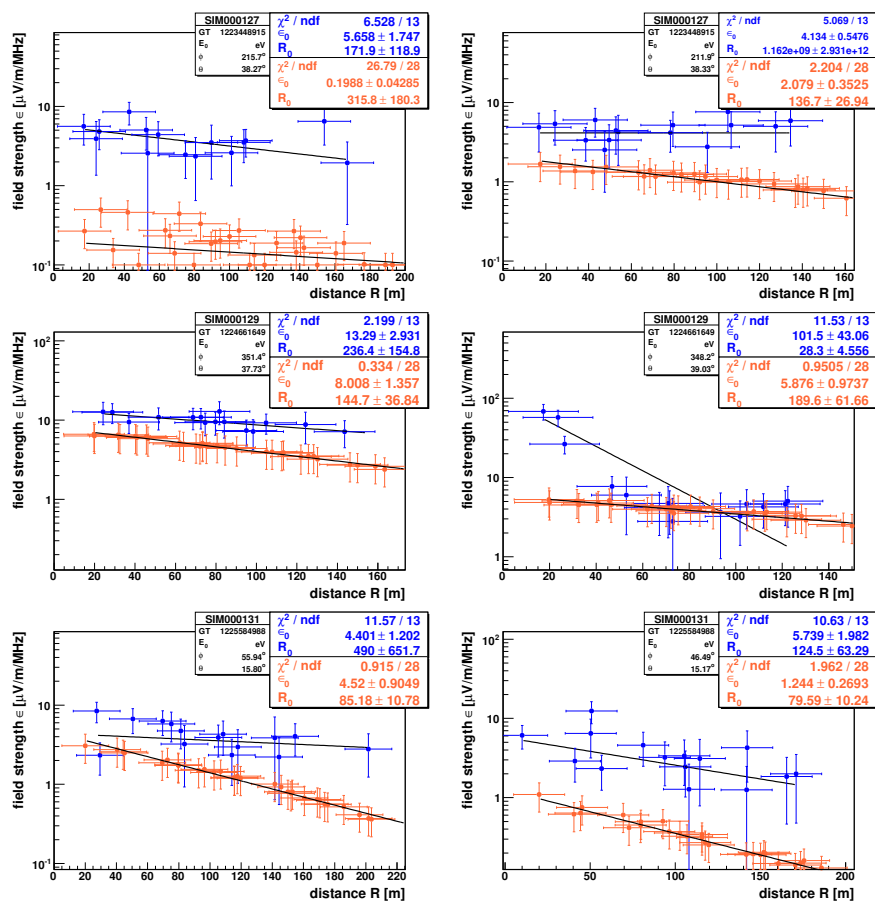
Figure B.11: Lateral distribution of single events of $E_p > 10^{17}$ eV. Left side: EW polarization. Right side: NS polarization. Blue: measurement. Red: Simulation.

Figure B.12: Lateral distribution of single events of $E_p > 10^{17}$ eV. Left side: EW polarization. Right side: NS polarization. Blue: measurement. Red: Simulation.

Figure B.13: Lateral distribution of single events of $E_p > 10^{17}$ eV. Left side: EW polarization. Right side: NS polarization. Blue: measurement. Red: Simulation.

Figure B.14: Lateral distribution of single events of $E_p > 10^{17}$ eV. Left side: EW polarization. Right side: NS polarization. Blue: measurement. Red: Simulation.

Figure B.15: Lateral distribution of single events of $E_p > 10^{17}$ eV. Left side: EW polarization. Right side: NS polarization. Blue: measurement. Red: Simulation.

Figure B.16: Lateral distribution of single events of $E_p > 10^{17}$ eV. Left side: EW polarization. Right side: NS polarization. Blue: measurement. Red: Simulation.

Bibliography

[1] V. Hess. Über die Absorption der γ-Strahlung in der Atmosphäre. *Physikal. Zeitschrift*, 12:998, 1911.

[2] V. Hess. Über Beobachtungen der durchdringenden Strahlung bei sieben Freiballonfahrten. *Physikal. Zeitschrift*, 13:1084, 1912.

[3] P. Evans, L. Bryant. LHC Machine. *JINST*, 3:S08001, 2008.

[4] J. Blümer, R. Engel, and Hörandel J. R. Cosmic Rays from the knee to the highest energies. *Progress in Part. and Nucl. Phys.*, 63:293, 2009.

[5] P. Auger, R. Maze, and Mayer T. G. Extensive cosmic showers in the particles. *Compt.Rend.Acad., Sci.*, 206:1721, 1938.

[6] W. Kohlhörster, I. Matthes, and E. Weber. Heavy electrons in cosmic ray showers originating in the atmosphere. *Compt.Rend.Acad., Sci.*, 26:1721, 1938.

[7] J. V. Jelley. Radio pulses from extensive air showers. *Nature*, 205:327, 1965.

[8] H. R. Allan. Radio emission from extensive air shower. *Prog. in Element. part. and Cos. Ray Phys.*, 10:171, 1971.

[9] B. McBreen et al. Correlation between optical and radio emission from extensive air showers at large zenith angles. *Phys.Lett.*, 23:677, 1966.

[10] G. A. Askaryan. Excess Negative Charge of an Electron-Photon Shower And Its Coherent Radio Emission. *Soviet Phys. JETP*, 14:441, 1962.

[11] F. D. Kahn and I. Lerche. Radiation from Cosmic Ray Air Showers. *Proc. Roy. Soc.*, A189:206, 1966.

[12] H. Falcke and P. Gorham. Detecting radio emission from cosmic ray air showers and neutrinos with a digital radio telescope. *Astropart. Phys.*, 19:477, 2003.

[13] H. Falcke et al. LOPES Coll. Detection and imaging of atmospheric radio flashes from cosmic ray air showers. *Nature*, 435:313, 2005.

[14] A. Haungs et al. KASCADE-Grande Coll. The KASCADE-Grande experiment. Prepared for 28th International Cosmic Ray Conferences (ICRC 2003), Tsukuba, Japan, 31 Jul - 7 Aug 2003.

[15] T. Huege and H. Falcke. Radio emission from cosmic ray air showers: Simulation results and parametrization. *Astropart. Phys.*, 24:116, 2005.

[16] A. Haungs, H. Rebel, and M. Roth. Energy spectrum and mass-composition of high-energy cosmic rays. *Rep. Prog. Phys.*, 6:1145, 2003.

[17] G. Navarra et al. KASCADE-Grande Coll. KASCADE-Grande: A large acceptance, high-resolution cosmic-ray detector up to $10^{18}eV. Nucl.Instrum.Meth., A518 : 207, 2004.$

[18] W. D. Apel et al. KASCADE-Grande Coll. The KASCADE-Grande experiment. *NIMA*, in press, 2010.

[19] W. D. Apel et al. KASCADE-Grande Coll. Time structure of the EAS electron and muon components measured by the KASCADE-Grande experiment. *Astropart. Phys.*, 29:317, 2008.

[20] R. M. Baltrusaitis et al. The Utah Fly's Eye detector. *NIMA*, 240:410, 1985.

[21] F. Nerling, J. Blümer, R. Engel, and M. Risse. Description of Cherenkov light production in high-energy air showers. *Astropart. Phys.*, 24:421, 2006.

[22] J. A. Abraham et al. Pierre Auger Coll. The Fluorescence Detector of the Pierre Auger Observatory. *NIMA*, 24:421, 2006.

[23] J. A. Abraham et al. Pierre Auger Coll. Properties and performance of the prototype instrument for the Pierre Auger Observatory. *NIMA*, 523:50, 2004.

[24] B. Keilhauer, J. Blümer, R. Engel, and H. O. Klages. Impact of varying atmospheric profiles on extensive air shower observation: Fluorescence light emission and energy reconstruction. *Astropart. Phys.*, 25:259, 2006.

[25] F. Schröder et al. New method for the time calibration of an interferometric antenna array. *NIMA*, in press, 2010.

[26] T. Huege and H. Falcke. Radio Emission from Cosmic Ray Air Showers: Coherent Geosynchrotron Radiation. *Astron. Astrophys.*, 412:19, 2003.

[27] W. D. Apel et al. KASCADE-Grande Coll. The KASCADE-Grande experiment. *NIMA*, in press, 2010.

[28] A. Haungs et al. KASCADE-Grande Coll. Cosmic rays in the PeV range: Results from KASCADE. Prepared for International Workshop on Frontier Science: Physics and Astrophysics in Space, Frascati and Rome, Italy, 14-19 Jun 2004.

[29] A. Badea et al. KASCADE-Grande and the LOPES Coll. The KASCADE-Grande experiment and the LOPES project. *Nucl. Phys. Proc. Suppl.*, 136:384, 2004.

[30] T. Asch et al. LOPES Coll. Trigger Strategy for Radio Detection in Atmospheric Air Showers with LOPES(STAR). *Proceedings of the 30th International Cosmic Ray Conference, Mexico City, Mexico*, 5:1081, 2008.

[31] A. Haungs et al. LOPES Coll. Radio emission in atmospheric air showers: Results of LOPES-10. *Journal of Phys.: Conf. Series, Proc. of ARENA, University of Northumbria, UK*, 81:012005, 2007.

[32] W. D. Apel et al. LOPES Coll. Progress in air shower radio measurements: Detection of distant events. *Astropart. Phys.*, 26:332, 2006.

[33] P. G. Isar et al. LOPES Coll. Radio emission in atmospheric air showers: First measurements with LOPES-30. *J. Phys. Conf. Ser.*, 81:012006, 2007.

[34] P. G. Isar et al. LOPES Coll. Radio emission in atmospheric air showers measured by LOPES-30. *AIP Conf. Proc.*, 972:470, 2008.

[35] P. G. Isar et al. LOPES Coll. Radio emission of energetic cosmic ray air showers: Polarization measurements with LOPES. *Nucl. Instrum. Meth.*, A604:81, 2009.

[36] S. Nehls et al. Amplitude calibration of a digital radio antenna array for measuring cosmic ray air showers. *Nucl. Instrum. Meth.*, A589:350, 2008.

[37] A. Saftoiu et al. LOPES Coll. Analysis of inclined showers measured with LOPES. *Nucl. Instrum. Meth.*, A604:9, 2009.

[38] A. Horneffer et al. LOPES Coll. The LOPES System for the Detection of Radio Pulses from Air Showers. *Astronomy and Astrophysics*, to be published, 2010.

[39] A. Horneffer et al. LOPES Coll. Primary Particle Energy Calibration of the EAS Radio Pulse Height. *Proceedings of the 30th International Cosmic Ray Conference, Mexico City, Mexico*, 4:83, 2008.

[40] W. D. Apel et al. LOPES Coll. Lateral Distribution of the Radio Signal in Extensive Air Showers Measured with LOPES. *Astropart. Phys.*, 32.

[41] A. Saftoiu et al. LOPES Coll. Update on radio detection of inclined air showers with LOPES-10. *Proc. of the 30th Cosmic Ray Conference.*, 4:231, 2007.

[42] S. Buitink et al. LOPES Coll. Amplified radio emission from cosmic ray air showers in thunderstorms. *Astron. Astrophys.*, 467:385, 2007.

[43] M. Ender et al. LOPES Coll. Radio emission of extensive air showers during thunderstorms. *Proceedings of the 31th International Cosmic Ray Conference, Mexico City, Mexico*, 2009.

[44] A. Nigl et al. LOPES Coll. Direction identification in radio images of cosmic-ray air showers detected with LOPES and KASCADE. *Astronomy and Astrophysics*, in press, 2008.

[45] A. Haungs et al. LOPES Coll. Recent results of the LOPES experiment. *Nucl. Phys. B (Proc.Suppl.)*, 196:297, 2009.

[46] C. Riviere et al. CODALEMA Coll. Radio emission of extensive air shower at CODALEMA: Polarization of the radio emission among the v x B vector. *Proceedings of the 31th International Cosmic Ray Conference, Mexico City, Mexico*, 2009.

[47] D. Ardouin et al. CODALEMA Coll. Radioelectric field features of extensive air-showers observed with codalema. *Astropart. Phys.*, 26:341, 2006.

[48] D. Ardouin et al. CODALEMA Coll. Geomagnetic origin of the radio emission from cosmic ray induced air showers observed by CODALEMA. *Astropart. Phys.*, 31:192, 2009.

[49] D. A. Suprun, P. W. Gorham, and J. L. Rosner. Synchrotron radiation at radio frequencies from cosmic ray air showers. *Astropart. Phys.*, 20:157, 2003.

[50] D. Heck, J. Knapp, J. G. Capdevielle, G. Schatz, and T. Thouw. CORSIKA: A Monte Carlo Code to Simulate Extensive Air Showers. *Forschungszentrum Karlsruhe Report - FZKA*, 6019, 1998.

[51] T. Huege, R. Ulrich, and R. Engel. Monte Carlo simulations of geosynchrotron radio emission from CORSIKA-simulated air showers. *Astropart. Phys.*, 27:392, 2007.

[52] P. G. Isar et al. LOPES Coll. Polarization studies of the EAS radio emission with the LOPES experiment. *Proceedings of the 31th International Cosmic Ray Conference, Lodz, Poland. In press.*

[53] T. Huege, R. Ulrich, and R. Engel. Energy and composition sensitivity of geosynchrotron radio emission from cosmic ray air showers. *Astropart. Phys.*, 30:96, 2008.

[54] M. Ludwig and T. Huege. Completion of the geosynchrotron model with variation of number of charges. *In progress.*

[55] A. Haungs et al. LOPES Coll. Air Shower Measurements with the LOPES Radio Antenna Array. *Nucl. Instrum. Meth. A*, 604:S1, 2009.

[56] A. M. van den Berg. Radio detection of cosmic rays at the southern auger observatory. *Proceedings of the 31st ICRC, Lodz, Poland*, 2009.

[57] J. Hörandel et al. LOFAR Coll. LOFAR - A new experiment to record radio emission from cosmic particles. *Nuclear Physics B (Proc. Suppl.)*, 196:289, 2009.

[58] T. Huege and H. Falcke. Monte Carlo simulations of radio emission from cosmic ray air showers. *Int. J. Mod. Phys.*, A21S1:60–64, 2006.

Acknowledgment